THE INFLUENCE OF COOLING CONFIGURATION AND TIP GEOMETRY ON
GAS TURBINE BLADE TIP LEAKAGE FLOW AND HEAT TRANSFER

A THESIS SUBMITTED TO
THE GRADUATE SCHOOL OF NATURAL AND APPLIED SCIENCES
OF
MIDDLE EAST TECHNICAL UNIVERSITY

BY

SERGEN SAKAOĞLU

IN PARTIAL FULFILLMENT OF THE REQUIREMENTS
FOR
THE DEGREE OF MASTER OF SCIENCE
IN
AEROSPACE ENGINEERING

SEPTEMBER 2019

Approval of the thesis:

THE INFLUENCE OF COOLING CONFIGURATION AND TIP GEOMETRY ON GAS TURBINE BLADE TIP LEAKAGE FLOW AND HEAT TRANSFER

submitted by **SERGEN SAKAOĞLU** in partial fulfillment of the requirements for the degree of **Master of Science in Aerospace Engineering Department, Middle East Technical University** by,

Prof. Dr. Halil Kalıpçılar
Dean, Graduate School of **Natural and Applied Sciences**   ⎯⎯⎯⎯⎯⎯

Prof. Dr. İsmail Hakkı Tuncer
Head of Department, **Aerospace Engineering**   ⎯⎯⎯⎯⎯⎯

Assist. Prof. Dr. Harika Senem Kahveci
Supervisor, **Aerospace Engineering, METU**   ⎯⎯⎯⎯⎯⎯

Examining Committee Members:

Prof. Dr. Oğuz Uzol
Aerospace Engineering, METU   ⎯⎯⎯⎯⎯⎯

Assist. Prof. Dr. Harika Senem Kahveci
Aerospace Engineering, METU   ⎯⎯⎯⎯⎯⎯

Assoc. Prof. Dr. Sinan Eyi
Aerospace Engineering, METU   ⎯⎯⎯⎯⎯⎯

Prof. Dr. Mehmet Haluk Aksel
Mechanical Engineering, METU   ⎯⎯⎯⎯⎯⎯

Assist. Prof. Dr. Sıtkı Uslu
Mechanical Engineering, TOBB ETU   ⎯⎯⎯⎯⎯⎯

Date: 11.09.2019

I hereby declare that all information in this document has been obtained and presented in accordance with academic rules and ethical conduct. I also declare that, as required by these rules and conduct, I have fully cited and referenced all material and results that are not original to this work.

Name, Surname: Sergen Sakaoğlu

Signature   :

ABSTRACT

THE INFLUENCE OF COOLING CONFIGURATION AND TIP GEOMETRY ON GAS TURBINE BLADE TIP LEAKAGE FLOW AND HEAT TRANSFER

Sakaoğlu, Sergen

M.S., Department of Aerospace Engineering

Supervisor: Assist. Prof. Dr. Harika Senem Kahveci

September 2019, 100 pages

In gas turbine engines, an increase in the thermal efficiency and power output can be ensured by increasing the turbine inlet temperature. This causes the high-pressure turbine (HPT) blades to be exposed to extremely high temperatures that requires the introduction of cooling flow in order to keep the temperatures within the allowable material limits and to reduce the high thermal loads on the blade. However, cooling flow introduced around the blade tip region affects the blade tip leakage flow and blade tip heat transfer. This work explores the effects of various combinations of location, size, and number of cooling holes used for blade tip cooling and different tip types with varying geometry on pressure loss and thermal performance. These combinations are analyzed either in the stationary or the rotating domain using computational fluid dynamics (CFD). The first-stage high-pressure turbine blade profile of the well-known General Electric Energy Efficient Engine (GE-E3) is used in the research. Findings suggest that squealer tips are superior to flat tips in terms of both aero and thermal performances and they give the best cooling performance when a larger number of cooling holes is located closer to the blade pressure side.

For squealer tips, rotation and addition of cooling at the tip are observed to alter the tip gap flow. Heat transfer coefficient on the squealer blade tip is found to increase with the addition of cooling, while higher film-cooling effectiveness is obtained with increasing the rim height

ÖZ

SOĞUTMA KONFİGÜRASYONU VE KANAT UCU GEOMETRİSİNİN GAZ TÜRBİN KANAT UCU KAÇAK AKIŞI VE ISI TRANSFERİNE ETKİSİ

Sakaoğlu, Sergen

Yüksek Lisans, Havacılık ve Uzay Mühendisliği Bölümü

Tez Yöneticisi: Dr. Öğr. Üyesi Harika Senem Kahveci

Eylül 2019 , 100 sayfa

Gaz türbini motorlarında, termal verimin ve üretilen gücün artırılması, türbin giriş sıcaklığının artırılmasıyla sağlanabilir. Bu durum yüksek basınç türbin (YBT) kanatlarının aşırı yüksek sıcaklıklara maruz kalmasına sebep olduğu için, sıcaklıkların malzeme limitlerini aşmasını önlemek ve kanat üzerinde etkiyen yüksek termal yükleri azaltmak için soğutma havasının kullanılması gerekmektedir. Öte yandan, kanat ucu bölgesine verilen soğutma havası, kanat ucu kaçak akışını ve kanat ucu ısı transferini etkilemektedir. Bu çalışma, kanat ucu soğutması için kullanılan soğutma deliklerinin yeri, büyüklüğü ve sayısının çeşitli kombinasyonlarının, ve geometrisi değiştirilen farklı kanat ucu türlerinin, basınç kaybı ve termal performans üzerindeki etkilerini araştırmaktadır. Bu kombinasyonlar, sabit veya döndürülen hesaplama alanlarında hesaplamalı akışkanlar dinamiği (HAD) kullanılarak incelenmiştir. Araştırmada bilinen General Electric Energy Efficient Engine (GE-E3)'nin ilk kademe yüksek basınç türbin kanat profili kullanılmıştır. Sonuçlar, kavite türü kanat uçlarının hem aerodinamik hem de termal performans açıdan düz kanat uçlarına göre daha üstün olduğunu ve bu kanat türünün en iyi soğutma performansını daha fazla soğutma deliği kanat

basınç kenarına daha yakın yerleştirildiğinde verdiğini göstermektedir. Kavite türü kanat uçları için, rotasyon ve kanat ucuna soğutmanın eklenmesinin kanat ucundaki akışı değiştirdiği gözlemlenmiştir. Kavite türü kanat ucundaki ısı transferi kat sayısının soğutuldukça arttığı ve kanat ucu rim yüksekliği artırıldıkça daha yüksek film soğutma verimi elde edildiği bulunmuştur.

Anahtar Kelimeler: Türbin Kanadı, Kanat Ucu Kaçak Akış, Soğutma Konfigürasyonu, Isı Transferi, Kanat Ucu Geometrisi, Hesaplamalı Akışkanlar Dinamiği

To my family for their belief in me.

ACKNOWLEDGMENTS

TABLE OF CONTENTS

LIST OF TABLES

TABLES

LIST OF FIGURES

FIGURES

xvii

xviii

LIST OF ABBREVIATIONS

A   Area [m^2]

BSL   Baseline

C   Chord [mm]

C_x Axial chord [mm]

CFD   Computational fluid dynamics

d   Diameter [mm]

d Squealer depth [mm]

e   Relative error between meshes

EXP   Experimental

F   Blending function

GCI   Grid Convergence Index

h Wall heat transfer coefficient [$W/m^2.K$]

$\overline{h}$ Averaged wall heat transfer coefficient [$W/m^2.K$]

h   Blade span [mm]

H   Enthalpy [J]

HPT   High pressure turbine

k   Turbulent kinetic energy [m^2/s^2]

k_f Thermal conductivity of air [$W/m.K$]

LE   Leading edge

$\dot{m}$ Mass flow rate [kg/m^3]

M   Mach Number

Nu   Nusselt number

N   Number of nodes

NHFR	Net heat flux reduction
p	Order of accuracy
P	Pressure $[kPa]$
P̄	Time-averaged pressure $[kPa]$
$\overline{P}$	Area-averaged static pressure $[kPa]$
p̄	Pressure fluctuation $[Pa]$
q	Wall heat flux $[W/m^2]$
Re	Reynolds number
r	Refinement factor
RANS	Reynolds-averaged Navier-Stokes equations
S	Strain rate $[]1/s]]$
$\mathbf{S_E}$	External energy source
$\mathbf{S_M}$	Momentum source
SST	Shear stress transport
t	Blade pitch $[mm]$
T	Temperature $[K]$
T_i	Inlet temperature $[K]$
TE	Trailing edge
U_i	i component of instantaneous velocity $[m/s]$
Ū$_i$	i component of time-averaged velocity $[m/s]$
u_i	i component of fluctuation velocity $[m/s]$
u,v,w	x,y,z components of velocity, respectively $[m/s]$
w	Squealer width $[mm]$
δ	Tip clearance gap height $[mm]$
$\oslash$	Predicted value of parameter
$\triangle$t	Timescale $[s]$
λ	Thermal conductivity $[W/m.K]$

τ_{ij}	Reynolds stress tensor $[m^2]$
ω	Turbulent frequency $[1/s]$
α_1	Inlet flow angle [degree]
α_2	Exit flow angle [degree]
α_i	Incidence angle [degree]
μ	Dynamic viscosity $[Pa.s]$
μ_t	Turbulent eddy viscosity $[m^2/s]$
ν	Kinematic viscosity $[kg/m.s]$

Subscripts

t	Total (stagnation) property
1	Domain inlet
2	Domain exit
aw	Adiabatic wall
w	Wall
c	Coolant

CHAPTER 1

INTRODUCTION

1.1 Motivation and Problem Definition

The term "turbo" in turbomachinery refers to the rotating machines, and the rotating disk with blades, "rotor", has a small gap between the tip and the casing called "tip clearance". This clearance gap causes momentum and total pressure loss as the flow passes through this region. The tip clearance in an axial turbomachinery typically lies in the range between 1 to 2 per cent [1] [2].

Rotors can be categorized as shrouded or unshrouded. The term shrouded means that an outer ring links the blades from their tip, circumferentially. This ring aims to prevent the fluid from flowing through the clearance gap. In aero engines, where rotors are unshrouded, the leakage flow is inevitable as the flow is not blocked by the ring. The tip leakage flow accounts for 1/3 of the total aerodynamic loss of a turbomachine, as it is stated by Denton [3].

The most of the research in this field relates the tip leakage flow with the thermal performance of a machine. Even though the phenomenon is more related to a thermal point of view since it directly affects the life expectancy and the thermal efficiency of the engine, the effects on the aerodynamic performance still requires answers to some specific questions, which are;

- Can aerodynamic efficiency be improved by making changes in the geometry?

- How much improvement in the aerodynamic efficiency can be obtained?

- What is the compromise when an improvement in aerodynamics is made in the

thermal efficiency? Is it worth it?

- Are there optimum spots on the blade tip to locate the cooling holes to make the turbine both aerodynamically and thermally more efficient?

- Which blade tip geometry provides a better performance?

- Which combination has better characteristics in terms of aerodynamics?

- Which combination has better characteristics in terms of heat transfer and cooling performance?

1.2 Thesis Scope and Outline

In this thesis, numerical calculations were first performed to validate the experimental cascade data sets and then, various configurations were solved numerically. Numerical simulations are performed in two parts in the thesis in stationary and rotational domains. The purpose of the study is to observe and investigate the complex, turbulent three-dimensional flow in the clearance gap and to examine the geometrical parameters affecting the tip leakage flow, and heat transfer with the goal of improving the aerodynamic and thermal efficiency through an improvement in the tip geometry and/or cooling configuration, where:

- the cooling configuration comprises of various combinations of location, size and number of cooling holes, and

- the tip geometry studied consists of flat and squealer types, with squealer type having different cavity depths.

The General Electric Energy Efficient Engine (E3) [4] first-stage high-pressure turbine blade was determined as suitable for the computational cases due to the availability of experimental data in literature. As was used in the experiments by Vetta et al. [5], only the tip profile of the blade is used for the stationary CFD study. The rotational domain is modeled by using the same geometry, but the dimensions are taken from Timko's report [4]. The problem to be solved is a real problem in today's aviation industry where the operational costs and fuel consumption need to be reduced

2

in order to increase the revenue while at the same time lowering the environmental pollution. Moreover, engines with less weight producing more power output are desired. From an economical point of view, engines need to become more efficient, and to achieve that the high-pressure turbine inlet temperature at the combustion chamber exit must be higher [6]. Last but not least, turbine blades' lifespan needs to be as high as possible since otherwise more frequent maintenance service and increase in overhaul costs are inevitable.

Modern gas turbine engine efficiencies are above 90%, which means that gaining further improvements in efficiency is even more challenging from now on. Achieving this is restrained by the so called flow phenomenon, "the tip leakage flow", that occurs in unshrouded axial turbomachinery. The pressure difference between the suction side (SS) and the pressure side (PS) drives the flow through the thin clearance gap above the blade tip. This gap is necessary since it prevents the rotor from rubbing against the casing, which otherwise would be catastrophic in flight operations. The amount of power extracted from the turbine decreases due to the tip leakage flow. The tip leakage vortex mixes up with the main flow and creates aerodynamic losses. Additionally, the high-temperature and high-momentum tip leakage flow causes critical thermal loads on the blade tip region, due to thin boundary layers, which requires sufficient cooling supply. High thermal loads reduce the lifespan of the blade causing erosion and deformation of the blade tip, especially in the high-pressure turbine (HPT). Hence, many cooling combinations are considered in literature and industry to endure these extreme thermal conditions. In tip cooling, relatively much cooler flow extracted from the compressor is blown over the tip through the holes and the blade tip is cooled. However, from an aerodynamical point of view, this application has its shortcomings, as several parameters affect aerodynamic performance of the blade tip.

The focus in this thesis is on the unshrouded turbine rotor blades. The geometrical parameters that affect the blade aerothermal performance are investigated. Although there are many studies investigating the blade tip aerodynamics or heat transfer separately, those studying the blade tip from both aspects are less in number. In these studies, mainly the parameters such as the blade tip geometry, clearance gap, and flow conditions have been investigated. In contrast, the studies focusing on the details of

3

the tip cooling configuration are scarce in literature. Additionally, only few studies focus on a cooled squealer tip under the effect of rotation. Besides, none of these studies consider the depth-to-width variation of a cooled blade tip cavity under rotation with a realistic rpm value and its effects on the thermal performance. All these aspects are investigated computationally through comparative analyses performed in the framework of this thesis.

1.3 Background

A wide range of research has been done regarding to this matter, some of which are presented here, and the parameters that affect the tip leakage flow and blade tip heat transfer will be investigated in detail. The tip leakage flow decreases the performance because the blade loading decreases due to the reduced mass flow rate and also the flow leaking through the gap mixes out with the passage flow causing a decrease in the energy as is stated by Heyes and Hodson [7]. Moreover, the leaking flow rolls up into a vortex in the blade passage which blocks the passage flow, therefore, it leads to a performance loss, as is described by Zhou and Hodson [8] in Figure 1.1.
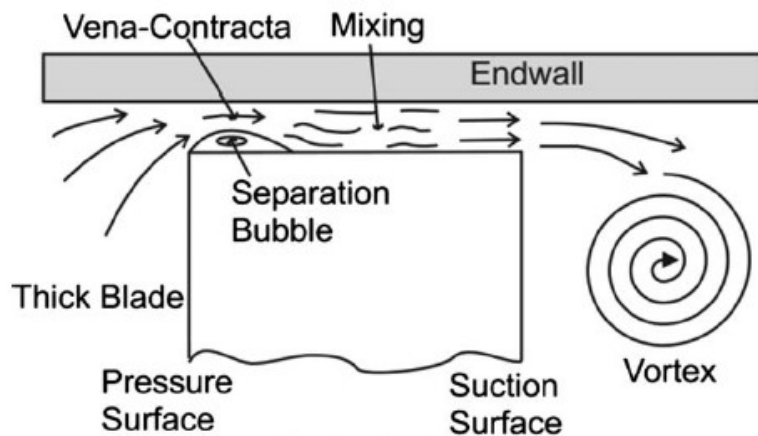
Figure 1.1: Two dimensional sketch of the tip leakage flow [8]

As Heyes and Hodson [7] discuss, most of the flat tip turbine blades experience the flow reattachment which extends to a large fraction of the chord. For thin blades, the reattachment occurs near the trailing edge. The tip clearance gap height is an important parameter since the flow separation is dependent on the expanding shear layer

4

that forms as the flow impinges on the pressure side, which affects the reattachment location. The tip clearances in typical engines are generally found to be 1-2% of the blade span [1], [2].
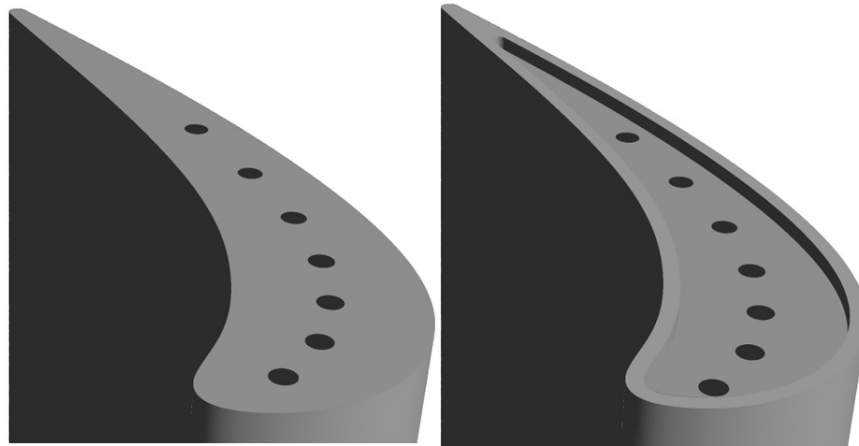
Figure 1.2: Turbine blade tip shapes: a) Flat, b) Squealer

Figure 1.2 shows the common blade tip geometries used in turbine blade tip research. The conventional type is the flat tip that has been investigated by the majority of the studies. The more recent type is the squealer tip where a groove is implemented on the top surface resulting in a tip shape with rims extending outward in the radial direction from the tip, surrounding the cavity floor fully or partially. Zhou and Hodson [8] found that the cooled cavity tip was the most efficient tip in terms of tip leakage loss compared to the suction side squealer (SSS) and flat tips. With relatively low blowing ratios (<0.5% of cascade inlet) and for a clearance gap of 1.6% of the chord, the SSS tip was the worst case in terms of aerodynamic performance. For higher blowing ratios (>0.5% of cascade inlet) and for the same clearance gap, the SSS tip, the flat tip with cooling holes placed underneath the separation zone corresponding to a location near the pressure side, and the flat tip with cooling holes placed underneath the reattachment zone along the camberline, all gave similar losses, while the cooled full-squealer tip produced a lower loss than the former flat tip configuration for all blowing ratios. Newton et al. [9] also showed that the flat tip with cooling holes placed underneath the separation zone exhibits much better thermal characteristics compared to the flat tip with holes underneath the reattachment zone at the same clearance gap. Zhou and Hodson [8] further investigated the effect of the clearance gap. As the blowing ratio increased, the tip leakage loss increased for all tip geome-

tries at all tip gaps. However, they showed that the amount of tip leakage loss was not proportional to the tip leakage mass flow rate. In this thesis, SSS blade tip was not investigated since Zhou and Hodson [8] have shown that it is the worst case. Tallman and Lakshminarayana [10] also investigated the effect of clearance gap height. Two different clearance heights were examined with a clearance-to-span ratio of 1% and 2.5%. The mass flow rate through the gap increased as the height increased. The increase in the mass flow rate was not linearly proportional to the height of the gap. The leakage vortex in the 2.5% height case was more detached, and the reduction in the clearance height resulted in a decrease in the average passage loss coefficient since the passage vortex gets larger as the clearance height increases. However, the flow across the smaller gap of 1% had larger local losses since the flow at the mid gap of the 2.5% case was more likely to be inviscid.

The tip leakage flow affects not only the aerodynamic performance, but also the thermal performance of the turbines. There exists numerous studies involving the blade tip geometry and its interaction with the tip leakage flow and tip heat transfer. In the experimental studies performed by Nho et al. [11] [12] on a five-bladed linear cascade, the tip profile of the E3 blade was examined in terms of both aerodynamics and heat transfer, respectively. The cascade setup had tip clearances of 1.5% and 2.3%. Various combinations of blade tip shapes including flat, squealer, partial squealer, dimpled and grooved shapes were of interest, and their findings were similar to those of Kwak and Han [13] from a thermal perspective. A reduction in Nusselt number was obvious when switched from flat to any carved type. Kwak and Han [13] carried out experiments on a squealer tip geometry having a cross section of the GE-E3 blade tip, and they found that the heat transfer coefficient over the blade tip was reduced when switched to squealer tip from flat tip. The tip floor heat transfer coefficient near the leading edge was higher than that for the trailing edge. Also, the tip floor heat transfer coefficient was lower than that for the rim. Nho et al. [11] concluded that increasing the clearance gap increased the loss due to leakage flow while diminishing the strength of the passage vortex. The squealer tips were found to be superior to their grooved, dimpled, flat and partial counterparts unless they were optimized in both aerodynamic and thermal points of view. In a research performed by Key and Arts [14], aerodynamic losses for different tip arrangements that were squealer and

flat tips were observed. It was an experimental study and experiments were carried out for various Reynolds numbers. When Reynolds number was increased, the aerodynamic tip losses were found to be increasing for a flat tip, contrary to the squealer tip where the tip losses were relatively insensitive to the changes in the Reynolds number. Naik et al. [15] studied partial and squealer turbine blade tips. They found that the full squealer tip was superior to its partial counterpart in both thermal and aerodynamic aspects. Newton et al. [16] showed that using the SSS instead of the flat tip resulted in an integrated net heat-flux reduction (NHFR) by 15% while the cavity tip revealed no NHFR reduction. Also, in the research done by Christophel et al. [17], it was found that increasing the tip gap increased heat transfer for the configuration with no blowing. Azad et al. [18], [19] carried out experiments on a cascade facility comprising of five blades with the GE-E3 blade profile with both squealer and flat tips; as was also studied in this thesis. The chord length of the blade was 86.1 mm, whereas in the study by Vetta et al. [5] it was 130 mm. Detailed pressure and temperature data were collected over the tip region. It was stated that the heat transfer coefficient on the tip leakage flow path was higher than that in the leading edge region. Also, the pressure side region was a high heat-transfer region due to the entrance effect. As the volume of the leakage flow increased, the heat transfer coefficient increased as a result. This was interpreted as the larger is the tip gap, the higher is the heat transfer coefficient. This behavior was also shown numerically by Krishnababu et al. [20]. They concluded that due to lower velocities inside the gap zone, the area-weighted averaged heat transfer coefficient on the blade tip floor was lower, decreasing the overall heat transfer coefficient on the tip surface. This conclusion is an outcome of the use of squealer-type blade tip geometries as they slow down the flow at the tip region. Nasir et al. [21] also compared various tip shapes including flat and squealer tips and showed that squealer tip produced lower overall heat transfer coefficients. Also observed is that flat tips produced higher heat transfer coefficients towards the trailing edge and lower heat transfer coefficients near the leading edge. The experiments performed by Kwak and Han [22] on a flat tip returned the highest heat transfer coefficients close to the pressure side of the tip where the flow separation and reattachment were causing this increase.

Location of cooling holes must be chosen wisely, otherwise one may end up with

spending the coolant air in the blade regions that do not need cooling. In literature, some of the studies emphasize the blade regions that need cooling. Firstly, the area at the forward tip region that has low heat transfer is named as "sweet spot" as mentioned by Bunker [23], and implementing a dense cooling scheme in this low heat-transfer region would be a waste of cooling. Secondly, it is shown in the study of Niu and Zang [24] that placing the holes as close as possible to the pressure side gives the best results; it reduces the amount of tip leakage flow and the associated losses, but also increases the strength of the passage vortex. Mercan et al. [25] conducted experiments on a flat tip, blowing from a row of holes placed along the camber line of a blade. They found that blowing from the holes in the upstream part was more effective than blowing from near the trailing edge. Only few studies associated with the aerodynamic performance of the tip blowing are present in the literature. The research done by Volino [26] stated that with a flat tip, blowing from the holes placed nearby the pressure side and inclining them toward the pressure side generally reduces the total pressure by reducing the tip leakage vortex effects. In the research, total of eleven holes were used on the cavity tip and the first five upstream holes were inclined at 45 degrees to the base of the squealer cavity. The next three holes were also inclined, but they had a lower length-to-diameter ratio due to the smaller blade thickness toward the trailing edge. With eleven holes, a blowing ratio of 1.4 increased the total pressure drop, and increasing it to 2.2 further increased the total pressure drop, although not as much. The total pressure drop due to tip leakage vortex was significantly reduced when seven holes were used at a blowing ratio of 2.2. The pressure drop due to passage vortex was observed to go up, and little change was observed from the no-blowing case overall. Mhetras et al. [27] experimentally studied film-cooling effectiveness on a cascade setup that was comprised of cutback squealer-shaped blades. Coolant air was blown off from the holes that were placed on both the cavity floor and the pressure side of the blade. It was concluded that the larger depth gave higher cooling effectiveness and that increasing the number of the cooling holes led to a better cooling management over the blade tip. Ma et al. [28] studied the thermal effects of coolant injection for a transonic cascade that included a full squealer turbine blade. They compared the effect of number of cooling holes on thermal characteristics comparing two configurations with five and nine holes. They concluded that the optimization of net heat-flux reduction was not guaranteed by adding more holes,

unless there was significant improvement in cooling effectiveness. They also showed that blowing near the pressure side resulted in a better film-cooling coverage zone over the tip, up to the suction side of the blade from the holes. Cheng et al. [29] conducted experiments to investigate the film-cooling coverage in a five-bladed cascade facility for a squealer turbine blade tip. They concluded that the cooling effectiveness over the blade tip was decreased by increasing the clearance gap and increased by increasing the blowing ratio. They did not study a configuration with holes located near the pressure side. Their study revealed that the most effective cooling hole arrangement among the examined configurations was the one with the holes clustered near the leading edge with the downtream holes placed along the camberline. Also, it was clearly stated that the worst thermal cooling performance was obtained with the one where the holes were located near the suction side.

Effect of rotation or relative cascade motion on the tip leakage flow is examined in some of the research. Tamunobere and Acharya [30] studied the effect of the blowing ratio on the heat transfer performance of a turbine blade operating in a rig rotating at 1200 rpm. The experiments showed that the relative motion pushed the film coolant coverage towards the suction side, while in the stationary case, the pressure side benefited the coolant more. It was also concluded that an increase in the blowing ratio increased the film-cooling coverage, over the blowing ratio range examined. As stated in the research carried by Palafox et al. [31], the relative motion of the cascade, which was provided by a moving belt, shifted the high Nusselt number distribution region and reduced the total averaged Nusselt number on the tip surface by up to 13.3%. It was also revealed that the relative motion shifted and weakened the high-velocity gradient near the pressure side. Tallman and Lakshminarayana [32] observed that the mass flow rate through the tip gap was decreased by 1% while the passage-averaged loss coefficient was increased by 4% under the effect of relative casing motion. From the leading edge to the mid chord region, near-casing secondary flow was enhanced by the direction of the relative casing motion as it was perpendicular to the primary flow direction. In the gap region, shear layer over the moving casing behaved as an obstacle to the leakage flow from the leading edge to the mid chord, which forced the majority of the leakage flow to leave the gap from its downstream half. On contrary to the fixed-wall simulations, they also found that most of the leakage flow passed

9

around and underneath the leakage vortex in the relative motion instead of rolling-up with it, with the vortex roll-up delayed further downstream. They concluded that this behavior led to the formation of a strong secondary flow in the spanwise direction and a reduction in the leakage vortex size by about 1/3 of the fixed-wall case. A study by Yang et al. [33] investigated the effect of the Coriolis and centrifugal forces on the tip leakage flow for both squealer and flat tips, again using the GE-E3 HP turbine blade tip profile. The results from the case with the relative casing motion was compared with those from a stationary cascade model. The Coriolis force was found to reduce the velocity near the leading edge while increasing it near the trailing edge. The relative motion of the casing also led to a significant increase in the averaged heat transfer coefficient over the flat blade tip whereas the centrifugal and the Coriolis forces reduced it. Acharya and Moreaux [34] studied numerically the effect of the relative motion between the casing and the blade either by moving the endwall or by rotating the blade itself, which resulted in Coriolis and centrifugal forces. However, the relative velocity of the endwall and the rotational speed of the blade considered were much lower compared to those at actual engine conditions. Their cut-back squealer tip geometry had six holes on the blade pressure side and two holes at the blade tip leading edge region, which is a different cooling configuration than those investigated in this thesis. The cavity depth and clearance gap were varied in the study. Though the differences between the relative motion and the rotating domain were not found to be significant as those between the stationary domain and the relative motion of the domain due to the low rotational speeds, the rotational cases still had higher velocity magnitudes in the cavity, directly leading to higher heat transfer coefficients. Rezasoltani et al. [35] performed both experiments and CFD runs under different rotational speeds and blowing ratios for squealer and flat tips. The cooling holes were placed on the cavity floor and by the pressure side for the cooling purposes of the tip region. Their work showed that the cooling effectiveness increased with increasing the blowing ratio. However, the effectiveness decreased with increasing the rotational speed for the squealer tip, which was the opposite behavior observed in the flat case. Although it is important to include the rotation effects in the analyses to mimic the actual engine environment, two separate studies, one from Mayle and Metzger [36] and the other from Coull and Atkins [37] gave some additional insight. From the experimental study in [36], it was stated that the rotation effect could be neglected

as long as the flow conditions were matched. Also the study of [37] concluded that both the relative casing motion and the inlet flow profile had negligible effects on the tip leakage flow, separately. However, the combination of those two effects changed the results undeniably. Saul et al. [38] investigated both numerically and experimentally the thermal characteristics with varying the clearance gap and blowing ratio for a squealer tip. The relative casing motion was taken into account with the use of CFD, but only for the uncooled cases. They concluded that the relative motion led to a decrease in the heat transfer coefficient near the blade leading edge while increasing along the chord due to the flow impingement on the cavity floor.

For the squealer tip, Bunker and Bailey [39] performed experiments to study the effect of cavity depth on the convective heat transfer coefficients over the blade tip surface. Uniform heat transfer coefficient over the cavity bottom was obtained for a cavity-to-depth ratio of 0.67. Locally averaged heat-transfer coefficients over the tip surface were found to be decreasing almost linearly as depth-to-width ratio increased. Yang and Feng [40] investigated the effect of clearance height and groove depths on the tip leakage flow and heat transfer. GE-E3 HP turbine blade geometry was used in the CFD analyses, with the relative casing motion also being modeled. The depth of the tip groove had an impact on reducing the tip leakage flow, up to 3% of groove depth-to-blade span ratio. Further increase in the groove depth did not change the amount of the tip leakage loss. It was also stated that an increase in the groove depth decreased the averaged heat transfer rate on the tip surface while a combination with an increase in the gap height resulted in the opposite behavior. Ameri et al. [41] numerically investigated the effects of tip recess levels on blade tip heat transfer characteristics under the effect of rotation for uncooled flat and squealer tips. The heat transfer rate on the shroud was observed to be higher for the flat tip compared to squealer tips. Zhou [42] also performed computations to examine the effect of cavity depth and width on the thermal performance of a rotating blade with a squealer tip. Cooling of any kind was out of scope in the study, so no cooling arrangements were present. The results revealed that cavity-scraping vortex was formed in the rotational domain, which was not observed in its stationary counterpart. Due to rotation, a low Nusselt-zone appeared on the cavity floor, which then disappeared as the height of the squealer increased. The height of the squealer was concluded to be directly

11

controlling the size of the cavity vortex and the cavity-scraping vortex. Wang et al. [43] conducted experiments on an experimental facility where the GE E3 blade tip profile was used. In the study, the rim width was varied while the cavity depth was held constant. Flow acceleration was observed along blade suction side from the leading edge up to 65% of the chord, as the volume of the cavity groove was increased. This increase was achieved by either increasing the cavity depth or by decreasing the rim width. Beyond that point, the flow decelerated towards the trailing edge. When the coolant flow was introduced, however, the acceleration was observed to be all the way from the blade leading edge to the trailing edge, and the cavity depth affected the tip pressure distribution more than the rim width since it was behaving like a labyrinth seal. Kwak et al. [44] conducted experiments at the same facility as in [13]. Experiments were performed for three different tip gaps and three different rim heights. They investigated the effects of the location and the height of the blade rim. They observed a reduction in the heat transfer coefficient on both the blade tip and the shroud as the cavity depth was increased. Also, when compared to the full squealer tip, the partial rim geometry placed along the suction side was observed to reduce heat transfer more.

1.4 Loss Mechanisms in Turbomachinery

In this section, the fundamentals of loss mechanisms occurring in axial turbomachinery are explained in brief.

1.4.1 Fundamentals of Loss Sources

Loss can be defined as an increase in entropy and a reduction in total pressure. Main sources of entropy generation in fluid mechanics are: viscous effects in boundary layers, viscous effects in mixing, shock waves and heat transfer.

Before continuing with the definitions, the loss definition is introduced first. There are various loss coefficient definitions for blade rows in the literature. In his famous paper, J.D. Denton [3] explains the loss mechanisms in turbomachines in detail, and this explanation will be briefly provided here in this section. The enthalpy-entropy

relation for turbine cascade flow is demonstrated in Figure 1.3. Here, stations 1 and 2 represent the inlet and exit to the blade row, respectively.
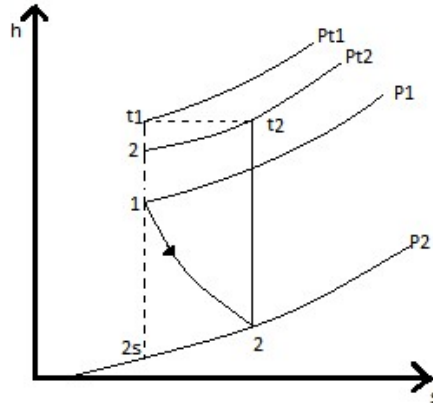
Figure 1.3: Enthalpy vs entropy curve for turbine cascade flows

According to Denton [3], the most common loss definition is the stagnation pressure loss coefficient and it is defined as:

$$\zeta = \frac{P_{t1} - P_{t2}}{P_{t2} - P_2} \tag{1.1}$$

where P_t is the total pressure P is the static pressure, and the subscripts 1 and 2 refer to the stations shown in Figure 1.3. The calculation of the loss coefficient based on Eq. (1.1) is straightforward since the quantification of pressure is best done in cascade tests. For design processes, a more convenient loss coefficient definition is introduced by the following equation, for a turbine blade:

$$\zeta = \frac{h_2 - h_{2s}}{h_{t2} - h_2} \tag{1.2}$$

where h is the enthalpy, and the subscripts t and s define the total and isentropic values, respectively.

There exist many other loss coefficient definitions for turbine cascades. They were compared by Brown [45] and it was concluded that the loss coefficient for energy is most likely to remain constant as the Mach number changes.

The loss coefficients given by Equation (1.1) and (1.2) are best suited for cascade

13

flows whereas the flows in a rotating media are susceptible to the changes in pressure or enthalpy variation along the blade radius. For such flows, the isentropic efficiency definition is used which is given by the following equation:

$$Isentropic\ Efficiency = \frac{Actual\ Work}{Isentropic\ Work} \qquad (1.3)$$

The "isentropic work" is the work extracted through a turbine stage in which the flow undergoes an isentropic, i.e. adiabatic and reversible, process. When all of the losses are taken into account, it becomes the "actual work" as the name suggests.

Variations from this efficiency is due to the entropy generation resulting from either heat transfer or thermodynamic irreversibility. Entropy can be calculated by thermodynamic properties and it is given by the following equations:

$$s - s_{ref} = Cp \ln\left(\frac{T}{T_{ref}}\right) - R \ln\left(\frac{P}{P_{ref}}\right) \qquad (1.4)$$

or

$$s - s_{ref} = Cv \ln\left(\frac{T}{T_{ref}}\right) - R \ln\left(\frac{\rho}{\rho_{ref}}\right) \qquad (1.5)$$

Here s denotes the entropy, and R is the ideal gas constant. Cv and Cp are the specific heats in constant volume and constant pressure, respectively. Subscript ref is used for reference values.

In this thesis, the loss coefficient will be used for comparisons between the configurations and their relative total pressure changes will be presented. The loss analysis was performed for the cases in the stationary domain. The modified version of Eq. (1.1) is used for the comparative analysis as given by the following equation:

$$\xi = (P_{t1} - P_t)/P_{t1} \qquad (1.6)$$

Here, the local total pressure, P_t, across the tip clearance gap is compared with the total pressure at the cascade inlet, P_{t1}.

14

1.4.2 Definitions of Loss Mechanisms

Up to now, various loss calculations, which are suggested by Denton [3] based on the entropy in detail, are presented. The definitions of loss types will be given next.

In the famous paper of J.D. Denton [3], loss occuring in turbomachinery is categorized in three types as follows:

1. Profile Loss

2. Endwall Loss

3. Tip Leakage Loss

The profile loss is typically defined as the loss generated in the blade boundary layer away from the wall. In general, the loss predictions can be based on cascade tests since the flow here is assumed to be two dimensional.

The endwall (secondary) loss arises partly from the secondary flows that are generated by the annulus boundary layers passing through a blade row. However, a combination of other factors may also generate secondary losses, making it difficult to distinguish between the secondary losses and the other types of losses. As is stated by Denton in [3], the term "secondary loss" is also considered to include all kinds of losses. The tip leakage loss is due to the flow leaking over the rotor blade tips and the stator hub clearances due to the pressure gradient between the suction and pressure sides of a blade. In many turbomachines, these three losses are comparable in magnitude, and each one is taken to account for 1/3 of the total loss. Reduction in any one of these losses will result in a performance gain. In this thesis, only the tip leakage flow and its consequences will be examined.

1.4.3 Review of Tip Leakage Flow

A tentative sketch of formation of the tip leakage flow is given by Bindon [46] and is presented in Figure 1.4:
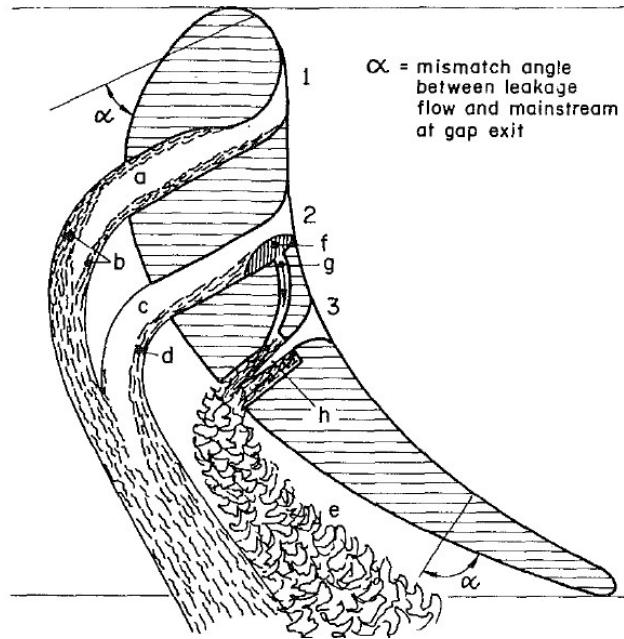
Figure 1.4: Conceptual sketch of various flow types in tip clearance [46]

Bindon [46] explains various types of leakage flow leaking through the clearance over a blade tip by depicting them with three channels as shown in Figure 1.4. A normal boundary layer with no separation is given by channel 1, and it is given a convergent-divergent shape to represent the pressure distribution affected by the blockage of the separation bubble. This happens upon mixing of the mainstream flow with the tip leakage flow as there is a mismatch angle for both the core flow a and wake b. In channel 2, there is a separation bubble f included, and the leakage flow in this case is formed by the reattachment wake d and the core flow c. Channel 3 is shaped differently than the other two and acts as a single-point ejector through which it exhausts the separation bubble fluid g over to the suction side, in addition to the jet flow h. Momentum is added to the stagnant fluid g by the mixing process of the jet h in order to escalate in the pressure gradient to the clearance exit. An entrainment wake e is created by the suction side and contributes to most of the mixing loss.

1.5   Blade Tip Film Cooling

Tip cooling of blades is managed by injection of cooling air through the holes placed at the blade tips. Cooling air must be at a sufficiently lower temperature relative to

the blade's metal temperature and mainstream temperature, which are high especially in high-pressure turbines, in order to be able to cool the blade surfaces properly. This explains the need for cooling in order to improve the life expectancy and to reduce the overhaul costs of turbine blades. As the literature introduced in Section 1.3 shows, there are many challenges that need to be tackled for a successful blade cooling design. Providing a uniform coolant coverage is almost impossible, because the pressure differential across the blade surfaces causes the tip leakage flow over the blade tip that also transports the coolant flow with it from the blade pressure side to its suction side across the clearance gap. When the holes are placed in the vicinity of the separation zone, the coolant flow tends to lift-off from the surface due to the separated flow, and the performance of the film-cooling coverage is adversely affected. Also, some portions of the blade tips may not be easy to cool even in abundance of coolant flow. Blowing more air mass into the clearance gap may result in higher loss levels since additional cooling air adds up to the present leakage flow and to the resulting loss along with it.

The thermal characteristics for blade tip cooling can be quantified by examining parameters such as the heat transfer coefficient and the film-cooling effectiveness over the tip. The heat transfer coefficient is calculated by the following equation:

$$h_c = q_w/(T_{aw} - T_w) \tag{1.7}$$

where T_{aw} is the adiabatic wall temperature, T_w is the wall temperature, and q_w is the heat flux at the wall. Due to high thermal loads, the high heat transfer coefficient zones are more prone to material loss known as erosion. The film-cooling coverage over a surface is evaluated by film cooling effectiveness, which measures how well the surface is cooled and is defined by:

$$\eta = \frac{T_{inlet} - T_{aw}}{T_{inlet} - T_c} \tag{1.8}$$

Tip cooling is affected by many parameters, some of which are the coolant mass flow rate, the blade tip geometry, the clearance gap height, and the arrangement of the cooling holes. The cooling mass flow rate has a dominant effect on the heat transfer coefficient and the film-cooling effectiveness over the blade tip since it interacts with both the hot mainstream and hot metal surfaces. The clearance gap height and the

blade tip geometry (i.e tip type, squealer rim dimensions, etc.) affect the pattern of the tip leakage flow across the clearance gap. Such geometric parameters can be used in the design of the turbine blade tip to control flow phenomena such as the reattachment point of the leakage flow and the size of the passage vortex to delay the vortex roll-up in the passage. These changes in the flow pattern all affect the distribution of the heat transfer coefficient and the cooling effectiveness at the blade tip.

CHAPTER 2

NUMERICAL MODELING OF THE FLOW

In this chapter, the numerical method and the computational domains will be explained in detail.

2.1 Governing Equations

In solving fluid mechanics problems, the three dimensional flow is governed by mass, momentum and energy equations, namely the Navier-Stokes equations which are the type of non-linear partial differential equations and are given in the differential form as follows:

$$\frac{\partial \rho}{\partial t} + \frac{\partial \rho u}{\partial x} + \frac{\partial \rho v}{\partial y} + \frac{\partial \rho w}{\partial z} = 0 \tag{2.1}$$

$$\frac{\partial \rho u}{\partial t} + \frac{\partial \rho uu}{\partial x} + \frac{\partial \rho uv}{\partial y} + \frac{\partial \rho uw}{\partial z} = -\frac{\partial p}{\partial x} + \frac{1}{Re}\left(\frac{\partial \tau_{xx}}{\partial x} + \frac{\partial \tau_{xy}}{\partial y} + \frac{\partial \tau_{xz}}{\partial z}\right) \tag{2.2}$$

$$\frac{\partial \rho v}{\partial t} + \frac{\partial \rho uv}{\partial x} + \frac{\partial \rho vv}{\partial y} + \frac{\partial \rho vw}{\partial z} = -\frac{\partial p}{\partial y} + \frac{1}{Re}\left(\frac{\partial \tau_{xy}}{\partial x} + \frac{\partial \tau_{yy}}{\partial y} + \frac{\partial \tau_{yz}}{\partial z}\right) \tag{2.3}$$

$$\frac{\partial \rho w}{\partial t} + \frac{\partial \rho uw}{\partial x} + \frac{\partial \rho vw}{\partial y} + \frac{\partial \rho ww}{\partial z} = -\frac{\partial p}{\partial z} + \frac{1}{Re}\left(\frac{\partial \tau_{xz}}{\partial x} + \frac{\partial \tau_{yz}}{\partial y} + \frac{\partial \tau_{zz}}{\partial z}\right) \tag{2.4}$$

$$\frac{\partial E_t}{\partial t} + \frac{\partial(uE_t)}{\partial x} + \frac{\partial(vE_t)}{\partial y} + \frac{\partial(wE_t)}{\partial z} =$$
$$- \frac{\partial(up)}{\partial x} - \frac{\partial(vp)}{\partial y} - \frac{\partial(wp)}{\partial z} - \frac{1}{RePr}\left(\frac{\partial q_x}{\partial x} + \frac{\partial q_y}{\partial y} + \frac{\partial q_z}{\partial z}\right)$$
$$+ \frac{1}{Re}\left(\frac{\partial}{\partial x}(u\tau_{xx} + v\tau_{xy} + w\tau_{xz})\right.$$
$$+ \frac{\partial}{\partial y}(u\tau_{xy} + v\tau_{yy} + w\tau_{yz}) + \left.\frac{\partial}{\partial z}(u\tau_{xz} + v\tau_{yz} + w\tau_{zz})\right)$$

(2.5)

where Eq. (2.1) is mass, Eqs. (2.2), (2.3), (2.4) are momentum and Eq. (2.5) is energy conservation equations. The solution of these equations gives insight to the behavior of fluid at that particular point and time. In order to have a "closed-system", there is a need for the sixth equation since the number of unknowns is six. The system of equations can be closed by introducing the following equation, the ideal gas law:

$$P = \rho RT \qquad (2.6)$$

2.1.1 Reynolds-Averaged Navier-Stokes Equations

Brief explanation to Reynolds-Averaged Navier-Stokes equations are given here, since they are employed throughout the analyses. The solution of the averaged form of N-S equations gives highly accurate results for the time-averaged flow field, especially in steady-state problems. The N-S equations are decomposed into averaged and fluctuating components as given in the following relation:

$$U_i = \overline{U_i} + u_i$$
$$P = \overline{P} + p \qquad (2.7)$$

The averaged component is given by the following equation:

$$\overline{U_i} = \frac{1}{\triangle t}\int_t^{\triangle t + t} U_i dt \qquad (2.8)$$

20

where timescale $\triangle t$ is large enough, relative to the fluctuations but smaller than the timescale at which the equations are solved.

The Reynolds-Averaged Navier Stokes (RANS) equations are presented next. So as to provide tidiness of the equations, they only are given in one dimension to steer clear of confusion and they are analogous in each direction.

$$\frac{\partial \rho}{\partial t} + \frac{\partial (\rho U_j)}{\partial x_j} = 0 \tag{2.9}$$

$$\frac{\partial (\rho U_i)}{\partial t} + \frac{\partial}{\partial x_j}(\rho U_i U_j) = -\frac{\partial p}{\partial x_i} + \frac{\partial}{\partial x_j}(\tau_{ij} - \rho \overline{u_i u_j}) + \mathbf{S}_M \tag{2.10}$$

$$\frac{\partial \rho h_{tot}}{\partial t} - \frac{\partial p}{\partial t} + \frac{\partial}{\partial x_j}(\rho U_j h_{tot}) = \frac{\partial}{\partial x_j}(\lambda \frac{\partial T}{\partial x_j} - \rho \overline{u_j h}) + \frac{\partial}{\partial x_j}[U_i(\tau_{ij} - \rho \overline{u_i u_j})] + \mathbf{S}_E \tag{2.11}$$

where Eq. (2.9) is for mass conservation and Eq. (2.10) is for momentum conservation. The term $\mathbf{S}_M$ represents the additional momentum source. Eq. (2.11) is energy equation written in terms of total energy. The term $\mathbf{S}_E$ represents the external energy source. The averaging process of the energy and the momentum equations brings about the non-linear convective term. This term leads to the famous "closure problem" since there are six equations while seven unknowns are present [47]. The mass conservation equation is not affected by the Reynolds stress, due to the absence of the non-linear convective term. Eqs. 2.9-2.11 represent the most general form of the RANS equations including the time-derivative terms. In this study, steady-state computations were performed, meaning that those terms were neglected in the calculations.

The Reynolds stress term reflects the enhancement in the mixing that occur due to turbulent velocity fluctuations and is in greater amount than the enhancement caused by thermal fluctuations at the molecular level.

At high Reynolds numbers, mean free path thermal fluctuations occur over a much smaller length scale than the turbulent velocity fluctuations, therefore, the turbulent

fluxes are of greater importance than the molecular fluxes in calculating the total fluxes. This term is given by the following equation:

$$-\rho \overline{u_i u_j} = \mu_t \left(\frac{\partial U_i}{\partial x_j} + \frac{\partial U_j}{\partial x_i} \right) - \frac{2}{3} \delta_{ij} \left(\rho k + \mu_t \frac{\partial U_k}{\partial x_k} \right) \delta_{ij} \qquad (2.12)$$

The Spalart-Allmaras, k-ε, and k-ω models are the eddy viscosity models. Spalart-Allmaras is a one-equation model and kinematic eddy viscosity is calculated by solving the modeled transport equation [48]. The Spalart-Allmaras model is widely used in aerospace applications in which wall-bounded flows are present. The two-equation turbulence models, which are k-ε and k-ω models, solve two separate transport equations. The k-ε model is based on the two transport equations which are the k and ε. It is only valid for fully-turbulent flows since molecular viscosity effects are ignored in the derivation of the model [49]. The model is quite useful where pressure gradients are small and it predicts the flow away from walls with a high accuracy. The k-ω model is based on two model transport equations which are k and ω. This model is capable of predicting the flows close to walls. The shear stress transport (SST) k-ω model blends the k-ω and k-ε models to combine the ranges in which the equations perform at their best. For that reason, the SST model is implemented in the CFD runs performed in this thesis.

2.1.2 Shear Stress Transport Model

Since Menter's Shear Stress Transport (SST) model [50] is used throughout the CFD analyses, the closure model is given in detail in this section. The model is built on the baseline (BSL) k-ω model that utilizes the kf-ε model away from the surface and the k-ω model near the surface. The BSL k-ω model is given in the following equations:

$$\frac{\partial(\rho k)}{\partial t} + \frac{\partial}{\partial x_j}(\rho U_j k) = \frac{\partial}{\partial x_j}[(\mu + \frac{\mu_t}{\sigma_{k3}})\frac{\partial k}{\partial x_j}] + P_k - \beta' \rho k \omega + P_{kb} \qquad (2.13)$$

$$\frac{\partial(\rho\omega)}{\partial t} + \frac{\partial}{\partial x_j}(\rho U_j \omega) = \frac{\partial}{\partial x_j}[(\mu + \frac{\mu_t}{\sigma_{\omega 3}})\frac{\partial \omega}{\partial x_j}] + (1 - F_1)2\rho\frac{1}{\sigma_{\omega 2}\omega}\frac{\partial k}{\partial x_j}\frac{\partial \omega}{\partial x_j}$$
$$+ \alpha_3\frac{\omega}{k}P_k - \beta_3\rho\omega^2 + P_{\omega b} \qquad (2.14)$$

Here, k is the turbulent kinetic energy, ω is the turbulent frequency, μ_t is the turbulence viscosity, P_k is the production rate of turbulence, and P_{kb} and P_{wb} are the buoyancy production terms that were neglected in this study since a buoyancy model was not used in the computations. The time-derivatives in these equations were also neglected due to the steady-state analyses performed. The coefficient α in the buoyancy production term P_{wb} is also replaced by the new coefficient α_3. A linear combination of the corresponding coefficients gives the new model, as provided by the following equation:

$$\phi_3 = F_1\phi_1 + (1 - F_1)\phi_2 \qquad (2.15)$$

Model coefficients are defined as the followings:

$\beta' = 0.09$, $\alpha_1 = 5/9$, $\beta_1 = 0.075$, $\sigma_{k1} = 1.176$, $\sigma_{omega1} = 2$
$\alpha_2 = 0.44$, $\beta_2 = 0.0828$, $\sigma_{k2} = 1$, $\sigma_{omega2} = 1/0.856$

In the Shear Stress Transport (SST) model, the BSL k-ω model is modified to introduce a better way of modeling the eddy-viscosity. The remedy for over-prediction of the eddy-viscosity is to use a limiter function as defined in the following equations:

$$\nu_t = \frac{\alpha_1 k}{max(\alpha_1\omega, SF_2)} \qquad (2.16)$$

$$\nu_t = \frac{\mu_t}{\rho} \qquad (2.17)$$

S is an invariant measure of the strain rate and F_2 is a blending function, similar to F_1. The limiter function is restricted to the wall boundary layer with the use of F_2.

Also, the production term P_ω is given by the next equation, which differs from the k-ω formulation:

$$P_\omega = (\frac{\alpha_3}{\nu_t})P_k \tag{2.18}$$

Blending functions, F_1 and F_2, are of vital importance for the success of the model. Their formulation is based on the flow variables and the distance to the nearest surface. The blending function F_1 is defined by the following equations:

$$F_1 = \tanh(arg_1^4) \tag{2.19}$$

$$arg_1 = min\left(max\left(\frac{\sqrt{k}}{\beta'\omega y'}, \frac{500\nu}{y^2\omega}\right), \left(\frac{4\rho k}{CD_{k\omega}\sigma_{\omega 2}y^2}\right)\right) \tag{2.20}$$

where y is the distance to the nearest wall, ν is kinematic viscosity and $CD_{k\omega}$ is defined by the following equations, which give the definition for the blending function F_2:

$$CD_{k\omega} = max\left(2\rho\frac{1}{\sigma_{\omega 2}\omega}\frac{\partial k}{\partial x_j}\frac{\partial \omega}{\partial x_j}, 1x10^{-10}\right) \tag{2.21}$$

$$F_2 = \tanh(arg_2^2) arg_2 = max\left(\frac{2\sqrt{k}}{\beta'\omega y'}, \frac{500\nu}{y^2\omega}\right) \tag{2.22}$$

$$arg_2 = max\left(\frac{2\sqrt{k}}{\beta'\omega y'}, \frac{500\nu}{y^2\omega}\right) \tag{2.23}$$

2.2 Numerical Discretization

ANSYS CFX [51] is utilized in the analyses, since it is capable of solving complex problems with high accuracy and is widely used in turbomachinery industry. CFX discretizes the governing equations with an element-based finite volume method approach. CFX is a fully implicit coupled solver. In the thesis, the flow is compressible,

which is activated in the solver by using air as an ideal gas and the energy equation is solved by enabling the total energy option. Viscous and convective fluxes are discretized using the second order approach. Solution domain, which is constructed with an unstructured mesh since the geometry is complex, is split into control volumes. Control volumes are small volume elements in which the flow and flux variables are calculated by discretizing the integral form of the N-S equations. Figure 2.1 demonstrates a two dimensional control volume, but the solution of the three dimensional one is analogous to that of the two-dimensional one.
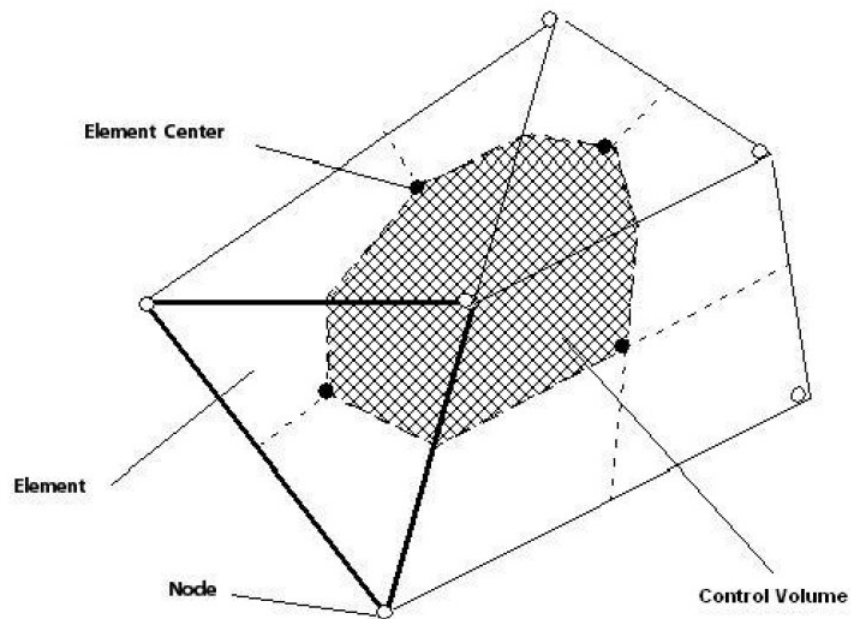
Figure 2.1: Definition of control volume [51]

Nodes are the points where all fluid properties and solution variables are stored. The shaded area in Figure 2.1 represents the control volume, it is constructed around each mesh element by intersecting the bisectors of the edges and the center of the elements.

2.3 Computational Domain

Three different computational domains are used since the thesis includes both rotational and cascade (stationary) CFD configuration studies and validation runs. Before starting with the analyses, the solver and the modeling approach are validated against the experimental data.

To summarize analysis steps in brief; three different scaled versions of the same turbine blade tip profile of the GE E3, are used:

- Blade 1: is used to validate the CFD approach and the solver for the midspan static pressure coefficient distributions. Also, the same geometry is used for the cascade configuration runs.

- Blade 2: is used to validate the CFD approach and the solver for heat transfer for both flat and squealer tips. Therefore, for this step, there were two different blade tips modeled with the same blade geometry.

- Blade 3: is used for the rotational domain solutions where the cavity depth of the squealer tip was examined.

The dimensions of each domain are given in Table 2.1.

Table 2.1: Blade dimensions for each domain

	Blade 1	Blade 2	Blade 3
Axial Chord(mm), C_x	130	86.1	28.7
Span(mm), h	152.4	122	42.7

2.3.1 Domain 1

The first domain is used for all runs in the stationary cases for the cooling configuration study on the blade tip. It is validated against the experimental data of Vetta et al. [5] that were obtained from the NASA's Transonic Turbine Blade Cascade Facility. The details of the cascade are given in Table 2.2.

This cascade did not involve tip clearance. The experiments provide pressure data and this data is used as a benchmark to validate the mesh and the problem setup. The domain is extended to C_x =130 mm ahead of the leading edge and 195 mm (1.5 C_x) downstream of the trailing edge to prevent backflow into the computational domain. A passage of the middle blade is modeled and periodic boundary conditions are imposed along the walls across the pitch direction to provide flow periodicity. No-slip

Table 2.2: Cascade parameters for the first validation study [5]

Inlet angle, α_1	29.7°
Incidence angle, α_i	29.1°, 9.1°, -11.4°, -46.5°
Exit angle, α_2	64.4°
Axial chord C_x	130 mm
Span, h	152.4 mm
Pitch/axial chord ratio, t/C_x	1

wall boundary conditions are imposed on the endwalls and the blade surfaces. Since the flow regime is compressible, inlet total pressure boundary condition is applied at the inlet and static pressure exit boundary conditions are defined at the exit. The boundary conditions and the results of the validation runs are discussed in 3.1.
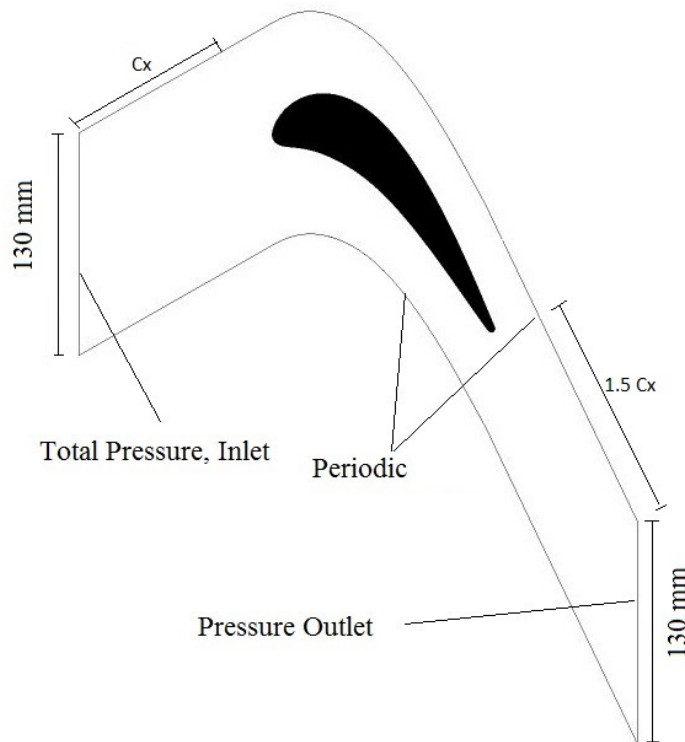
Figure 2.2: View of numerical domain for the first validation study

After the validation, tip coolant holes and clearance gap are introduced into the model. Also, a squealer tip is examined in the cooling configuration study. The detailed boundary conditions of that study are given in Section 4.2, and its results are presented

in Section 4.4.1 and 4.4.2. The domain parameters for the configuration study is given in Table 2.3, and its computational domain is depicted in Figure 2.3.

Table 2.3: Cascade parameters for configuration study

Inlet angle, α_1	29.7°
Exit angle, α_2	64.4°
Axial chord C_x	130 mm
Span, h	152.4 mm
Pitch/axial chord ratio, t/C_x	1
Tip clearance, δ	3 mm, 2%
Rim height, for squealer tips	3 mm
Rim width, for squealer tips	3 mm
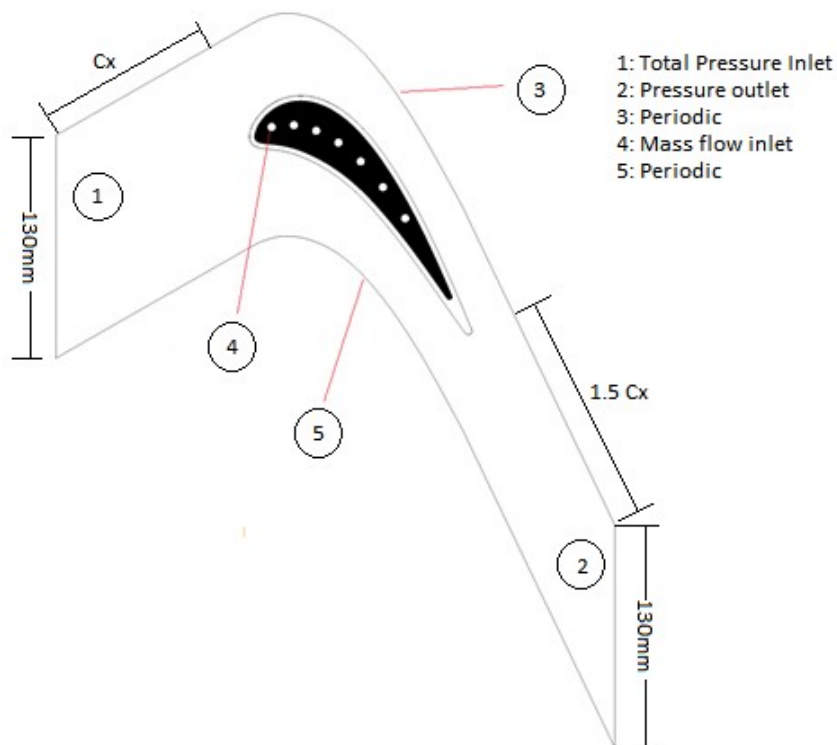
Figure 2.3: View of numerical domain for configuration study

In the configuration study, all holes are either located along the camber line or close to the pressure side by moving each of them by 7 mm in the pitch direction, towards the pressure side. 7 and 4-holed configurations are examined in this thesis. Location

28

of the holes is given in Table 2.4 as measured from the leading edge of the blade. All seven holes are deployed in the 7-holed configurations as the name suggests, whereas only the odd numbered holes 1-3-5-7 are used in the 4-holed configurations.

Table 2.4: Hole locations for configuration study

	Hole 1	Hole 2	Hole 3	Hole 4	Hole 5	Hole 6	Hole 7
x/C_x	0.1	0.2	0.3	0.4	0.5	0.6	0.7

2.3.2 Domain 2

The reason why the second computational domain was required is because the validation of the tip flow is necessary. The first domain described in Section 2.3.1 validates only the midspan flow, and no tip data were available in those experiments. Most of the flow solvers are good at capturing the flow features at the midspan, but the more compelling task is to accurately model the tip leakage flow which is a more complex flow region than that at the midspan. The data obtained from the experimental setup used by Azad et al. [18],[19] and by Kwak and Han [13], [22] are used in this section as a benchmark to validate the tip flow. Even though the cascade is comprised of squealer tips in [19], [13] the dimensions of the experimental setups for all these studies were the same. The cascade parameters are given in Table 2.5 Therefore, there were two different validation studies performed here, one for the flat tip [22] and one for the squealer tip [13].

Table 2.5: Cascade parameters for the second validation study [22]

Inlet angle, α_1	32°
Exit angle, α_2	65.7°
Axial chord C_x	86.1 mm
Span, h	122 mm
Pitch/axial chord ratio, t/C_x	1.06
Tip clearance, δ	1.97 mm, 1.5%

The squealer tip geometric parameters are given below, according to [13].

- Width of squealer rim = 2.29 mm

- Depth of cavity (or squealer height)= 5.08 mm

The schematic of the cascade is given in Figure 2.4.
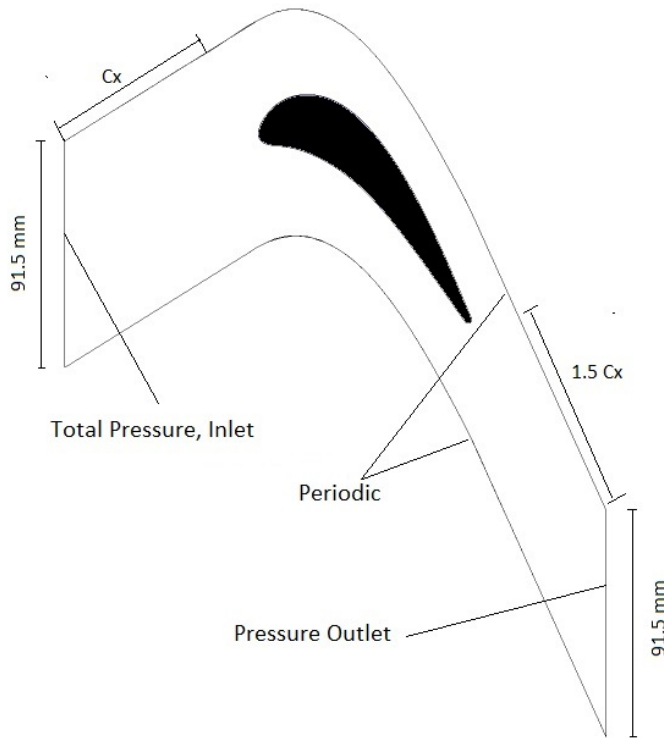
Figure 2.4: View of numerical domain for the second validation study

2.3.3 Domain 3

The third domain used is the actual -which is annular- rotor model of the GE E3 rotor blade, which is reported by Timko [4]. The second part of the configuration study in Chapter 5, examines the effect of rotation and the squealer parameter depth-to-width ratio on the tip aerothermodynamics. Although three different profiles at the hub, midspan and tip were available for the blade, only the tip profile is used in the study since the main concern is on the leakage flow. Thus, the blade twist was not modeled. Squealer tip geometries with realistic width-to-depth ratios are used. The side view of the HPT flow path is depicted in Figure 2.5.

30
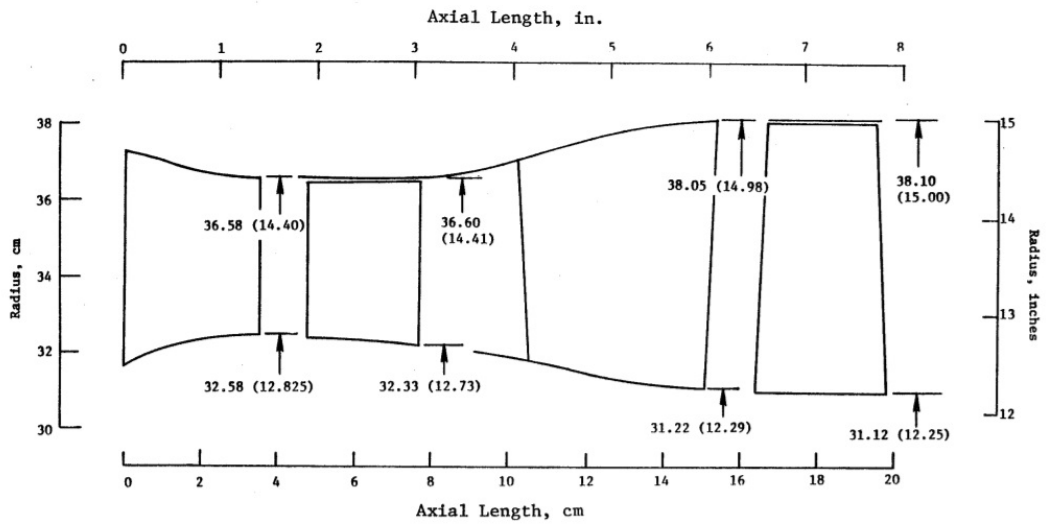
Figure 2.5: High pressure turbine aerodynamic flowpath [4]

The view of E3 HPT blade is shown in Figure 2.6.
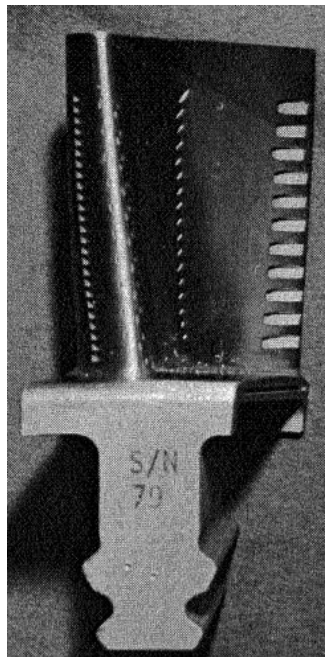
Figure 2.6: High-pressure turbine first-stage blade [4]

The rotor of the first stage comprised of 76 blades. Annular domain dimensions can be seen in Figure 2.6. In the study, only one blade of the first stage rotor is modeled. Rotational periodicity is imposed along the boundaries in the circumferential direc-

Table 2.6: Domain parameters for rotational study

Inlet angle, α_1	75.4°
Axial chord C_x	28.7 mm
Span, h	42.7 mm
Pitch/axial chord ratio, t/C_x	1.06
Tip clearance, δ	0.427 mm, 1%
Squealer width, w	0.662 mm
Squealer depth, d	0.662, 1, 1.325 mm
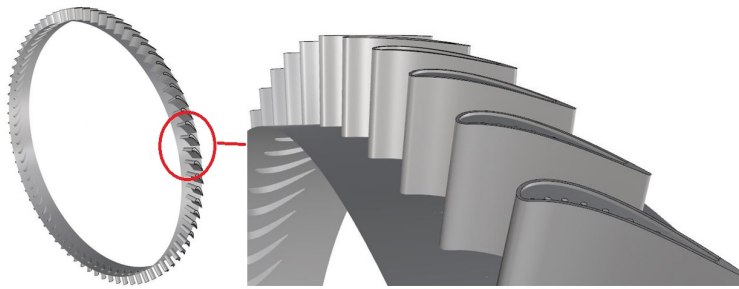
Figure 2.7: 3D model of high pressure turbine rotor

tion. In order to have a realistic domain, the inlet flow angle is taken as the angle of the wake coming out of the stator.

The details of the domain is given in Table 2.6, and the 3-D model of the domain is given in Figure 2.7. The fluid domain's used in the computational study in Figure 2.8, which is generated with respect to the dimensions given in Figure 2.5.
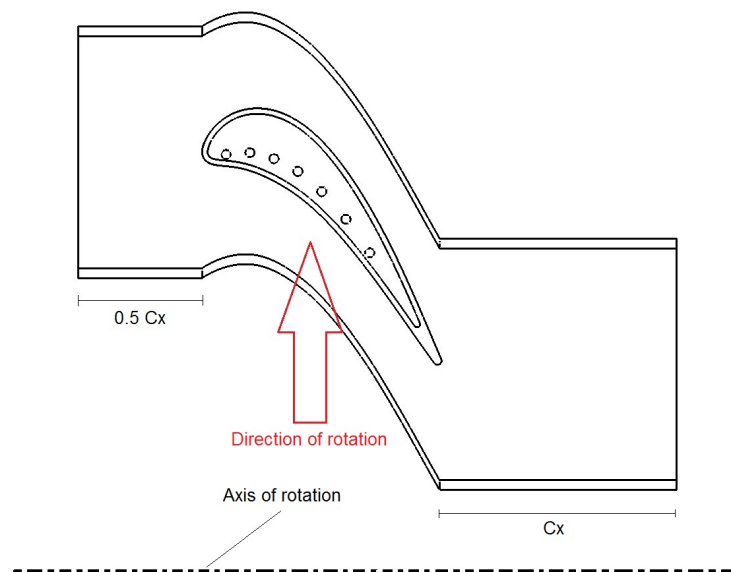
Figure 2.8: CFD domain for configuration study

CHAPTER 3

VALIDATION OF THE NUMERICAL APPROACH

In this chapter, the validation cases performed to build confidence in pressure and heat transfer predictions and in the approach followed during the analyses are presented. The same blade profile at different scales are used in order to make use of the available data in the literature.

3.1 Validation of Pressure Distribution at Blade Midspan

There exists a great amount of experimental data in literature giving details of pressure distribution at various span locations for the cascaded experiments. Since the rotational experiment results are proprietary information to companies, open-to-public engine data is scarce in literature. In the experimental works of Azad et al. [18], [19] and Kwak and Han [13], [22]-, in which the same experimental setup was used, the pressure and heat transfer data are presented. However, the measurement accuracy of the pressure control system used in the experimental setup [18], was questioned by Yang et al. [52].

Vetta et al. [5] conducted experiments in a cascade setup, comprised of the E3 turbine blade, that provides a large data set of flow measurements. The details of the domain for the modeling of the cascade is given in Chapter 2 Section 2.3.1. The findings through CFD analyses are in good agreement as will be shown next.

The boundary conditions for the cascade are given in Table 3.1.

The inlet boundary conditions such as the turbulence intensity and total pressure that were applied at the inlet for the validation study are also used in the configuration

Table 3.1: Boundary conditions for pressure distribution validation [5]

Inlet total pressure, Pt_1	145.91 kPa
Exit pressure, P_2	101.325 kPa
Inlet Reynolds number	683,000
Turbulence intensity level	5%
Turbulence model	k-ω Shear Stress Transport
Inlet static temperature	288 K
Pressure ratio (Pt_1/P_2)	1.44
Exit Mach number	0.68

study. The mass flow rate, $\dot{m}$ through each hole is calculated by the following equation:

$$\dot{m} = \rho_c A_c V_c \tag{3.1}$$

Here, ρ_c and V_c are the density and relative velocity of the coolant flow at the hole exit plane, and A_c is the hole area. This value was selected to give a realistic value for the blowing ratio.

A mesh sensitivity study is done for various number of elements ranging from 0.6M to 6M cells for the cases with no clearance gap. The number of cells is doubled first, from 0.6 millions to 1.3 millions. Figure 3.1 shows that this caused little change in the static pressure coefficient, Cp_s.

Vetta et al. [5] reported their pressure measurements in terms of the static pressure coefficient distribution; hence it is used through this validation study. This term is defined by the following equation:

$$Cp_s = (P - \overline{P_2})/(P_{t1} - \overline{P_2}) \tag{3.2}$$

where P and P_2 are the local static and the area-averaged static pressure at the cascade exit, respectively. The results are almost insensitive to the change in the mesh

36
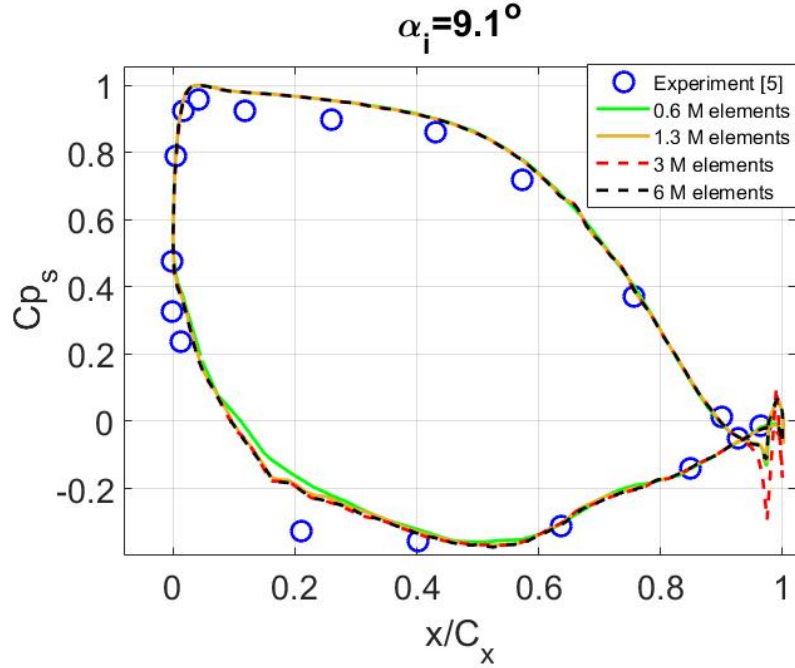
Figure 3.1: Static pressure coefficient variation with mesh size vs experimental data at midspan

number, as the coarse and the fine meshes gave very close results. Hence, no significant changes were expected as the number of the mesh elements in the domain is increased. As a confirmation to this, the performed sensitivity study showed that increasing the number of elements beyond 3M did not make any further changes in the static pressure coefficient distributions.

The experimental data is validated against four different incidence angles, 29.1°, 9.1°, -11.4°, -46.5°. The results can be seen in Figure 3.2. The CFD results are in close agreement with experiments even at high incidence angles. The difference was found to be ranging from 1% to 4%.

A mesh sensitivity study based on the variations at the midspan could be misleading since the midspan flow features are different than the complex flow over the tip region. The insensitivity of the predictions must be established regardless of the coolant flow and the tip shape. For this reason, the squealer tip with seven holes located along the camberline is chosen for the sensitivity study.

For the cooled cases, a blowing ratio of 1.5 is chosen since it is widely used in the
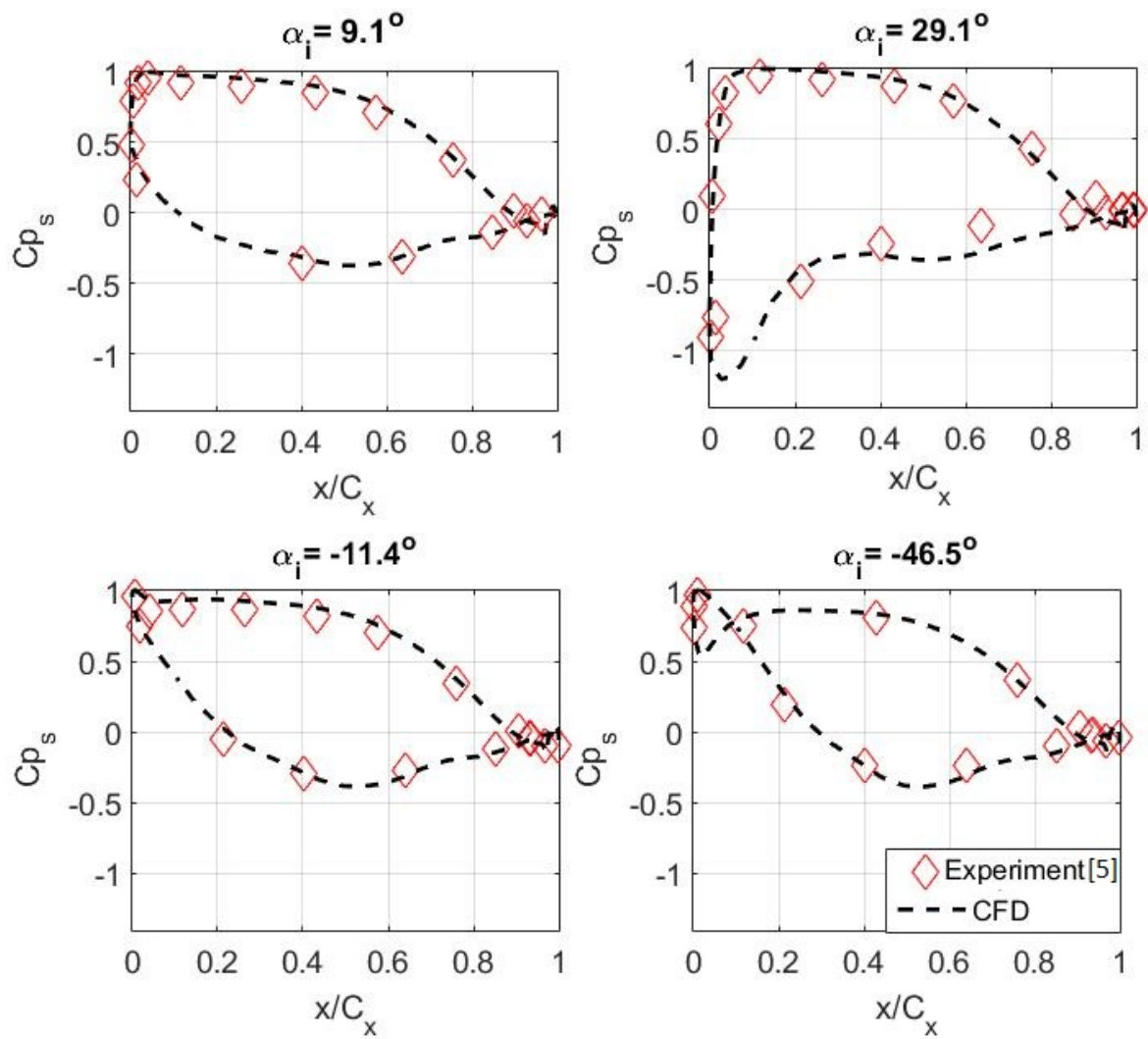
Figure 3.2: Comparison of CFD approach with experimental data

Table 3.2: Number of cell elements used in mesh sensitivity study

Mesh ID	1	2	3	4	5	6	7	8
# of cell elements in millions	2.4	2.9	3.6	4.2	5.2	6	7.3	13

literature [26]. The blowing ratio is the ratio of the multiplication of coolant air velocity and density to the multiplication of the mainstream velocity and mainstream density, as is given by the following equation:

$$BR = \frac{\rho_c V_c}{\rho_{inlet} V_{inlet}} \tag{3.3}$$

The corresponding mass flow rate per each hole is 0.00298 kg/s. The calculation of this value will be explained in Section 4.2 in more detail. The diameter of each hole is 5 mm. The squealer rim height and width are both 3 mm as explained in Section 2.3.1.

Twenty monitor points along the camberline at the mid-gap, in an equally-spaced fashion in the axial direction, were placed to obtain velocities at those points. The flow property that was monitored is velocity, because it reflects the change in the pressure and density as well.

The number of elements used for the mesh sensitivity is given in Table 3.2. In regards to the previous comparison, there are more mesh elements in the clearance gap to provide a higher resolution of the flow in this region of interest. The increase in the number of elements were ensured by only adjusting the affecting parameters of the clearance gap, i.e. the edge length of a cell, the number of elements on the edges of the squealer rim or the blade tip for the flat tip simulations. The remaining domain maintained the same number of elements. The average velocity is calculated by taking the mean of the velocity values obtained from the twenty monitor points. Plot of these average values are given in Figure 3.3.

In addition to the average values, the local values for each monitor point are also examined. The velocities do not differ much with switching to a mesh with higher
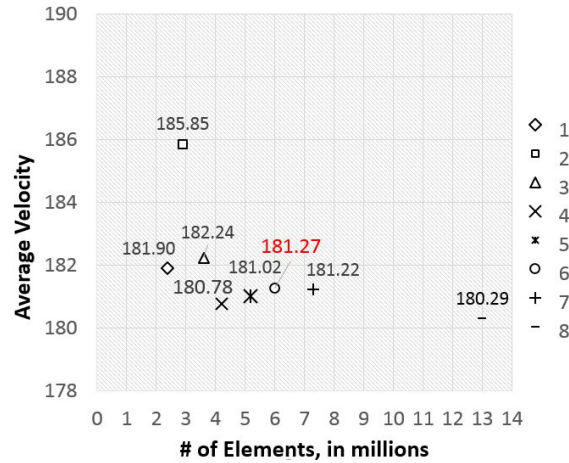
Figure 3.3: Average velocity vs number of mesh elements

number of elements, for the largest three sizes of mesh in the group. The average velocity almost stayed constant for the 7.3M mesh elements that is beyond 6M elements. Therefore, all cases are solved with 6M elements and the corresponding mesh parameters, since the mesh size is an important factor in terms of computational cost. The comparisons shown in Figure 3.2 were from the midspan of the blade. The effect of the leakage flow on the midspan will be negligible. To investigate this behaviour, the same geometry with a 3 mm-clearance gap is analyzed to include both tip types. The blade tips were uncooled in this comparison. The result in Figure 3.4 shows that the blade shape has no effect on the flow features at the midspan, as expected.
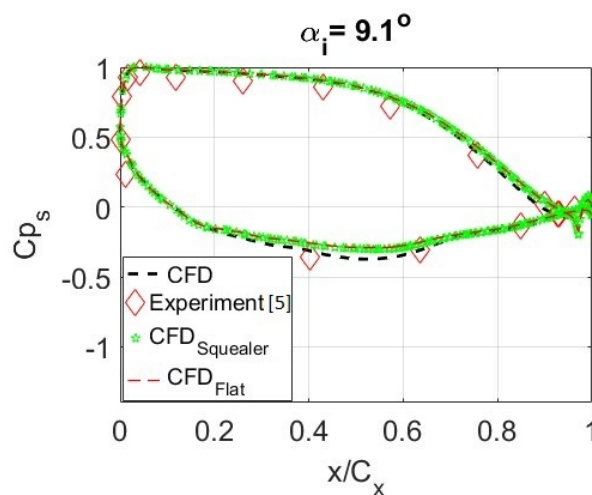
Figure 3.4: Comparison of midspan Cp_s for a blade with and without clearance gap

40

3.2   Validation of Heat Transfer Coefficient at Blade Tip

Since the midspan flow does not reflect the characteristics of the flow leaking over the tip, it was essential to validate the numerical approach against a set of tip data. Kwak and Han [13], [22] collected the average heat transfer coefficient over the E3 blade tip, for both squealer and flat tips, respectively. The blade used was three times larger than that in the actual E3 engine. This data set is used in the thesis as a benchmark to validate the numerical approach. The liquid crystal technique was used in the experiments to measure the convective heat transfer coefficient over the tip. The geometric details of the flow domain are given in Section 2.3.2. The boundary-condition set for the validation is given in Table 3.3. The same experimental environment was used with only the tip shapes of the blade changed.

Table 3.3: Boundary conditions for heat transfer coefficient validation, [22], [13]

Boundary Condition	Value
Inlet total pressure, Pt_1	126.9kpa
Exit static pressure, P_2	102.7kpa
Blade tip temperature	302.15 K, 302.75 K
Casing temperature	302.45K, 302.75 K
Inlet Static temperature	293 K
Inlet Turb. Length Scale	15 mm
Turbulent Intensity	9.7%

Second order accuracy is applied and the k-ω SST turbulence model implemented since it is famous for its accuracy in the calculation of separated flows as is mentioned in Section 2.1.1. Convergence for momentum and mass conservation is ensured by observing the residuals which fell below 10^{-5}.

The blade used for this validation has a different scale, but the mesh parameters used are the same as those used in the sensitivity study in Section 3.1. The same number of elements at the edge of the tip and the maximum cell edge length are used. Hence, the overall mesh size differed. Compared to the flat tip, the number of elements in the squealer tip validation case is higher, since the gap is larger and the volume over the

41

blade tip is also increased due to the fact that a squealer tip is actually a carved version of a flat tip. For the squealer tip geometry, a number of elements ranging between 5M and 15M were used for the mesh sensitivity of this model with the squealer tip. The variation in the area-averaged wall heat flux between the 8M and 15M mesh sizes was only 2%, hence an 8M size mesh was used for validation. A similar mesh size was used for the validation case with the flat tip, since the same blade was used.
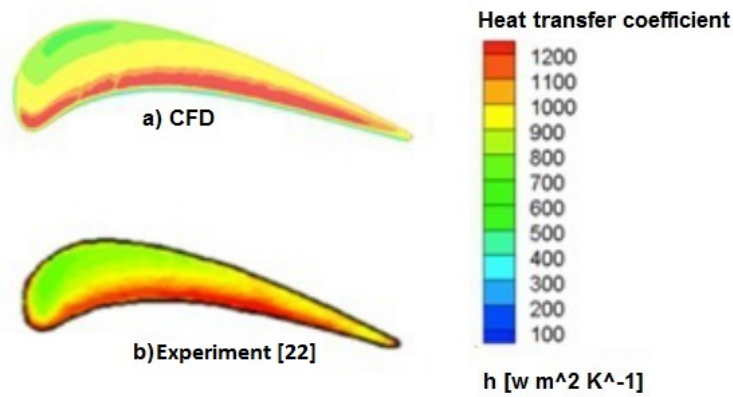

Figure 3.5: Heat transfer coefficient for flat tip, comparison of a) CFD and b) experiment
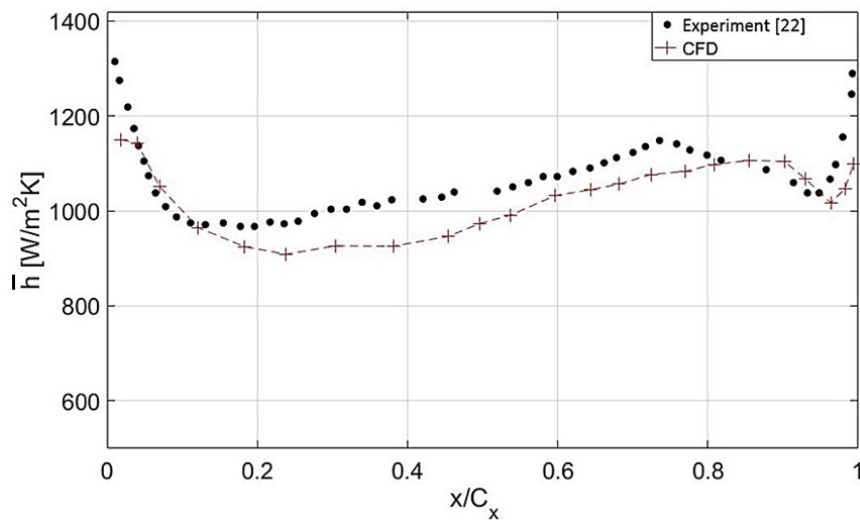

Figure 3.6: Averaged heat transfer coefficient for a flat tip, comparison of CFD and experiment

The heat transfer coefficient distribution over the tip, shown in Figures 3.5, and 3.6 are calculated based on the adiabatic wall temperature. Goldstein [53] proposed that the

use of adiabatic wall temperature is appropriate in the calculation of the heat transfer coefficient, rather than the mainstream temperature, which is used in the calculation of convective heat transfer in practice. Harrison and Bogard [54] also showed that the calculation of heat transfer coefficient is more suitable using adiabatic wall temperature that is the driving temperature for heat transfer, especially in compressible flows. In order to obtain adiabatic wall temperatures, all analyses are repeated to calculate their corresponding adiabatic wall temperatures. After that, the heat transfer coefficient is calculated by the following equation:

$$h_c = q_w/(T_{aw} - T_w) \tag{1.7}$$

where T_{aw} is the adiabatic wall temperature, T_w is the wall temperature, and q_w is the heat flux at the wall. To calculate T_{aw}, the adiabatic wall boundary condition was used, which is the corresponding temperature when the surface is imposed to zero heat flux boundary condition. Since the distribution of the adiabatic temperature over the blade tip surface is not uniform, the temperature information at each cell was required. All temperature boundary conditions were switched to adiabatic wall boundary conditions and the same cases were solved one more time. This procedure was repeated for all heat transfer predictions presented in this thesis.

Heat transfer coefficient based on T_{aw} is given in Figure 3.6 for the flat tip blade, which shows that CFD results are in good agreement with the experimental data. From the mid-chord to the trailing edge, the CFD predictions deviate by 5-8%, which is acceptable since in the experiments, the uncertainty in the heat transfer measurements was high, being approximately ±8%, and reached up to 15% levels in the high heat transfer regions. Still, the high convective heat transfer region near the pressure side is well-predicted. This region is a result of the sharp entrance effect due to the pressure side corner.

The same methodology was followed in predicting the wall heat transfer coefficient distribution over the squealer blade tip. Separate analyses were again solved to obtain the wall temperature distribution from the adiabatic case and the wall heat flux distribution from the temperature boundary condition case. For the squealer tip, the heat transfer coefficient trend is different than that of the flat tip, as observed in Figure 3.7. The heat transfer coefficient reaches its peak value at the leading edge due
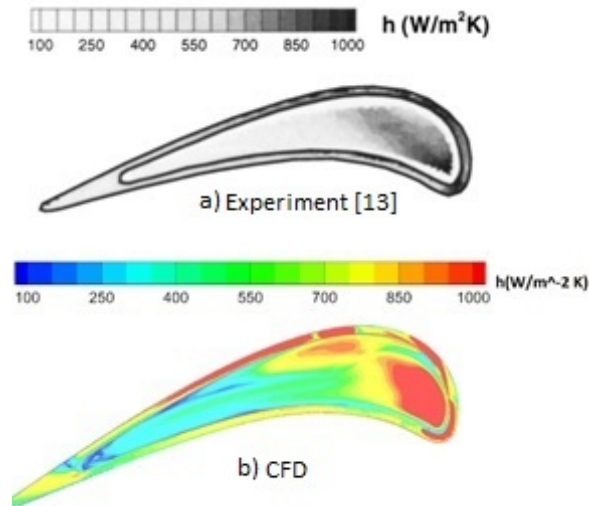
Figure 3.7: Heat transfer coefficient for squealer tip, comparison of a) experiment and b) CFD, 2.5% clearance gap
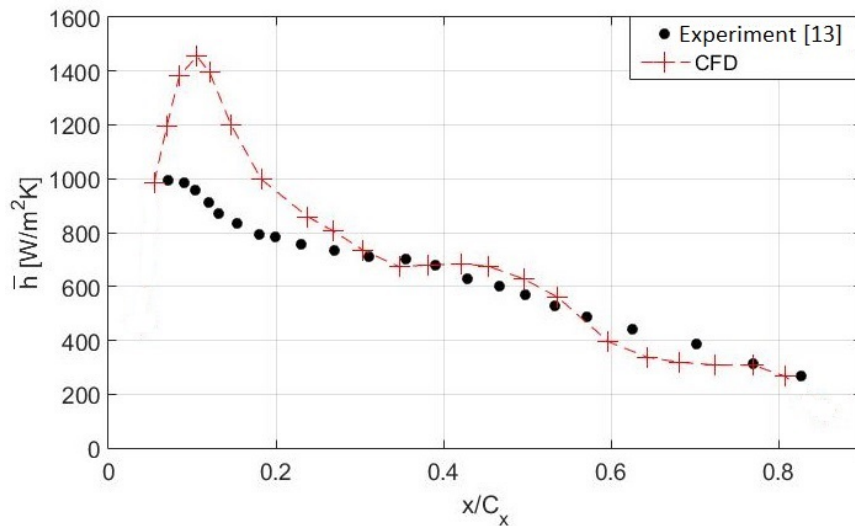
Figure 3.8: Averaged heat transfer coefficient for a squealer tip, comparison of CFD and experiment

to the leakage flow reattachment here. Also, the values over the rim are higher than those over the floor, which were also mentioned before in Chapter 1 Section 1.3. In addition, the heat transfer coefficients are lower near the pressure side compared to the suction side of the blade, as expected.

The local heat transfer coefficient on the cavity floor is also averaged in the chord-

44

wise direction and compared to the data from [13] in Figure 3.8. It was reported in the experiments that the data near the cavity edge could not be obtained due to the shadow of the squealer rim. This was observable from the white stripe surrounding the blade cavity floor edges, on the greyscale contour plot given in Figure 3.8. The axial distribution reflects a continuous drop towards the blade trailing edge as the distribution of Figure 3.7 suggests. The CFD seems to over-predict the data obtained in the leading edge region of the blade. This mismatch is partly due to the mentioned lack of experimental data on the cavity floor since the extent of the shadow is not clearly known, while the predicted heat transfer coefficients were averaged from the pressure side to the suction side across the whole floor instead. On the other hand, as stated before, it was also reported in [13] that the uncertainty for the local heat transfer coefficient was estimated to be ±8% and that it could go up to as much as 15% near the blade tip edge due to the two-dimensional heat conduction effect. Due to the short color change time during the experiments, the uncertainty was also expected to be higher in high heat transfer regions. Considering this, the predictions generally show a good agreement with the data over the majority of the chord length.

CHAPTER 4

BLADE TIP COOLING IN STATIONARY DOMAIN

In this chapter, first, the configurations used in the study are given. Then, the methodology and the boundary conditions will be explained. Finally, the aerodynamic and heat transfer results are presented for the stationary domain. The configurations consist of cooling holes varying in number, location, and size and are implemented on two different tip geometries.

4.1   Preparation of Cooling Configurations

The configuration study uses flat and squealer blade tip geometries. The effect of cooling is examined by introducing cooling hole variations onto the blade tips. After the validation that was introduced in the previous chapter, a tip clearance gap of a typical value found in most of the research in the literature is implemented in the models. A cooling configuration is introduced for both squealer and flat tips. Twelve different configurations with cooling tips were modeled in order to examine the effects of the hole diameter, hole location, number of holes, and the effect of the tip geometry. Additionally, the flat and squealer tips with no cooling configuration were utilized as the baseline configurations to observe the effect of coolant introduction into the blade tip environment. In this part, the domain is stationary, that is, the rotational effects are excluded in the study since the main flow features of aerodynamics are well captured in stationary cascades according to the findings reported in [36] and [37]. The clearance gap, δ, is kept constant for all configurations and it is taken as 2% of span as a typical value. For the squealer tip geometries, δ, is defined as the distance between the rim tip and the casing, so the volume over the squealer tip cavity is larger than

Table 4.1: Details of configurations

Config. ID	Tip Geometry	# Holes	Diameter	Hole Location
Uncooled f	Flat	0	-	-
7c-f	Flat	7	5 mm	Camber line
7ps-f	Flat	7	5 mm	PS
4c-f	Flat	4	5 mm	Camber line
4ps-f	Flat	4	5 mm	PS
Uncooled s	Squealer	0	-	-
7c-s	Squealer	7	5 mm	Camber line
7ps-s	Squealer	7	5 mm	PS
4c-s	Squealer	4	5 mm	Camber line
4ps-s	Squealer	4	5 mm	PS
4c2-s	Squealer	4	5.25 mm	Camber line
4c3-s	Squealer	4	5.5mm	Camber line

those for the flat tips.

The geometrical properties of the flow domain are given in Chapter 2 Section 2.3.1, in Table 2.3 and the hole locations are given in Table 2.4. The boundaries of the domain are depicted in Figure 2.3.

Here, the matrix of the cooling configurations used in the analyses are given in Table 4.1. The abbreviation s stands for the term "squealer" whereas f used for "flat". The camberline is abbreviated as c and it means that the holes are placed along the camberline. ps is an abbreviation for pressure side referring to the holes that are located closer to the pressure side. The hole displacement for ps configurations is 7 mm in the negative pitch direction, i.e. each hole was moved from their corresponding camberline location to the pressure side by 7 mm. $c2$ and $c3$ refer to the configurations with increased hole diameters. These configurations are illustrated in Figure 4.1. Baseline analyses were carried out first where there were no holes on the tips. Then, the effect of number of holes and hole locations are investigated for both squealer and flat tips.
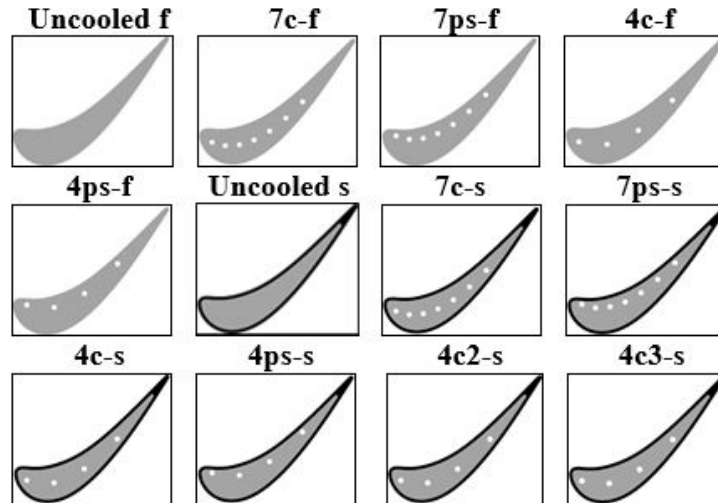
Figure 4.1: Blade tip cooling configurations

4.2 Boundary Conditions

The boundary conditions used in the comparisons are given in Table 4.2.

Table 4.2: Boundary conditions for configuration study

Inlet total pressure, P_{t1}	145.91 kPa
Exit pressure, P_2	101.325 kPa
Inlet Reynolds number	683000
Turbulence intensity level	5%
Inlet static temperature	590 K
Pressure ratio (P_{t1}/P_2)	1.44
Blowing ratio (BR)	1.5 *
Wall temperature, T_w	470K
Coolant mass flow rate	0.00298 kg/s **
Coolant temperature, T_c	330K

* For holes with 5 mm diameter.

** Per each hole.

The Reynolds number is calculated by the inlet air velocity, V_{inlet}, to the domain and

the blade axial chord, C_x is used as the characteristic length, as given in the following equation:

$$Re = \frac{\rho V_{inlet} C_x}{\mu} \qquad (4.1)$$

Here, ρ is the mainstream air density, and μ is the dynamic viscosity. The pressure ratio is a typical value found in the cascade setups.

The inlet temperature, T_i, is 590K, and T_w/T_i is taken as 0.8. For the cases in which the coolant flow is introduced, T_c/T_i is 0.56. These temperature ratios are representative of the actual engine environment.

The definition of the blowing ratio (BR), a parameter that is typically used in any blade cooling study, was given by Eq. (3.3) in Section 3.1.

$$BR = \frac{\rho_c V_c}{\rho_{inlet} V_{inlet}} \qquad (3.3)$$

It is calculated as 1.48 for a mass flow rate of 0.00298 kg/s through each hole. Assuming a fixed amount of cooling air allocation for the subject blade in the design process, the mass flow rate was held constant. This led to a decrease in the magnitude of air velocity through the holes of $4c2$-s and $4c3$-s as the hole diameters were increased. Therefore, BR is 1.48 for all configurations except for $4c2$-s and $4c3$-s, in which the BR values are 1.25 and 1.15, respectively. The determination of this specific mass flow rate was accomplished by several trial-and-error runs.

4.3 Solver Setup and Mesh Sensitivity

Mesh sensitivity study presented in Chapter 3 in Section 3.1 was peformed for the same geometry but with different temperature boundary conditions that were taken from the validation study. The goal was to check the effect of mesh size on the pressure predictions in the clearance gap. The results were presented in Figure 3.3. Since the tip geometry varied between the configurations, one of the most complex tip geometry -the squealer tip with 7 holes along the camberline- was studied to determine

50

the proper mesh size. However, the later stages of the study is concerned with not only aerodynamics but also heat transfer, for which the change in the blade tip flux was also checked for this boundary condition set. The same squealer geometry with the same cooling arrangement as in Section 3.1, is used in this study, but with the boundary conditions defined in Section 4.2. The results presented in Figure 4.2 are plotted only on the cavity floor; the squealer rims are excluded since the predictions on these regions are found to be less sensitive to the change in the mesh size. The appropriate cell size on the cavity floor provides enough resolution for the rims.
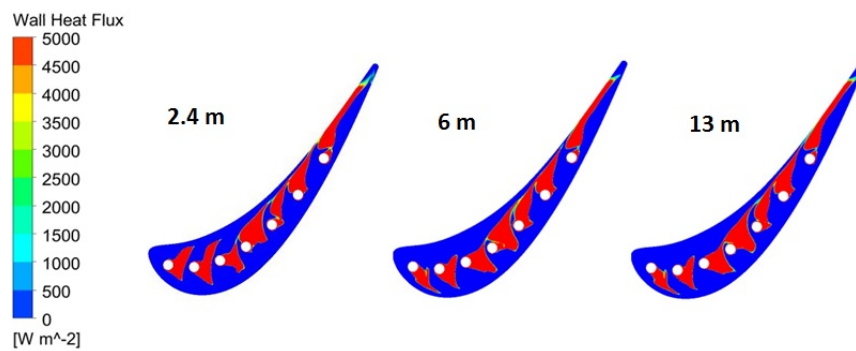
Figure 4.2: Wall heat flux contour plots for mesh sensitivity study on cavity floor, $7c$-s

Since the study also covers the blade tip thermal performance, the solver setup was adjusted accordingly. The $k - \omega$ SST model and discretization with second order accuracy are used as is also mentioned in Chapter 2, Section 2.1.1. The optimum mesh size of 6M was chosen using the differences between these monitor points for different mesh sizes. The maximum error in the wall heat transfer coefficient predictions between 2.4M and 6M elements was 11%. This error decreased to 3.5% between 6M and 13M of elements. The 6M elements were chosen, given that the computational cost increases exponentially when the mesh size increases. The iterations were continued until the convergence criterion of 10^{-5} was reached. $y+$ value was lower than 1 for all cases.

The surface mesh is shown in Figure 4.3. The mesh is denser toward and over the blade tip zone, since the resolution is more critical in that portion of the blade in this study.

51
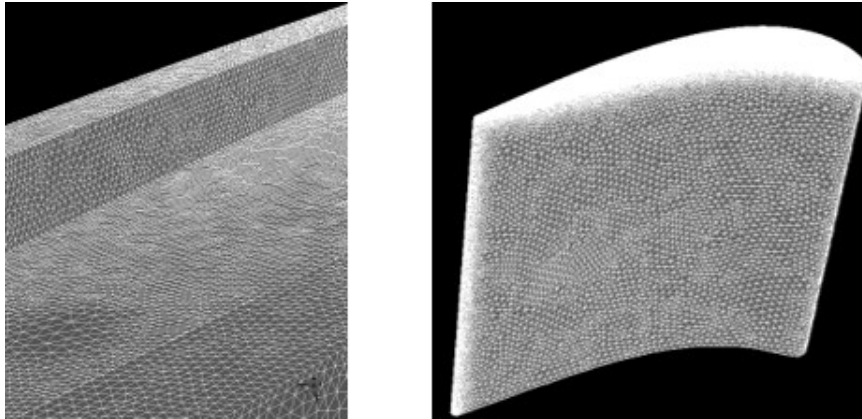
Figure 4.3: Surface cell distribution in configuration study

4.4 Results

In this section, the pressure losses and heat transfer results at the blade tips will be discussed.

4.4.1 Loss Coefficient Calculations

The leakage flow passes through the gap, from the pressure side to the suction side due to the pressure gradient between the surfaces, as confirmed by many studies. This behavior is illustrated in Figure 4.4 where the coolant flow's streamlines are color-coded and shows the velocity variation, indicating flow acceleration towards the suction side of the blade. Black-colored streamlines depict the tip leakage flow, separating from the sharp corner of the squealer rim and rushing into the gap. The detached, leakage flow is mixed out with the coolant flow, rolls up into a vortex structure in the passage. Energy is transferred into the leakage flow, while causing a decrease in the total pressure.

Figure 4.5 compares the tip leakage flow across the tip gap for two different blade tip shapes: squealer and flat tips with coolant injection.

It is apparent that the squealer tip pushes the low-pressure flow to further away from the suction side and delays the formation of the passage vortex. This is the main tip leakage flow behavior when squealer tips are implemented.
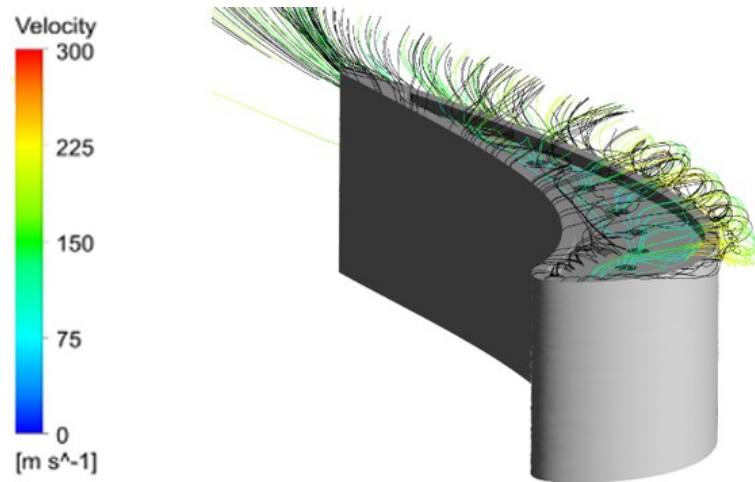
Figure 4.4: Tip leakage flow mixing with coolant flow
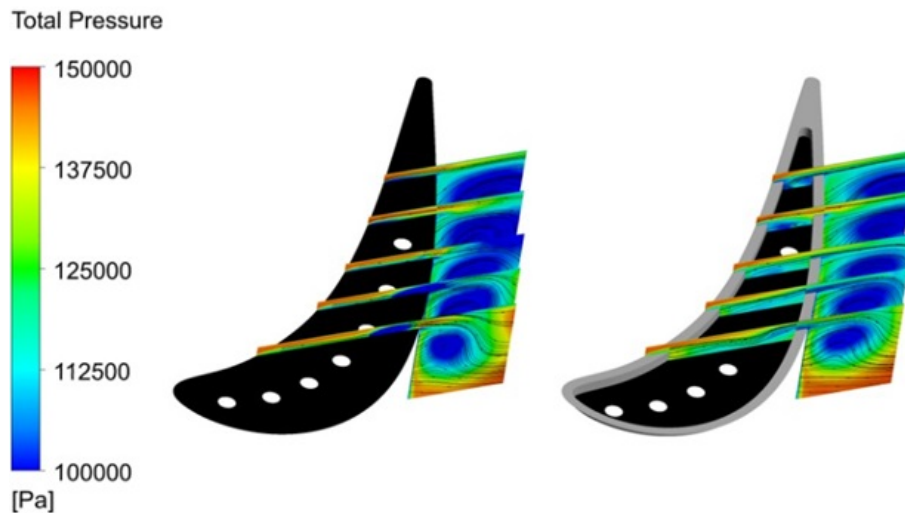
Figure 4.5: Variation in total pressure across gap

Figure 4.6 gives detailed velocity field information for the two tip geometries. Overall pressure loss is thought to be decreasing as a result of a squealer rim usage, according to the contours on the right hand side, since the flow is slowed down due to the squealer rim implemented acting as an obstacle, causing a decrease in the leakage flow velocity. Moreover, towards the trailing edge, further away from the blade surface, the velocity vectors are directed from the pressure side of the neighboring blade that was represented by periodic boundary conditions towards the suction side of the modeled blade, which is an indication of the existing passage vortex.
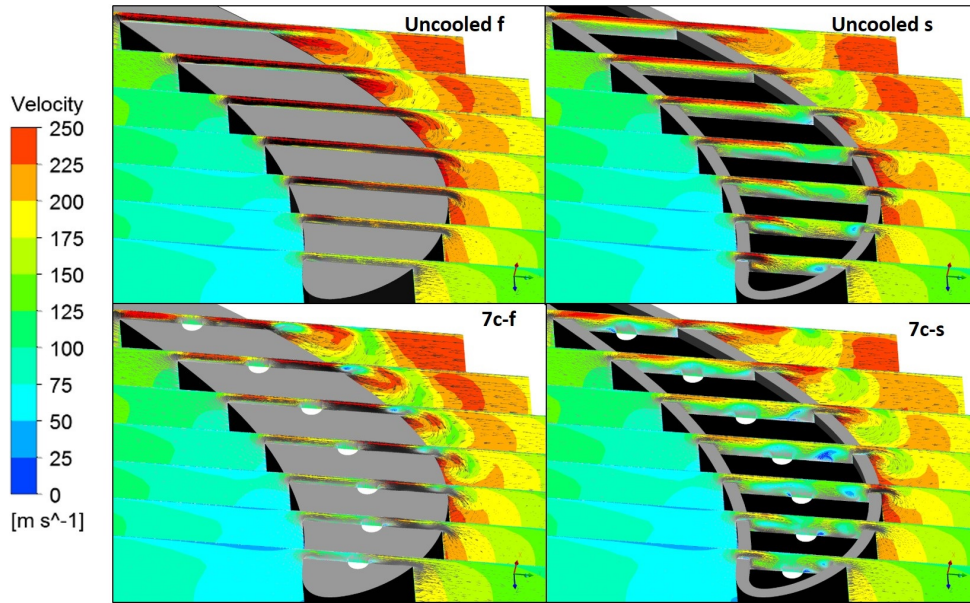
Figure 4.6: Comparison of velocity fields for flat and squealer tips, with and without cooling

The velocity contour plots at the mid gap are depicted in Figure 4.7, the first two rows show the flat tip cooling arrangements while the other two rows show the squealer ones. Configurations $4c2$-s, $4c3$-s are not shown since their distributions are very similar to that of configuration $4c$-s. The reduction in the loss is more for the squealer tip, which has more volume in the gap due to tip recess. For the same amount of mainstream and coolant air, the velocity decreases over the blade tip, as is shown in Figure 4.7 and lower velocity leads to lower losses. This also shows that air sealing is well-accomplished in the squealer tips compared to the flat ones. In addition, the squealer tips with seven holes implemented are superior to their four-holed counterparts, since the total mass flow rate blown off to the gap is more with seven holes, which creates a blocking air-seal with a more efficient manner. Due to this blockage, the leakage flow is slowed down more helping with the decrease in the leakage mass flow rate.
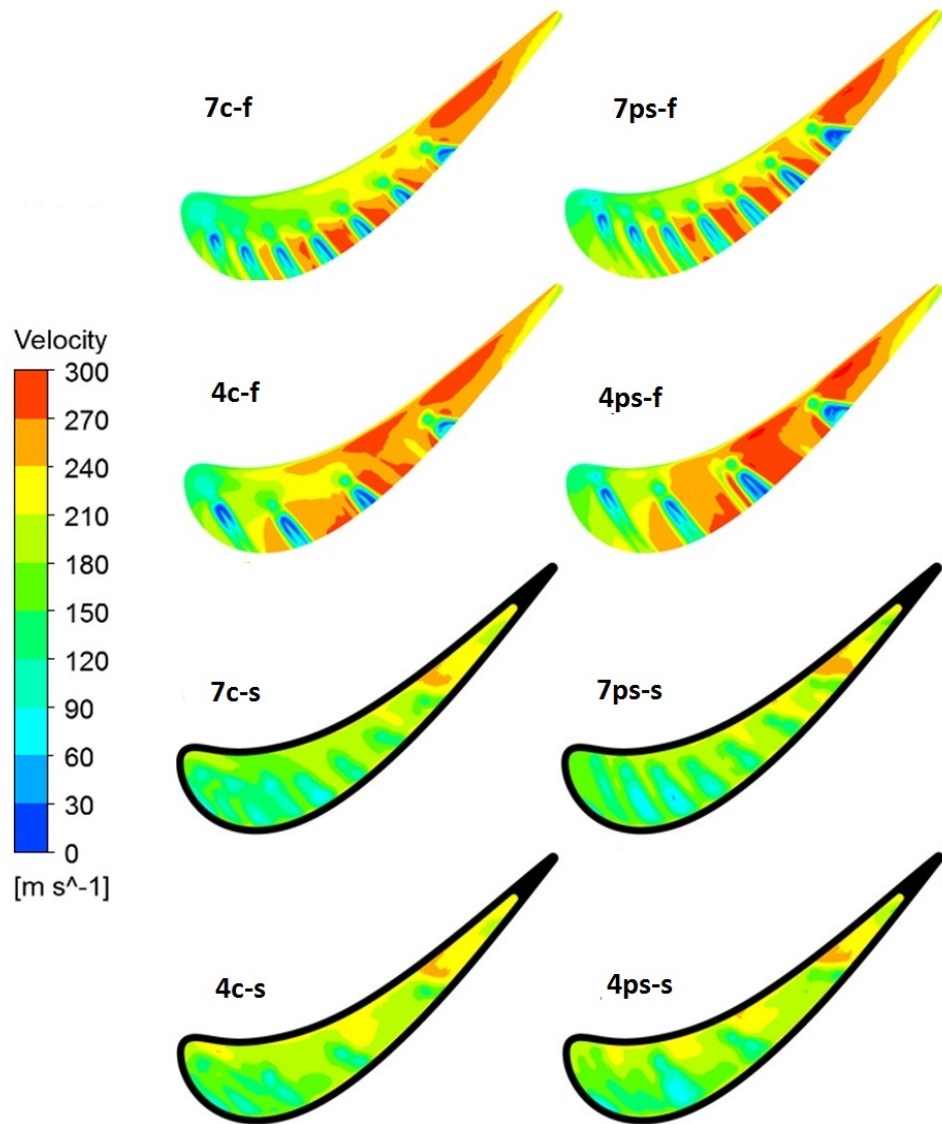
Figure 4.7: Midgap velocity contours

The loss at the tip region can be determined by comparing the local total pressure across the clearance with the total pressure at the domain inlet that was defined in Chapter 1 Section 1.4.1 by Eq. (1.6) as follows:

$$\xi = (P_{t1} - P_t)/P_{t1} \qquad (1.6)$$

The loss at the gap region is calculated by this equation with using local values in the section of interest over the gap zone.

Figure 4.8a given below is plotted for every 25% interval across the clearance gap, starting from the blade tip, as 0%, to the casing wall on the opposite direction, as 100%. The loss coefficient given by Eq. (1.6) is calculated by mass-averaged local total pressure predictions, which are averaged over the planes spanning the clearance gap from the blade tip to the opposite wall, each having an identical shape to the airfoil's cross-sectional area. These planes were separated from each other by 25% increments along the spanwise direction. Explicitly, 0%, 25%, 50%, 75%, 100% are the plane locations at the gap. These steps were repeated for every single configuration in the configuration matrix. The dashed markers with hollow symbols represent the squealer tips in the figure, while the solid markers and symbols are used for flat tips.

Spanning the gap region incrementally from the tip towards the casing, some general trends can be observed for all configurations with slight variations. All configurations with squealer tips appear to have lower loss coefficient than their flat counterparts, on the blade tip and on the opposite wall. The tip loss levels even out at the distance of 25% clearance from the tip, regardless of cooling configuration and/or blade tip geometry used. If one solely looked at the mid gap (50%) clearance, the uncooled flat tip would be considered more advantageous. However, the loss amounts vary across the clearance gap, as shown in Figure 4.8a. The lowest loss levels are observed at 50-75% of the clearance gap. The reason why these specific locations have lower loss amounts might be due to the coolant flow injection into the gap counteracting more efficiently with the leakage flow. Moreover, the squealer configurations reveal more of a gradual decrease starting from 0% to 75%. On the plane located on the shroud, at 100%, the loss levels for all configurations go up significantly. The boundary layer
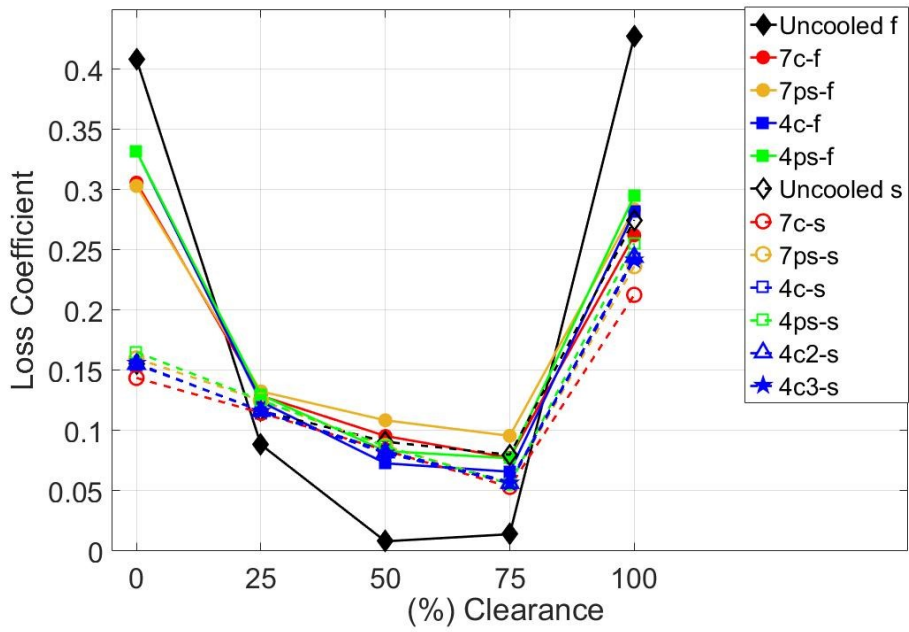
(a) Across clearance gap
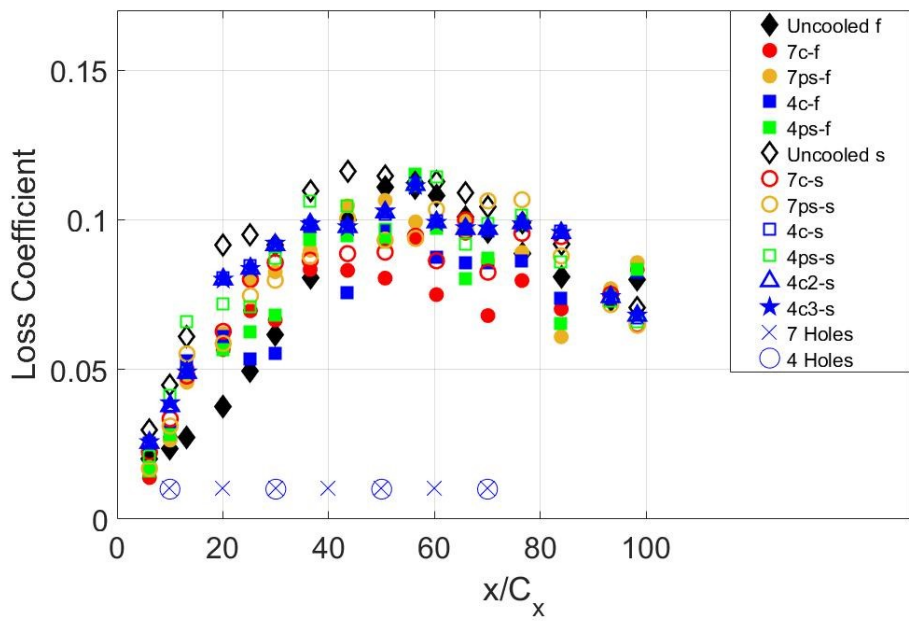
(b) In chordwise direction

Figure 4.8: Loss coefficient variation

developed over the shroud wall might be adding up to the losses here.

Secondly, the loss coefficient variation in the chord-wise direction is given in Figure 4.8b. This time, the local total pressure values at specific chordwise locations on the radial cut-planes in the clearance are mass-averaged to obtain the distribution. Locations of the cooling holes on the tip are shown at the bottom of the plot in grey-colored symbols. For all configurations, the general trend indicates an apparent increase towards the mid-chord region of the blade, which is followed by a mild decrease through the trailing edge of the blade. This behavior is observable for both cooled and uncooled configurations. Each flat counterpart of a squealer tip is observed to cause slightly lower loss on each radial cut. The variation between the comparisons becomes more apparent towards the mid-chord region compared to the regions near the leading edge and the trailing edge. However, these differences are not as large as inspected across the gap in Figure 4.8a.

In order to have a better understanding of the tip leakage flow, the leakage flow behavior downstream of the blade trailing edge can be examined. The total pressure loss distribution on a radial plane at $0.7C_x$ downstream of the blade trailing edge is demonstrated in Figure 4.9, across a single passage. The right and left sides are the pressure and suction surfaces of the blades, respectively. For comparison purposes, the distributions are shown in terms of the total pressure coefficient, ψ, to represent the total pressure loss as was done by Volino [26] which is given by the following equation:

$$\psi = (P_{t1} - \overline{P_t})/(\rho_i U_i^2/2) \qquad (4.2)$$

where $\overline{P_t}$ is an area-averaged value at the specific examined location downstream of the blade trailing edge as shown in the figure.

Though the boundary conditions used in Volino's study [26] were not close to those in this thesis, the flow structure exhibits the same features. The experiment in Figure 4.9 was performed using the same E3 airfoil profile, but the aspect ratio of the cascade was kept much higher and the Reynolds numbers in which the measurements were performed at (Re=60,000) were much lower than in the current study.
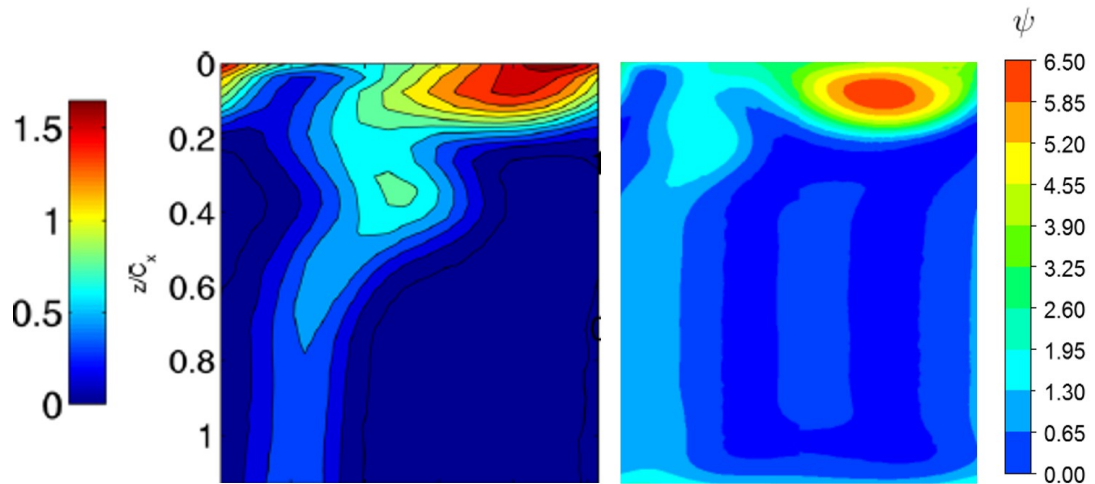
Figure 4.9: Tip leakage flow comparison, left data from Fig. 21-a [26], right CFD

Moreover, the radial cut plane was at $0.7C_x$ downstream of the trailing edge in Volino's study. On the other hand, the predictions of the current study are generated on a radial plane at $0.5C_x$ downstream of the trailing edge. The comparison is performed for the uncooled flat blade tip. The computational domain did not extend beyond $0.65C_x$ downstream (in the axial direction), however, the flow structure was observed to stay the same beyond $0.5C_x$ location. Though there are differences between the two cases, especially in magnitudes, the predictions show remarkable similarities in terms of main flow features. Here, the red spot observed is the leakage vortex, and the one right below is the passage vortex.

In Figure 4.10, the circumferential mass averages of exit flow angle and the loss coefficient, ξ, given by Eq. (1.6), along the whole span are represented for the plane located at $0.5C_x$, downstream of the trailing edge. As seen in these figures, the leakage vortex has a strong influence on the flow pattern. Moreover, the flow angle and the loss coefficient are observed to be inversely proportional, the loss coefficient amount increases towards the tip and in the near-tip region as the flow deviates from the blade's exit angle.
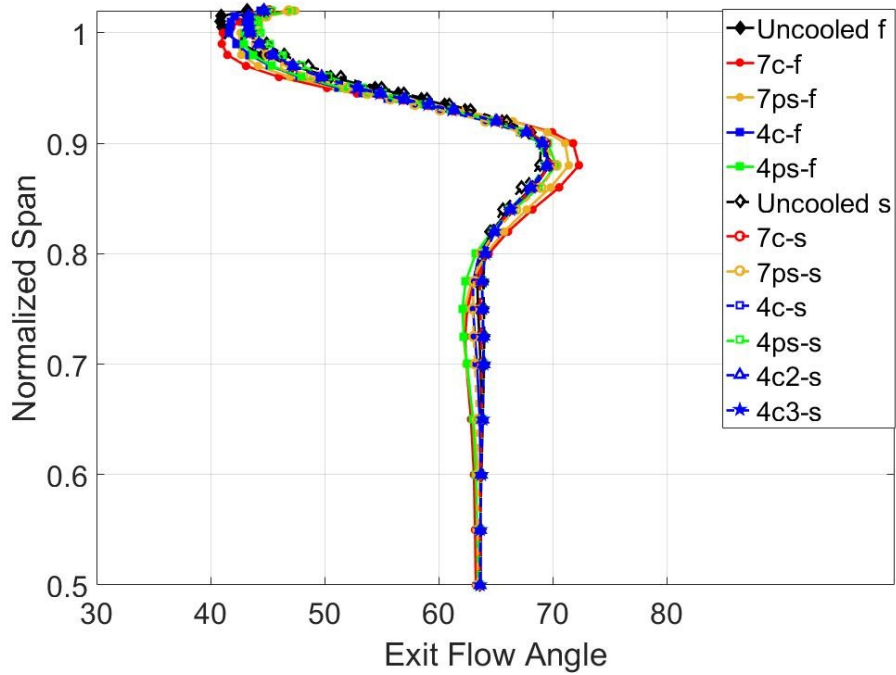
(a) Exit flow angle
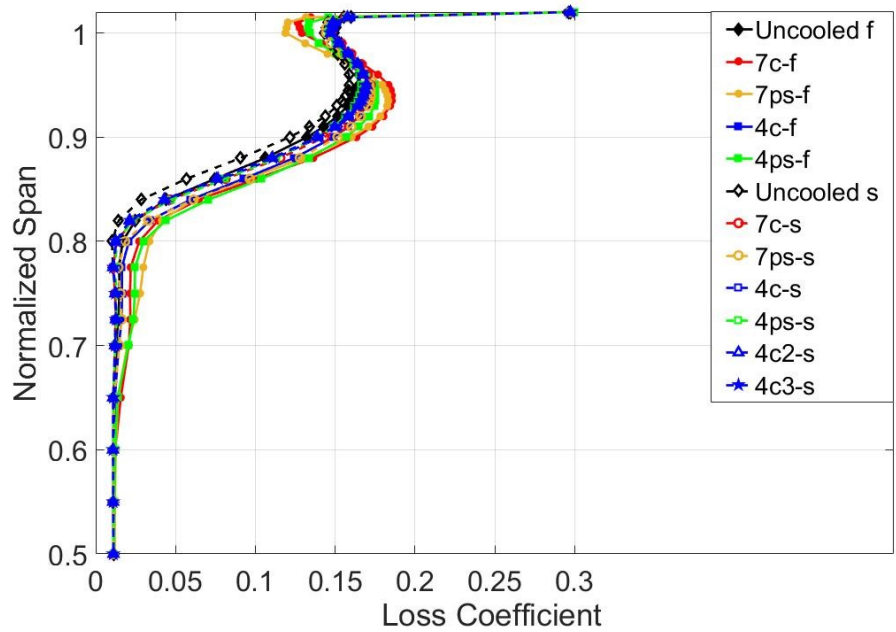
(b) Loss coefficient

Figure 4.10: Circumferential averages in the pitchwise direction at $0.5C_x$ downstream of the blade TE
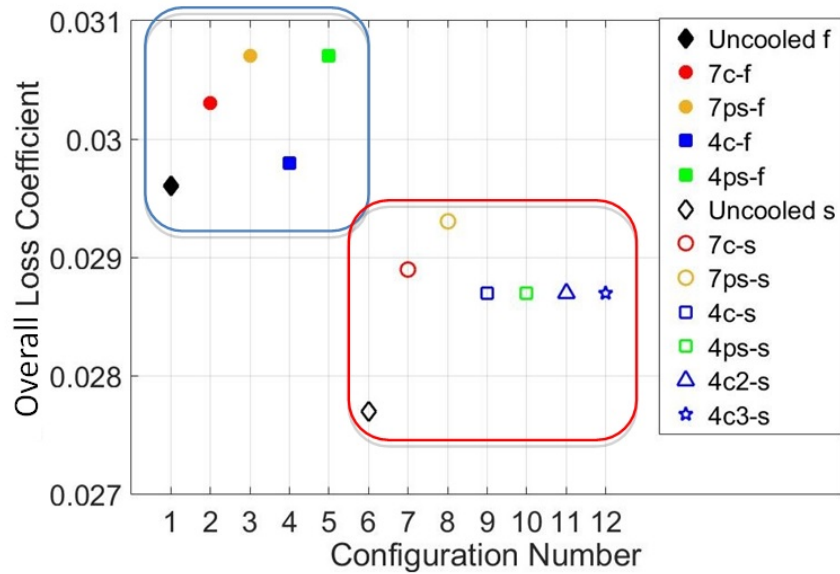
Figure 4.11: Overall loss coefficient comparison

The local total pressure was mass-averaged over the plane located at $0.5C_x$ downstream of the trailing edge to calculate the overall loss levels throughout the cascade for each configuration. Figure 4.11 summarizes the loss behavior through a cascade passage as the tip geometry and cooling configurations are varied. It is seen that the data points are gathered in two groups: the data falling into the red enclosure belongs to the configurations with squealer tips, whereas the data points in the blue enclosure are flat tip configurations. It is obvious that the flat tip configurations produce more loss compared to squealer ones. The effect of increase in the hole diameters was only examined in configurations with squealer tips, and this effect on the aerodynamic loss is negligible. Also, another remarkable finding is that the holes placed close to the pressure side lead to a higher amount of tip leakage loss with an exception for the squealer tip with four holes. For this configuration, the resultant loss is not observable. The baseline uncooled configurations are found to be more efficient than their corresponding cooled configurations. It is because of the momentum addition through the coolant injection adding up to the losses generated across the tip gap. Therefore, the squealer tips with four holes are more efficient than their seven-holed counterparts.

61

4.4.2 Heat Transfer Results

The wall heat transfer coefficient is calculated as explained in Chapter 3, Section 3.2 by Eq. (1.7):

$$h_c = q_w / (T_{aw} - T_w) \tag{1.7}$$

q_w is calculated by the CFD run with the wall boundary condition where a wall temperature, T_w is applied. The adiabatic wall temperature, T_{aw}, is calculated through a separate analysis in which the adiabatic wall boundary condition is applied to the walls in the domain.

In Figure 4.12, the surface streamlines with the heat transfer coefficient, h_c, on the blade tip for each configuration are demonstrated. Blue-colored traces depict the lowest heat transfer coefficients, which are caused by the addition of coolant. Along the blade's pressure side, the highest h_c levels are observable towards the leading edge portion for the flat tip configurations. For the configurations with the squealer rim, the leading edge of the cavity floor exhibits higher heat transfer coefficient across a wide zone as well as on the suction side portion of the squealer rim. These regions are the corresponding lowest momentum portions from the velocity distribution contour plots of Figure 4.7. The flow streamlines are denser and squeezed towards the pressure side in the configurations with flat tips where the holes are located along the camberline. This is due to the flow reattachment occuring in this region, which is the sharp entrance effect. When the holes are moved towards the pressure side near this split region, the dense streamline trend is washed out of the zone.

Figure 4.12 compares the heat transfer coefficient for configurations with the coolant effect. The comparison for the baseline uncooled versions is given in Figure 4.13. These findings are generally in good agreement with the trends in the study of Kwak and Han [13], [22], which were done by using the same blade profile, but the experiments were conducted at much lower temperatures. It is clear that the variation of the heat transfer is undeniably large across the tip region. The gradients are also more significant on the squealer tip. The implementation of the cooling holes further increases this variation. For the flat tip, the heat transfer coefficients along the pressure

side are higher than those along the suction side. On the other hand, for the squealer tip, the lowest heat transfer coefficients are observed on the cavity floor, towards the trailing edge of the blade. Also, it is found that the formation of the low heat-transfer zone by the leading edge, namely the "sweet spot" is not observable in our predictions whereas it was observed in [13]. This difference is thought to be because of the difference in the boundary conditions, since the configurations in this thesis reflect the actual engine environment.

Next, the calculations will be performed in terms of the Nusselt number, which is calculated by the following equation:

$$Nu = \frac{h_c C_x}{k_f} \tag{4.3}$$

where C_x is the axial chord of the blade, and k_f is the thermal conductivity of air with a value of 0.04148 $W/m.K$. This value corresponds to the film temperature, 530 K, which is the average of the free stream and wall temperatures as defined in [55]. The corresponding area-averaged Nusselt number values are provided in Table 4.3 for both the squealer rims and the cavity floors. The Nusselt trends demonstrate similar trends with those of the averaged heat-transfer coefficients over the surfaces, but with different values since the heat transfer coefficients in Figures 4.12 and 4.13 are shifted when converted into the Nusselt number. Therefore, additional contour plots for Nusselt number distributions will not be provided.

From Table 4.3, it can be deduced that adding the squealer rim to the tip results in a remarkable decrease in the averaged Nusselt number over the tip floor, compared to the flat counterpart. Since the rim restrains the air inside the cavity, the air velocity decreases. The most effective cooling option is observed to be the one with the squealer tip and seven holes located near the pressure side. The configurations with 4 holes are not as efficient as their seven-holed counterparts in removing the excessive heat over the tip. The difference caused by the number of holes becomes more significant in squealer tips. The last two rows of the Table 4.3 shows the cases with increased diameters. It can be deduced that they are more effective in reducing the Nusselt number. Since the coolant mass flow rate is held constant for these cases with the larger holes, the velocity of the coolant air introduced into the gap decreased
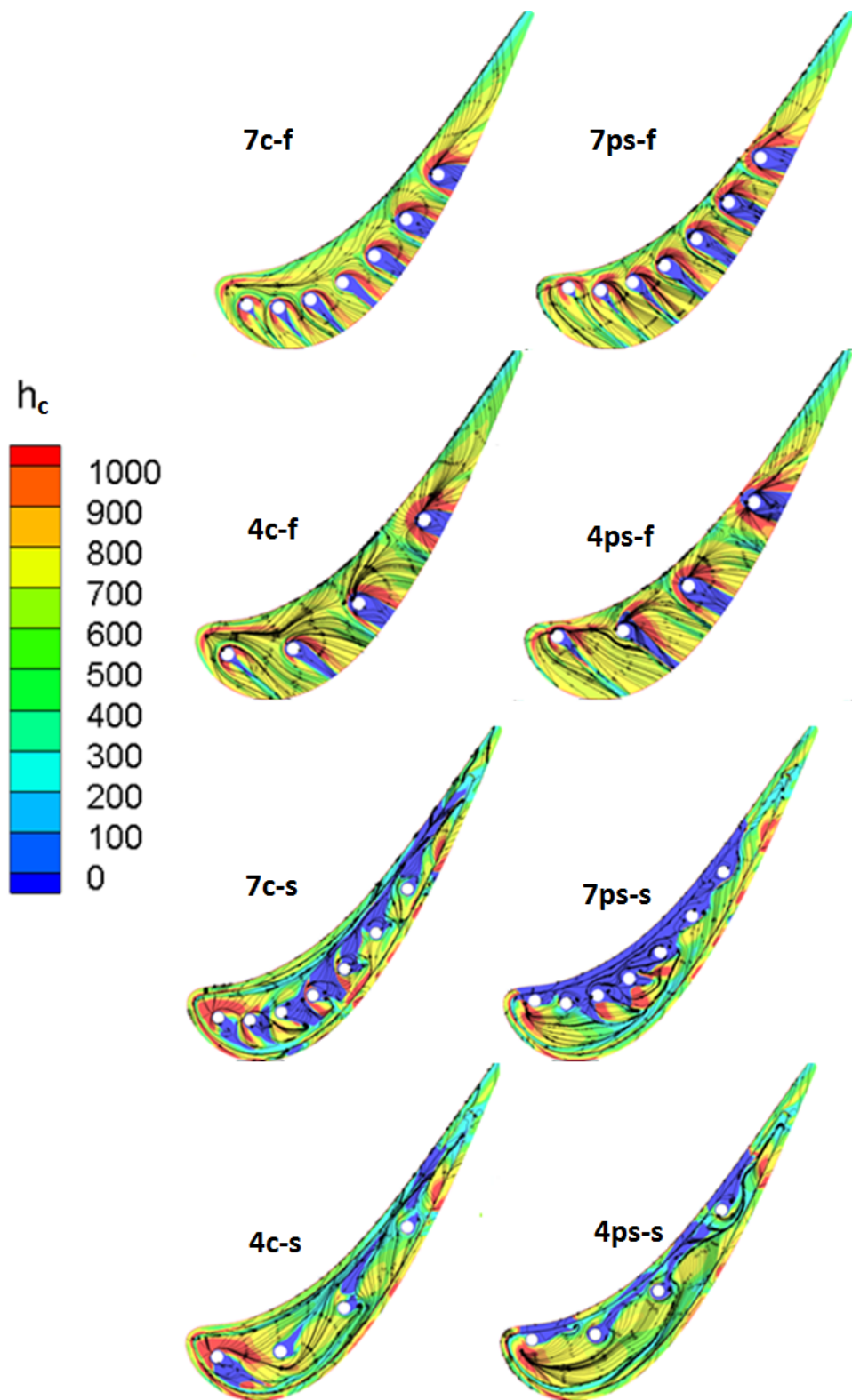
Figure 4.12: Blade tip heat transfer coefficient comparison
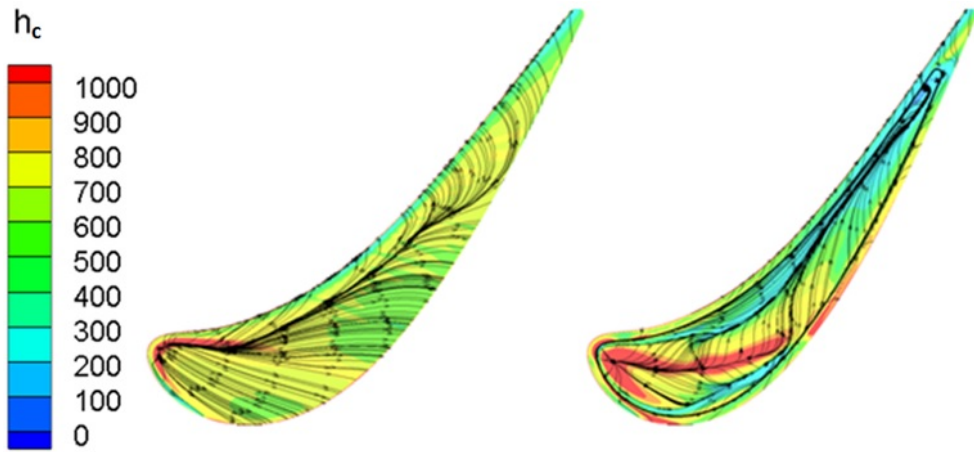
Figure 4.13: Comparison of blade tip heat transfer coefficient for uncooled configurations

Table 4.3: Area-averaged Nusselt numbers for configurations

CONFIG. ID	Nu # Tip floor	Nu # Squealer Rim
Uncooled f	2140.7	-
7c-f	1991.4	-
7ps-f	2179.4	-
4c-f	2154.6	-
4ps-f	2217.5	-
Uncooled s	1929.9	2401.4
7c-s	1137.6	2663.9
7ps-s	628.5	3349.5
4c-s	1728.3	2509.4
4c-s	1728.3	2509.4
4ps-s	1720.3	2780.1
4c2-s	1679.9	2536.4
4c3-s	1631.7	2547.3
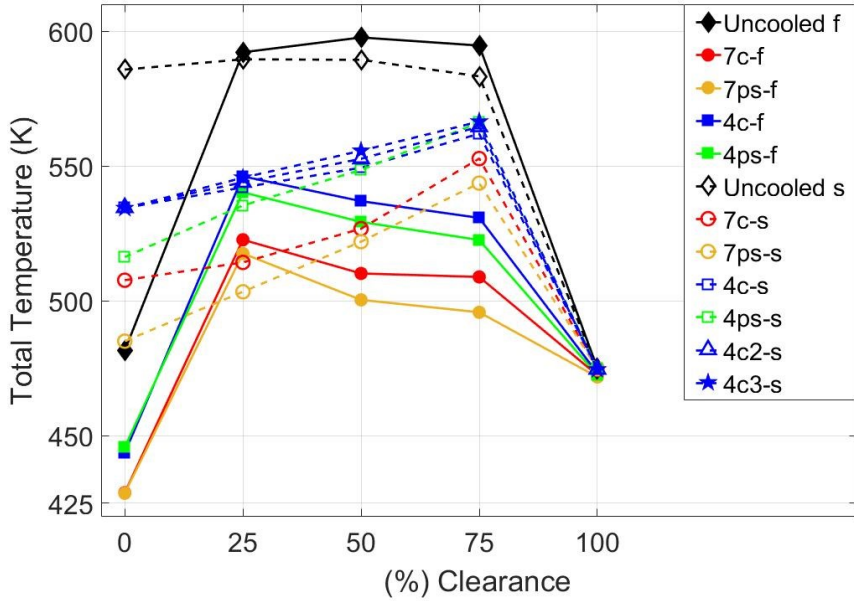
Figure 4.14: Variation in total temperature across the gap

resulting in a decrease in the Nusselt number.

Figure 4.14 shows the mass-averaged total temperature across the clearance gap to examine the flow behavior. The dashed symbols are used for the squealer tips whereas the solid ones represent the flat tips. The total temperature varies across the clearance gap from the tip surface to the shroud, which results in differing bulk temperatures. The same boundary conditions were applied to all walls in computations, which were set at 470 K. However, although the average temperature is the same at the casing, it is differing at 0% on the tip surface for all configurations. This is because this location corresponds to the blade tip surface for the flat tips, while it corresponds to the rim tip surface for the squealer tips. Hence, there is an additional volume between 0% location and the cavity floor and those regions are not captured in this figure.

The averaged total temperature is the highest for the uncooled cases compared to their cooled counterparts at all clearance gaps as expected. Both flat and squealer tips demonstrate lower levels of temperature across the gap with the holes close to the pressure side. In addition, the effect of an increase in the diameter of the holes on the total temperature is negligible. This trend is consistent with what has been observed in the previous figures. The configuration with seven holes located toward the pressure

66

side has the lowest temperature across the gap, among the squealer configurations examined. The highest temperature levels attained for all squealer tips are observed at the distance corresponding to 75% of the clearance gap, radially away from the blade tip. It is also the location where the lowest tip loss amounts are observed, according to Figure 4.8a. That is to say, for the squealer tips, the local total pressure increases gradually which is also followed by a gradual increase in the local total temperature, up to this point. For the flat tips, this trend seems to differ.

The total temperature distributions at the mid-gap region for all configurations are shown in Figure 4.15. Obviously, the cooling effect of the coolant air blown into the gap is still valid at this distance away from the holes for all configurations. The mass-averaged values of these temperatures are what is given at 50% clearance gap of Figure 4.14. The five mass-averaged values presented in Figure 4.14, across the clearance gap are averaged once more to obtain a representative bulk temperature inside the gap, as shown in Figure 4.16.

Figure 4.16 indicates that, depending on the configuration used, the total temperature in the gap can be decreased as much as 60 °C. The configuration with the lowest bulk temperature inside the gap is calculated to be the one with seven holes that are placed near the pressure side. This holds for both flat and squealer tip configurations. The bulk temperatures for the squealer configurations would be further reduced if the additional volume inside the cavities were taken into account.
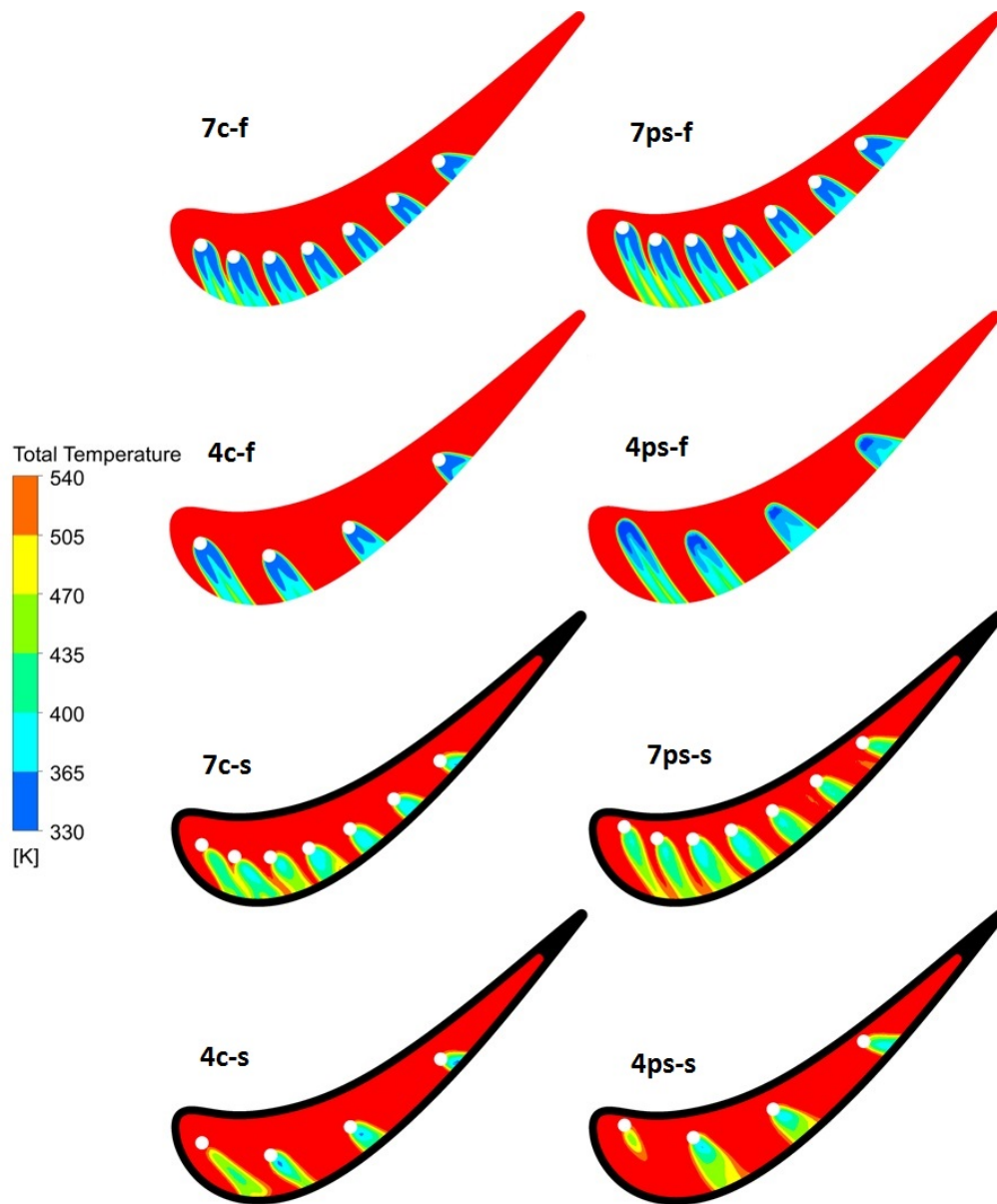
Figure 4.15: Total temperature distribution at mid gap
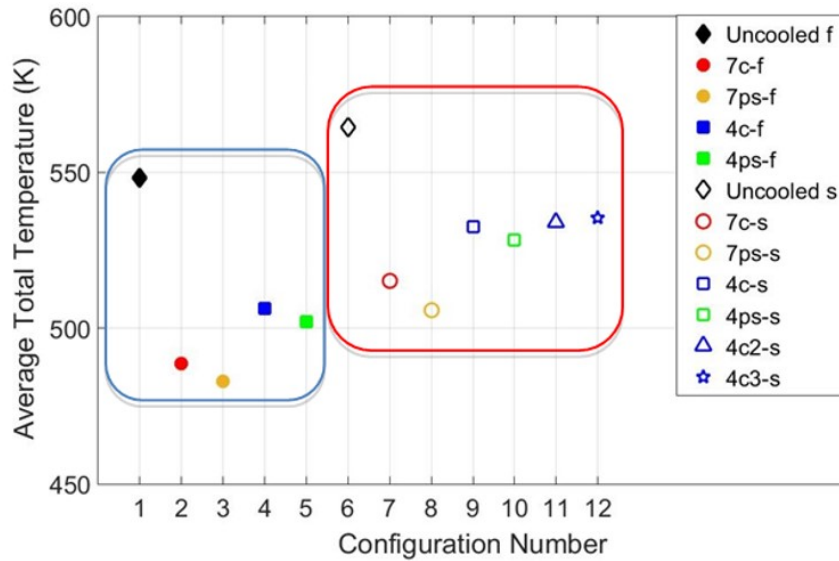
Figure 4.16: Mass-averaged total temperature across the gap per configuration

4.4.3 Summary of Findings

The correlation between the thermal performance and the aerodynamic loss can be interpreted in a summary plot that will guide one to select the optimum cooling configuration. It should be noticed that these findings are relevant to the configurations studied and the boundary conditions applied in this thesis. The overall loss coefficient versus Nusselt number is plotted for each configuration and those values are normalized with a base value to make a one-to-one comparison. The base value is defined as the average value of the predictions from the uncooled configurations.

The variations are presented in Figure 4.17 for all configurations. Generally, the squealer tips are superior to flat tips in terms of both aerodynamic and heat transfer. For the flat tip configurations, placing the holes near the pressure side is observed to be increasing the tip losses, but this does not cause a significant change in its thermal performance. Among the configurations examined, the squealer tip with seven holes near the pressure side arrangement yields the best thermal performance while causing a slightly higher level of loss compared to its seven-hole counterpart with the holes placed along the camberline.
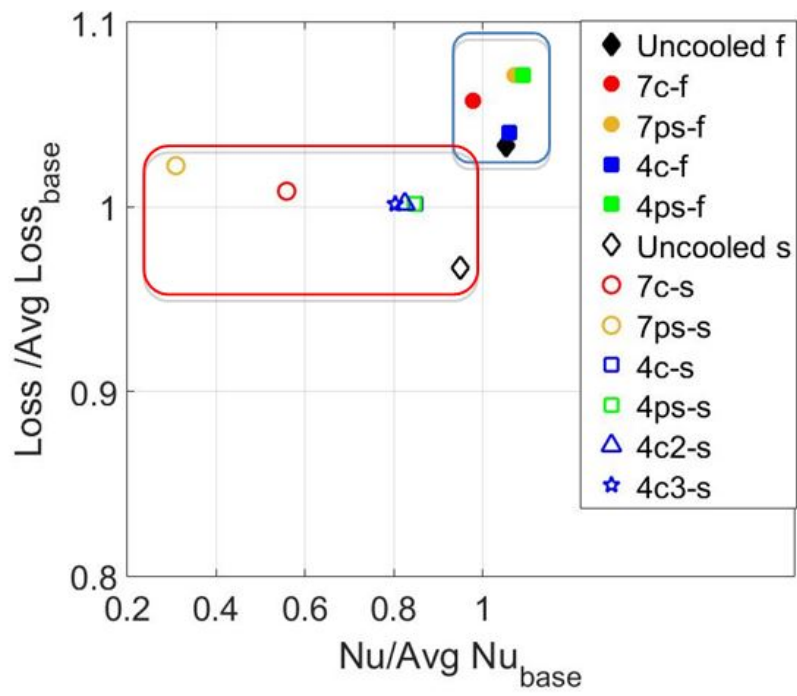
Figure 4.17: Overall loss vs heat transfer

CHAPTER 5

BLADE TIP COOLING IN ROTATING DOMAIN

In this chapter, the thermal performance of a squealer tip geometry is investigated by varying the depth of its cavity. The cooling configuration is not varied in the comparisons. The engine operating environment is modeled using a rotational domain together with representative temperature and pressure conditions. In the following sections, first, the configurations used in the study are presented. Then, the methodology and the boundary conditions will be explained. Finally, the heat transfer results are discussed.

5.1 Preparation of Tip Configurations

This time, the configuration study is comprised of a squealer tip blade only, since the squealer tip has proven its superior performance in the previous chapter. In this chapter, the squealer rim depth-to-width ratio and the rotation effects are taken into account. The geometry is taken directly from the report by Timko [4], as was explained in Section 2.3.3 and is designed accordingly. The clearance gap, δ, is again kept constant for all configurations, and is designed as 1% of the blade span. This is the gap between the shroud (casing) and the top of the squealer rim, and not the tip cavity floor. Therefore, an additional cavity volume is present below the tips of the squealer rims.

The intent is to examine the effect of the depth-to-width ratio of the rim on the heat transfer characteristics of the rotating blade. This ratio, denoted as d/w, varies among the values of 1, 1.5 and 2. This variation is obtained by keeping the width constant while the depth of the squealer rim is varied. The configurations of the blade tips are

depicted in Figure 5.1.
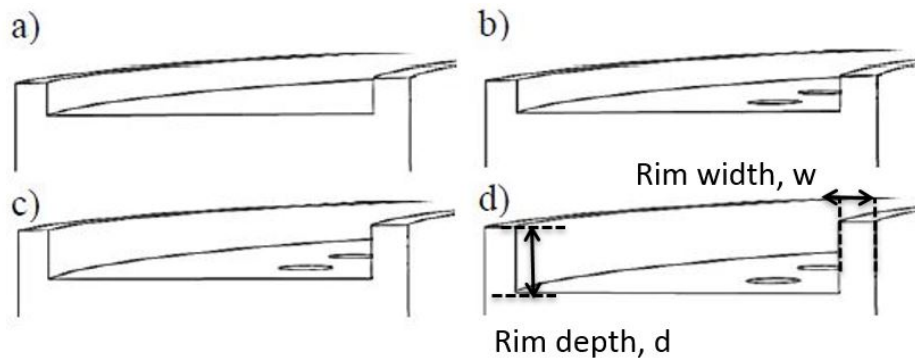
Figure 5.1: Configurations, a) uncooled, d/w=1, b) cooled d/w=1, c) cooled d/w=1.5, d) cooled d/w=2

Blade profile is the same one that has been so far. The differences are explained in Section 2.3.3. The squealer tip configurations were implemented in the E3 first-stage high-pressure turbine (HPT) blade. This rotor consists of 76 blades. Next, the calculation of the blowing ratio is explained.

5.2   Boundary Conditions

The boundary conditions used in the configuration study are summarized in Table 5.1. The conditions are categorized as stationary or rotational. They are all the same except for the applied pressure ratio through the passage, since the rotational domain allows for a higher pressure drop, inherently. The pressure ratio is taken as the total-to-static pressure ratio and it is 5.57 for rotational configurations whereas it is 1.5 in the absence of rotation. With these boundary conditions, a shock was observed right at the leading edge of the blade in the stationary cases. However, the findings from the stationary domain are still included in this discussion and gives insight to the differences arising from the blade rotation. The flow periodicity is ensured by modeling a blade passage and by applying periodic boundary conditions to the boundaries across the pitch direction.

For the rotational analyses, the configurations used in the study consist of an uncooled

Table 5.1: Boundary conditions for configuration study

Boundary Condition	Rotating Domain	Stationary Domain
Inlet total pressure, P_{t1}	344.74 kPa	344.74 kPa
Exit pressure, P_2	61.84 kPa	229.83 kPa
Turbulence intensity level	5%	5%
Inlet total temperature	683 K	683 K
Wall temperature, T_w	470 K	470 K
Coolant Temperature, T_c	330 K	330 K
Mass flow rate per cooling hole	0.00014 kg/s	0.00014 kg/s
RPM	8450	0

blade tip with $d/w = 1$ and cooled tips with $d/w = 1$, $d/w = 1.5$, and $d/w = 2$. The Mach number at the inlet of the domain is higher in the cases involving rotation due to the higher pressure ratio. As the energy is extracted from the flow through the rotating blade row, the Mach number decreases in the absolute frame, resulting in a Mach number of 1.02 at the blade leading edge and 0.86 at the blade trailing edge, while flow acceleration is observed in the relative frame as expected, increasing the Mach number from 0.44 to 1.34 at the blade trailing edge. These values are mass-averaged values in the radial direction.

Reynolds number is calculated using Eq. (4.1) as defined in the previous chapter, Section 4.2:

$$Re = \frac{\rho V_{inlet} C_x}{\mu} \tag{4.1}$$

The axial chord is used as the characteristic length in the calculation of the Reynolds number. This value is 844000 for the rotational cases and 749000 for the stationary ones. Also, the mass flow rate of 0.00014 kg/s corresponds to a blowing ratio of 0.68 and 0.30 in the rotating and stationary cases, respectively. The main flow parameters used in the definition of the blowing ratio are taken at the inlet of the domain, and the velocities are defined to be relative to the blade.

5.3 Solver Setup and Mesh Sensitivity

In the selection of a suitable mesh size, the computational time and the sensitivity of a parameter to the mesh size were taken into account. The increase in mesh size was managed by increasing the mesh density over the tip region and by decreasing the surface cell size on the rim and on the cavity bottom. The volume elements in the gap adjusted themselves, accordingly. The mesh parameters such as the cell edge length, minimum cell volume, number of prism layers on the walls are kept the same.

Table 5.2: Mesh sizes used in mesh sensitivity study

# Elements (in millions)	Area-averaged wall heat flux (W/m^2) on the cavity	% deviation from the largest mesh
2.4	-101424	10.878
3.1	-105903	6.943
4.3	-109314	3.945
5.7	-110125	3.233
6.2	-109971	3.368
7.1	-111073	2.399
8	-110801	2.639
11	-113095	0.623
13	-113804	0.000

For the mesh sensitivity analysis, different mesh sizes ranging from 2.4 M to 13 M elements were considered. The analyses were carried out for the tip geometry having a depth-to-width ratio of 1 and under rotation. The change in the area-averaged wall heat flux on the blade tip was monitored as the mesh size was increased. The corresponding values are given for each mesh size in Table 5.2. The variation in the averaged wall heat flux between 2.4 M and 5.7 M elements was 8.6%. This variation decreased to 3.2% between 5.7 M and 13M. Considering that the required computational power grows exponentially with the mesh size, the mesh comprising of 5.7 M elements was used in the study. The convergence was established in the levels of 10^{-5}. $y+$ values were lower than 1. The surface mesh used in the computations is

illustrated in Figure 5.2.
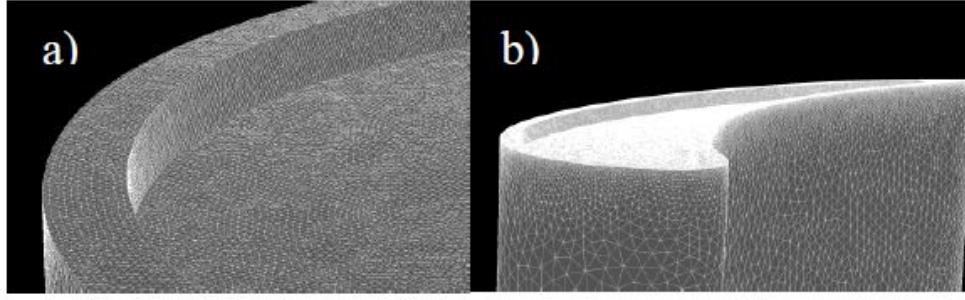
Figure 5.2: Surface mesh a) blade tip b) blade

The Richardson extrapolation [56] is used to calculate the discretization error in the computations performed. The Grid Convergence Index (GCI) is defined as follows:

$$GCI_{21} = \frac{1.25 e_{a_{21}}}{r_{21}^p - 1} \tag{5.1}$$

According to this definition, e_a is the approximate relative error between the predictions from two different size of meshes, and r is the refinement factor, which are defined by the following equations:

$$e_{a_{21}} = \left| \frac{\oslash_1 - \oslash_2}{\oslash_1} \right| \tag{5.2}$$

and

$$r_{21} = \left(\frac{N_1}{N_2} \right)^{1/D} \tag{5.3}$$

Here, subscript 1 denotes the fine mesh, and subscript 2 the medium mesh. $\oslash$ is the predicted value by each mesh, D is the dimensionality of the study and is taken as 3, and N is the corresponding number of nodes. The order of accuracy, p, that appears in Eq. (5.1) can be calculated iteratively through the following equations:

$$p = \frac{1}{ln(r_{21})} \left| ln \left| \varepsilon_{32}/\varepsilon_{31} \right| + q(p) \right| \tag{5.4}$$

$$q(p) = ln\left(\frac{r_{21}^p - s}{r_{32}^p - s}\right) \qquad (5.5)$$

$$s = sgn(\varepsilon_{32}/\varepsilon_{31}) \qquad (5.6)$$

where $\varepsilon_{32} = \oslash_3 - \oslash_2$ and $\varepsilon_{21} = \oslash_2 - \oslash_1$. The meshes mentioned above have 0.85 M, 2 M, and 4.7 M nodes. The GCI was evaluated for the area-averaged wall heat transfer coefficient at the blade tip. Calculations lead to a value of 3.5%, suggesting that the discretization error is small.

5.4   Results

In this section, the results obtained by the computations performed for six cases are presented. The effects of tip cooling on a rotating blade tip are examined for the squealer tip geometry while the rim height was varied, giving different depth-to-width ratios. The flow structure and Mach number distributions inside of the tip cavities are studied first. For this, axial planes are used to span the flow field along the chord with streamlines displayed on each plane. The uncooled cases are depicted in Figure 5.3 and the cooled ones are depicted in Figure 5.4.

In the tip cavity, a single cavity vortex is observable from Figure 5.3 in the stationary domain. However, when the domain is rotated, two different types of vortices are formed here. The similar vortical structures were observed in the study by Zhou [42] in the comparisons of stationary and moving endwall in a transonic turbine cascade. The second vortex formed inside the cavity near the suction side has apparently been caused by the rotation, which is defined as the cavity scraping vortex in [42]. More-over, the cavity vortex seems to be restrained in a small zone near the pressure side of the blade, where it flows into the squealer cavity. These flow features are more dominant towards the blade leading edge for both cases, and the vortex strength di-minishes towards the blade trailing edge along the chord of the blade. The resulting local Mach numbers in the flow passage by the blade suction side are lower com-pared to the rotational case due to the differences in the flow conditions between the
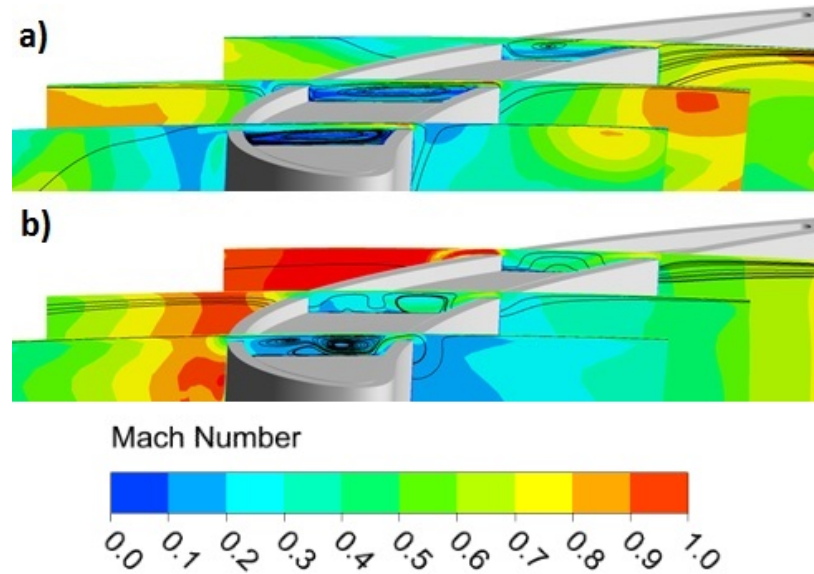
Figure 5.3: Mach number distributions without cooling, $d/w = 1$, a) stationary, b) rotating

two cases. However, regardless of rotation, once the leakage flow enters the cavity from the blade pressure side, its motion is restrained inside the cavity, resulting in a low-momentum flow field, due to the increase in the volume over the blade tip.

When the uncooled stationary case in Figure 5.3 is compared with its cooled counterpart in Figure 5.4, it s observed that the tip leakage flow cannot cross the tip gap as smoothly anymore and the shape of the cavity vortex is disturbed due to the ejection of cooling air from the tip holes. The vortex structure over the tip also changes for the rotational cases with the addition of cooling. As the rim height is increased, the strength and location of vortices change inside the cavity. Consequently, the location of the flow impingement on the surface will change, which will in return affect the thermal performance of the tip cavity.

More information on the interaction of the tip leakage flow and the coolant flow can be obtained by observing the flow path by streamlines. Figure 5.5 shows the main flow streamlines in blue and the streamlines for cooling flow in red. The number of streamlines used in each configuration is kept the same. With the addition of cooling, the flow circulation due to the cavity vortex helps to distribute the cooling air more effectively across the cavity. In addition, when the rotational effects are introduced,
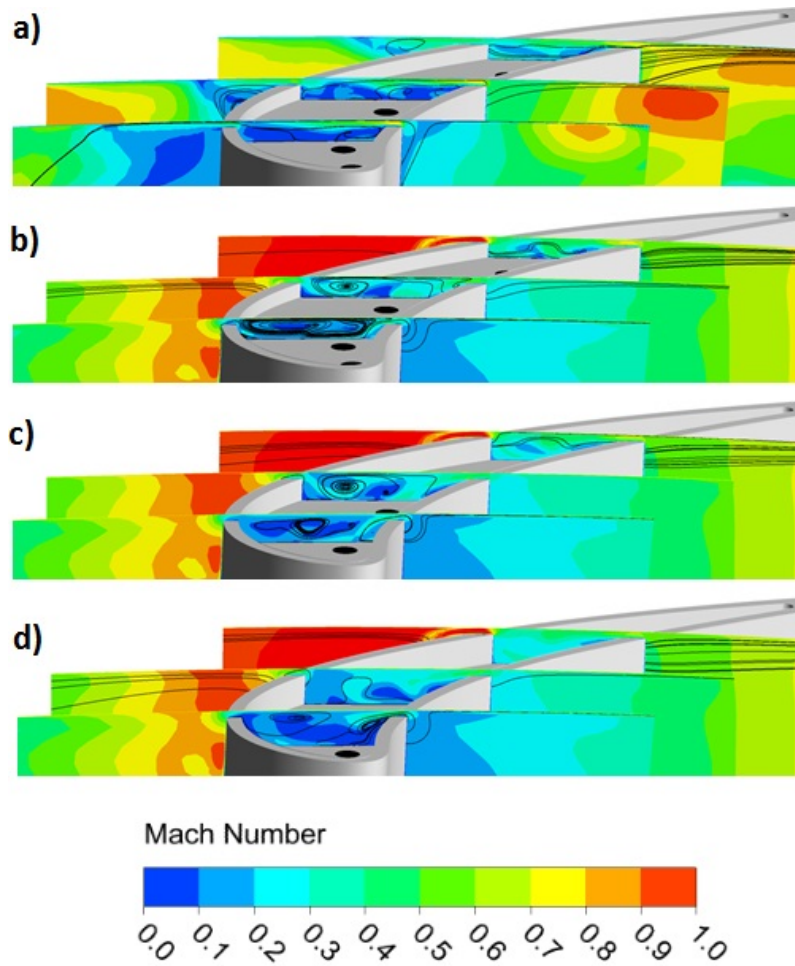
Figure 5.4: Mach number distributions with cooling, a) stationary, $d/w = 1$, b) rotating, $d/w = 1$, c) rotating, $d/w = 1.5$, d) rotating, $d/w = 2$
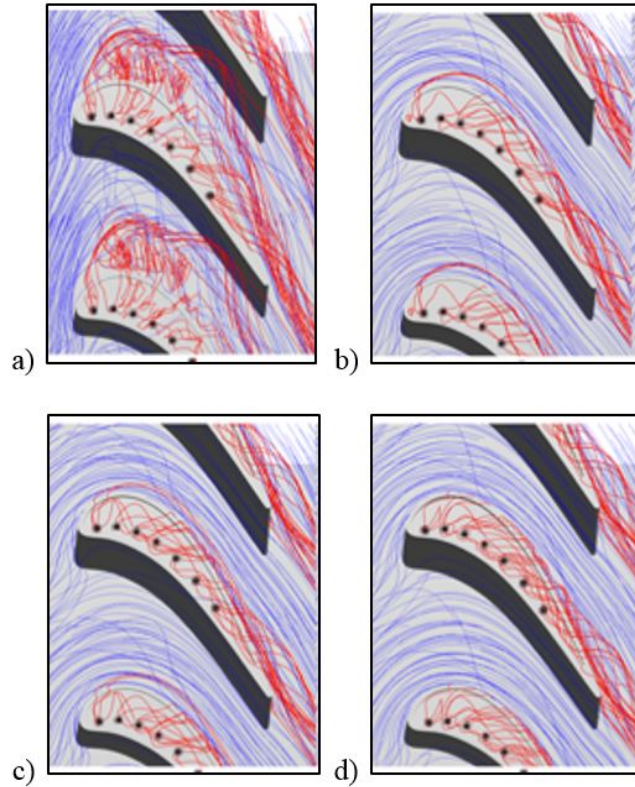
Figure 5.5: Cooled tip streamline patterns, a) stationary, $d/w = 1$, b) rotating, $d/w = 1$, c) rotating, $d/w = 1.5$, d) rotating, $d/w = 2$

it is observed that the flow over the tip change its direction: it passes over the blade tip at a lower incidence angle. This results in a reduction in the cooling coverage of the floor in the vicinity of the cooling holes by the pressure side. The change in the incidence angle observed here was also observed by Rezasoltani et al. in [35]. In their study, they varied the rotational speed. Although the cooling configuration they investigated was different and the speeds were not as high as in the current study, the decrease in the incidence angle caused by the increase in the rotational speed was obvious. Another observation from Figure 5.5 is that as the height of the rim is increased, the coolant flow circulation inside the cavity is intensified. From Figure 5.5 it is evident that there is a difference in the tip aerodynamics with the addition of rotation and further with the change in the depth-to-width ratio of the cavity. These differences cause significant outcomes in the blade tip thermal performance that will be demonstrated next.

5.4.1   Heat Transfer Coefficient Calculations

Typically, as performed by Eq. (1.7), the heat transfer coefficient can be calculated in film cooling applications. However, when the wall temperature is kept constant and is very close to the adiabatic wall temperature, the heat transfer coefficient results in negative values. This is what was mainly observed in the post processing performed in this section upon the use of Eq. (1.7). Li et al. [57] proposed a general formula for the calculation of the heat transfer coefficient as given by the following equation:

$$h_c = \frac{q_{ref} - q}{T_{ref} - T_w} \tag{5.7}$$

Equation (5.7) was used in the heat transfer calculations since the calculated adiabatic wall temperatures for the cases involving cooling were in the vicinity of the wall temperature of 470 K. T_{ref} was taken as the inlet static temperature of 560 K for the cases involving rotation, whereas it was taken as 628 K for the stationary cases. The calculation of h_c is performed by separate simulations: one for the calculation of q and the other for the calculation of q_{ref} for each case in the study.
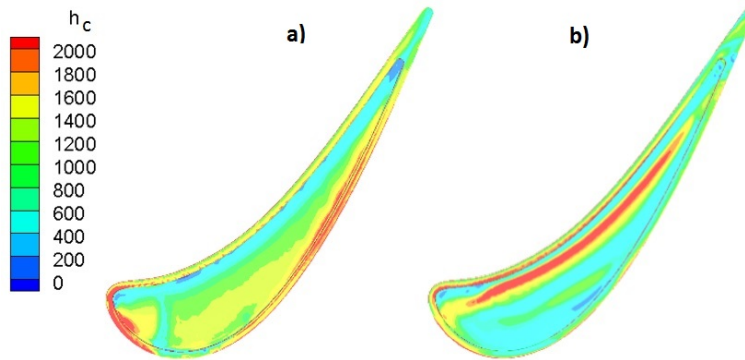
Figure 5.6: Heat transfer coefficient distributions without cooling and with $d/w = 1$ a) stationary b) rotating

Figure 5.6 shows the contours of heat transfer coefficient at the blade tip surface for the cases with d/w = 1 without cooling. Part (a) and part (b) demonstrate results from the stationary and rotating cases, respectively. High heat transfer coefficients observed by the leading edge and along the suction-side rim in the stationary case

correspond to those locations where the tip flow impinges on the tip surface. In fact, a hot spot by the leading edge is known to be a characteristic of the squealer tip flow [38] since the flow separates over the rim at the leading edge causing the flow reattachment at this spot. The region of high heat transfer observed along the suction side in the stationary case and the lower heat transfer region observed along the pressure side are the resulting effects of the cavity vortex dominating the cavity. On the other hand, it is clear that there are local alterations in the trends at the blade tip due to the blade rotation. A red streak is now distinguishable along the blade chord near the pressure side of the blade in the rotational case. This line coincides with the locations where the cavity vortex pushes the tip flow towards the floor and causes it to impinge on the surface, which augments heat transfer levels from the mainstream to the blade. These findings are in agreement with those in literature [38], [42].

With the ejection of cooling air, the gradients in heat transfer coefficient are intensified. Examining the stationary case in Figure 5.7, in the vicinity of the cooling holes by the blade pressure side, the heat transfer coefficient is still found to be at its lowest levels. The higher heat transfer coefficient region observed by the suction side is also still at the background, but the uniformity in the distribution is now disturbed due to cooling air ejection that locally decreases the heat transfer coefficient along the cooling traces that are formed downstream of the holes. This results in pockets of highest levels of heat transfer coefficient both across the cavity floor and on the suction-side rim. These trends were also reported by Ma et al. [28] and Saul et al. [38], in the stationary configurations they studied. This shows that large thermal gradients exist over the tip surface, especially in the vicinity of the cooling holes, which leads to high thermal stresses. When the blade is exposed to rotation in the presence of cooling, the gradients in the distribution seen in its uncooled counterpart are weakened due to the mixing effect of the cooling air; hence the effect of the scraping cavity vortex is still dominating the floor at the background. Downstream of the cooling holes, the cooling air is pushed towards the suction side at the new incidence angle as was discussed with Figure 5.5, leaving lower heat transfer coefficient traces in the cooling air trajectory. The effect of rim height on the heat transfer coefficient distribution can also be seen in Figure 5.7. As the height of the cavity rim is increased, the distribution reflects the changes observed in the cavity flow field shown in Figure 5.4.

81

The main observable trend is that as the volume over the tip increases from a ratio of $d/w = 1$ to $d/w = 2$, a larger area is exposed to the lowest levels of heat transfer coefficient. However, for the intermediate case of $d/w = 1.5$, a line of high heat-transfer-coefficient pockets along the camber can be observed in a region around the cooling holes. This line corresponds to the location of the vortex observed in the mid cavity of this case in Figure 5.4. For the highest-rim case considered in this study, the strength of this vortex has lessened to a great extent.

Limited findings in literature referring to the tip flow for a rotating squealer-tip blade show that flow here is indeed complex and there are different driving mechanisms behind. Yang and Feng [40] performed simulations on the same E3 blade and with similar boundary conditions used in the current study. The blade was rotating, but the configurations had no cooling. They varied the rim height at two different tip gap values. What they observed was that for 1% clearance gap, heat transfer decreased as the rim height was increased. However, this trend was reversed when the tip gap was increased to 2% - heat transfer increased as the rim height increased. Computations of Acharya and Moreaux [34], involved cooling and the effect of rotation. The blade had only two holes at the tip that were located at the leading edge and the other holes were on the blade pressure side, while the rotational speed was considerably lower than the one used in the current study. For their higher-rim case, they observed a general reduction in heat transfer coefficient on the rims, but in the immediate neighborhood of the cooling holes on the cavity floor the gradients of the heat transfer coefficient were intensified. This behavior is similar to what is observed for the intermediate rim height of $d/w = 1.5$ in Figure 5.7. Introduction of cooling into the complex flow field at the squealer blade tip under the effect of rotation apparently causes significant alterations in the thermal performance of the tip. These findings show that more investigation is needed to understand the tip leakage flow behavior so that the tip design can be optimized to achieve the desired thermal performance.
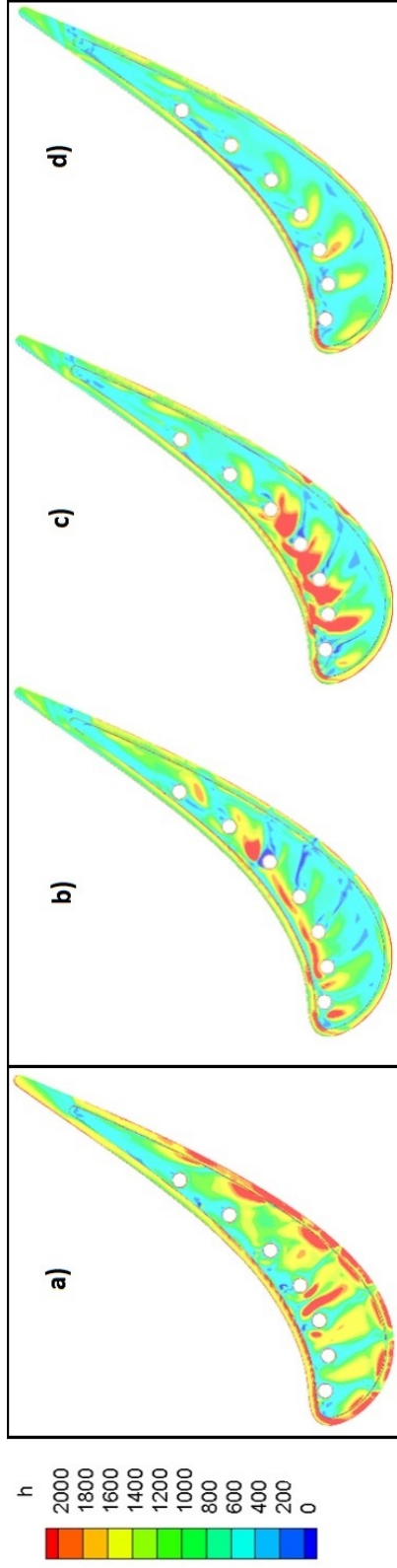
Figure 5.7: Heat transfer coefficient distributions with cooling a) stationary, $d/w = 1$, b) rotating, $d/w = 1$, c) rotating, $d/w = 1.5$, d) rotating, $d/w = 2$
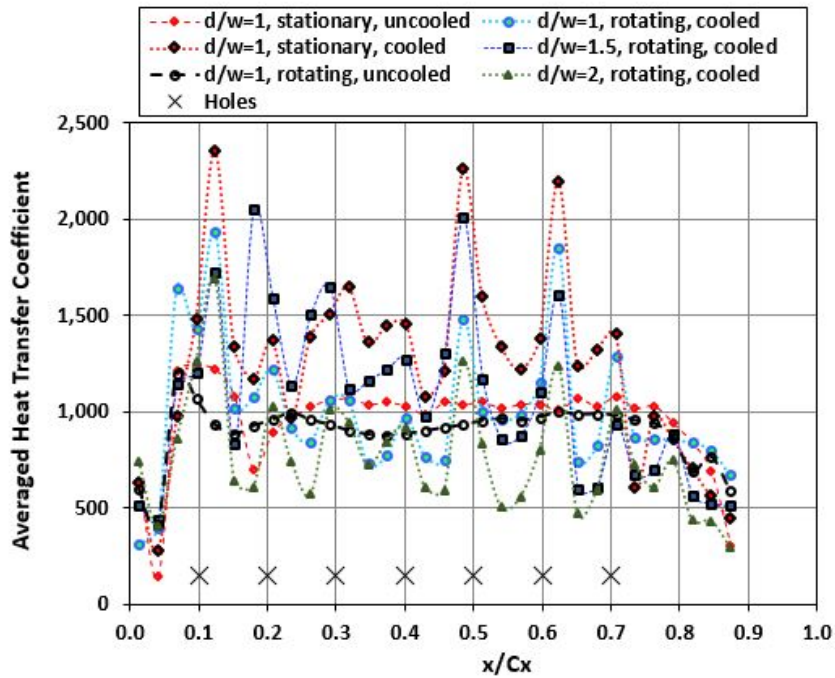
Figure 5.8: Averaged heat transfer coefficient, along axial chord

The heat transfer coefficient distributions depicted in Figure 5.6 and 5.7 are laterally averaged on the blade tip and the calculations are presented along the axial chord in Figure 5.8. The rim surfaces were not included in the averaging. The empty symbols represent the uncooled cases and the solid symbols represent the cooled ones. The locations of the cooling holes are shown by the cross signs. Despite their differences, the two uncooled cases show fairly uniform trends from the leading edge towards the trailing edge of the blade; i.e upon averaging, the effect of distinctive local features observed in Figure 5.6 for the stationary and rotating blades from pressure side to suction side have disappeared. The rise in the first 10% of the chord due to the flow reattachment at the leading edge is still observable. For the cooled cases, the peak heat transfer levels occur in the vicinity of the cooling holes. The abrupt changes across the pockets of heat transfer on the tip surface due to cooling addition shown in Figure 5.7, are reflected as altering peaks and drops along the axial chord in Figure 5.8.

5.4.2 Film-Cooling Effectiveness Results

To examine the film-cooling performance of the studied tip configurations, the film-cooling effectiveness parameter is calculated by the following equation:

$$\eta = \frac{T_{inlet} - T_{aw}}{T_{inlet} - T_c} \tag{1.8}$$

where T_{inlet} is the inlet static temperature and T_c is the coolant temperature. Film-cooling effectiveness of the stationary and rotational squealer tips are demonstrated in Figure 5.9. In all cases, the pressure- side rim has the lowest amount of effectiveness, since, as soon as the cooling air is injected into the tip gap, it is pushed away from the pressure side in the flow direction according to Figure 5.5. Due to the high incidence angle that was observed in the stationary case, the leading edge of the blade receives good film-cooling coverage. High effectiveness values in the vicinity of the cooling holes indicate that the cooling film layer is attached to the surface here protecting it from the hot mainstream flow. Keeping in mind the differences in flow conditions between the stationary and rotating cases, with the introduction of rotation, the film coverage has considerably lessened in the cavity floor for the rim height of $d/w = 1$. Comparing the distributions of heat transfer coefficient given in Figure 5.7, the distributions of high film-cooling effectiveness generally correspond to the regions of high heat transfer coefficient, but the opposite is also observed locally across all tips. As the height of the rim increases, the film-cooling effectiveness significantly increases across the cavity since taller rims do not allow as much tip leakage flow to enter the cavity floor. Further increase in the rim height drives the film effectiveness to a more uniform distribution over the tip surface.

In a similar fashion to Figure 5.8 the distributions of film-cooling effectiveness are laterally averaged and presented along the axial chord in Figure 5.10. The rim surfaces were again excluded from the averages. The reduction in film-cooling effectiveness upon the introduction of blade rotation is obvious under the examined conditions in this study. Other than the leading edge region up to 20% axial chord, there is generally an increase in the cooling coverage as the rim height is increased. Figures 5.10 and 5.11 give the area-averaged heat transfer coefficient and film-cooling effectiveness, respectively. Here, the averages on the rim surfaces and the cavity floor are

Figure 5.9: Film-cooling effectiveness, a) stationary, $d/w = 1$, b) rotating, $d/w = 1$, c) rotating, $d/w = 1.5$, d) rotating, $d/w = 2$

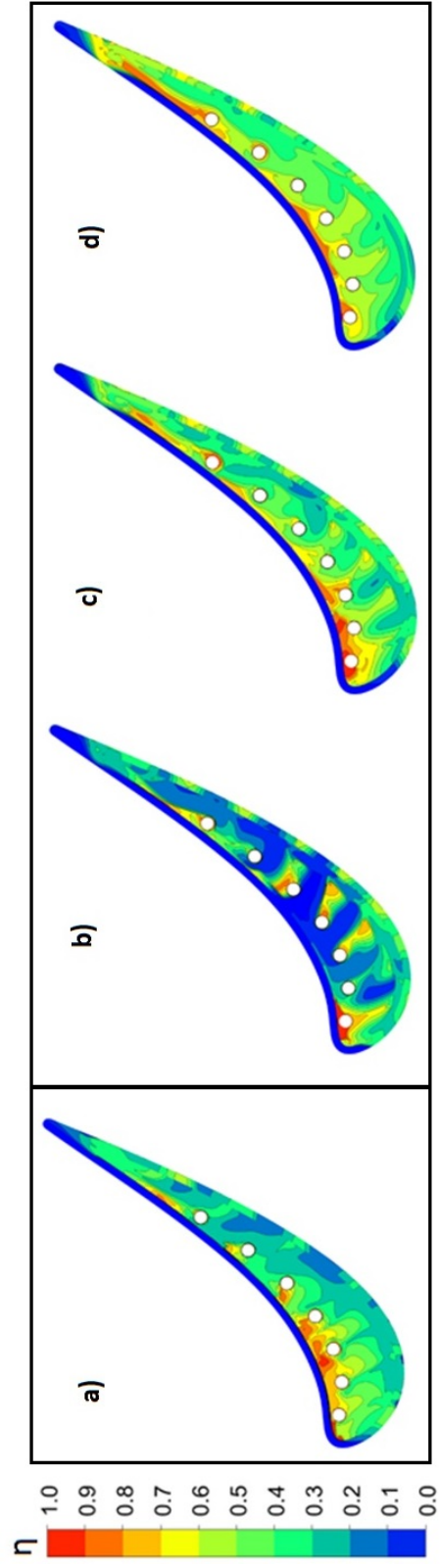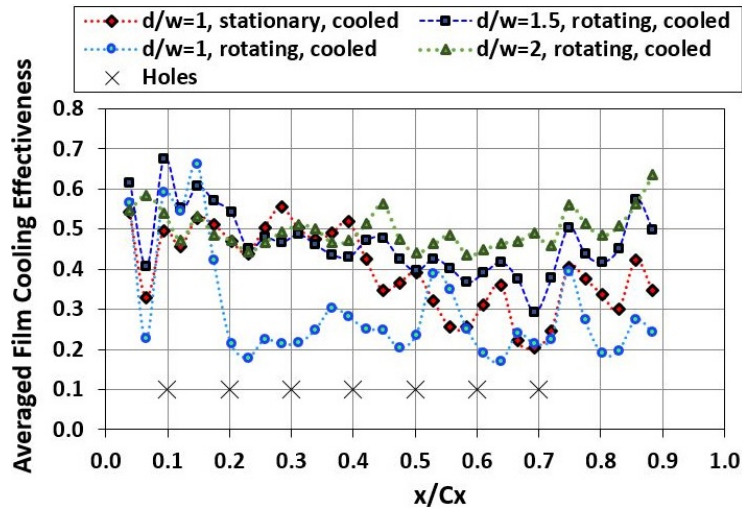Figure 5.10: Averaged film-cooling effectiveness, along axial chord

shown separately. It is evident that the heat transfer coefficient is consistently higher on the squealer rims compared to the cavity floor for all cases. This difference is the highest when the blade is stationary. Alteration in the tip flow structure due to blade rotation that was observed in Figure 5.4 causes reduction in this difference in heat transfer between the cavity floor and the rims, while it reduces heat transfer generally over the whole tip.

Another observation is that the addition of cooling increases heat transfer on the blade tip, and this increase is more significant when the blade is stationary compared to the rotating blade. The local differences in the tip flow observed between the two tips with $d/w = 1$ and $d/w = 1.5$ result in an increase in the heat transfer on the cavity floor of the latter case due to the vortex located close to the cooling holes, but the rim does not reflect any differences. With further increasing the rim height to a ratio of $d/w = 2$, both floor and the rims clearly show lessened levels of heat transfer.

On the other hand, Figure 5.12, shows that the film-cooling effectiveness is consistently higher on the cavity floor than on the rim for all four cases. The difference in the effectiveness between the floor and the rim is the highest for the stationary case. This is similar to the trends of heat transfer coefficient. When the rotational effects are present in the flow field, a reduction in cooling coverage over the blade tip is observed. With an increase in the rim height, the cooling coverage clearly improves over all tip surfaces.

87
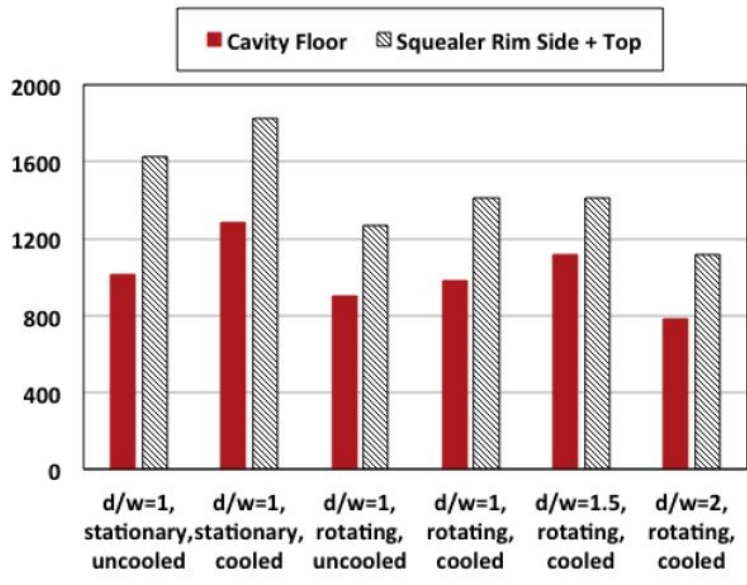
Figure 5.11: Averaged heat transfer coefficient on cavity floor and rim surfaces
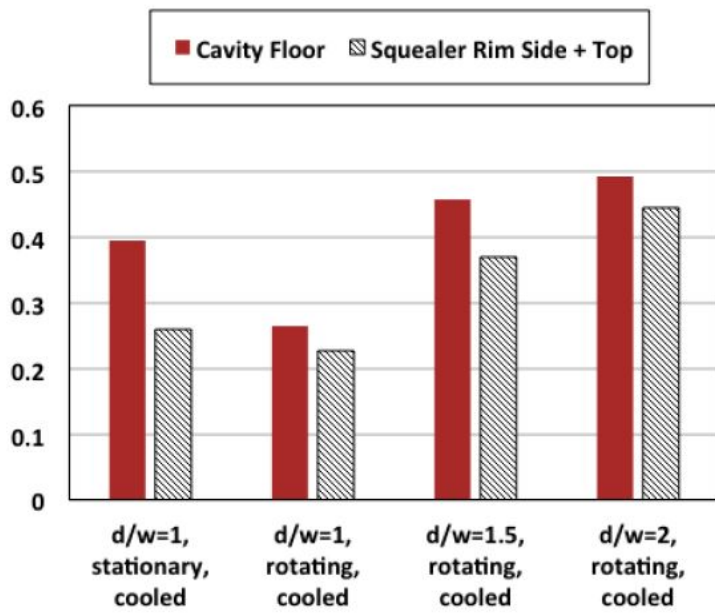
Figure 5.12: Averaged film-cooling effectiveness on cavity floor and rim surfaces

5.4.3 Summary of Findings

A different vortex structure is observed when the blade is rotating. The effect of rotation is seen as a reduction in heat transfer for both cooled and uncooled cases. Due to rotation, the heat transfer values on the cavity floor are increased; a red streak become apparent on the cavity floor near the pressure side of the blade. Blade tip heat transfer also increases with the addition of cooling. When the rim height is increased from $d/w = 1$ to $d/w = 2$, a more evenly-distributed lower heat transfer coefficient region is observed where the red pockets on the cavity floor disappear. Besides, the results show a clear improvement in blade tip film-cooling effectiveness as the depth of the rim increases.

CHAPTER 6

CONCLUSIONS

The research in the literature investigating the tip flow has focused mainly on the cooling performance of the tip. In those studies, the parameters such as the blade tip geometry, clearance gap, and flow conditions have been of primary interest. In contrast, the studies focusing on the details of the cooled blade tip and investigating this environment from an aerothermal aspect are scarce in literature. The main reason to why this study was performed is that the effects of the details such as:

1. the cooling hole configuration implemented on a blade tip, and

2. the blade tip geometry

on blade tip leakage flow and heat transfer need to be clearly understood for a successful blade design with improved aerodynamic and thermal performance.

The injection of coolant changes the flow structure in the gap from an aerodynamic point of view. These changes in blade tip aerodynamics would further lead to alteration in the heat transfer performance of the blade tips. Blade tips that are exposed to high temperatures inevitably experience tip erosion, causing performance degradation. Therefore, it is essential to understand the aerodynamic driving mechanisms affecting the heat transfer performance and the aerodynamic performance losses due to the implementation of cooling holes and the blade tip geometry.

In the current study, the configurations of a high-pressure turbine (HPT) blade with different tip cooling arrangements and geometrical variations are investigated using computational fluid dynamics (CFD). The confidence in the predictions was established by performing several CFD validations. The results for both stationary and

91

rotating analyses are presented. The findings of this research are intended to guide the designers and to contribute to the literature.

In the stationary part of this research, the main focus was on the blade tip cooling configuration and its geometry. Two different blade tip geometries, namely the flat and squealer tips, combined with a tip cooling configuration consisting of varying number, location, and size of cooling holes were examined in a stationary domain, to understand the effects of tip leakage flow on the total pressure loss and the effects of cooling injection on the aerodynamic and thermal performance of the blade.

In the rotating part of this research, the focus was on the geometry variation of the bade tip, particularly of squealer type, that had a fixed cooling hole arrangement. In this section, the effects of rotation were also examined by introducing the results from the stationary cases involving the same blade tip with the goal of providing qualitative comparisons between the two domains.

The findings regarding the details of the blade tip cooling configuration and the tip geometry, as was discussed in Chapter 4, can be summarized as follows :

- The aerodynamic study revealed that the use of a squealer tip instead of a flat tip leads to a significant reduction in the loss amounts, due to the additional volume existing inside the cavity that slows down the flow here by providing extra space for flow expansion.

- The examination of the aerodynamic losses across the clearance gap showed that the lowest levels of aerodynamic loss are encountered at 75% of the clearance gap for all configurations. This might be the particular location where the coolant flow most effectively counteracts the leakage flow. effectively counteracts the leakage flow.

- The heat transfer study showed that the squealer tips also exhibit lower heat transfer levels on the blade tip cavity floor compared to the flat tips, both with or without cooling.

- Placing the holes close to the pressure side on a flat tip increases the tip losses.

- The change in heat transfer with the location of holes is observed to be negligi-

ble for the four-hole configuration.

- When the holes are moved toward the pressure side in squealer tips, it clearly improves the thermal efficiency, with the seven-hole configuration.

The findings regarding the effect of the depth-to-width ratio of a squealer tip was investigated investigated in Chapter 5. What is also investigated is the heat transfer of a cooled blade tip under the effect of rotation. The blade tip was examined in the stationary and rotating domains, for which the boundary conditions were matched except the pressure ratio, revealing additional information on the rotation effects on general trends of tip flow and heat transfer. These findings are summarized below:

- The vortex structure inside the gap is altered when the domain rotation is introduced. It leads to a reduction in tip heat transfer, regardless of tip cooling.

- When the blade tip is cooled, heat transfer increases both on the cavity floor and on the rim, for both the stationary and the rotational cases.

- Changing the depth-to-width ratio from 1 to 2 results in an obvious reduction in the averaged heat transfer coefficient.

- The improvement due to the increase in the rim height is more noticeable in terms of film-cooling effectiveness.

REFERENCES

[1] J. Moore and J. S. Tilton, "Tip leakage flow in a linear turbine cascade," *Journal of Turbomachinery*, vol. 110(1), pp. 18–26, 1988.

[2] A. Huang, "Loss mechanisms in turbine tip clearance flows," *M.Sc Thesis, MIT*, 2011.

[3] J. D. Denton, "The 1993 IGTI scholar lecture: Loss mechanisms in turbomachines," *Journal of Turbomachinery*, vol. 115(4), p. 621, 1993.

[4] L. P. Timko, "Energy efficient engine high pressure turbine component test performance report," *NASA-CR-168289*, 1984.

[5] A. B. Vetta, P. W. Giel, and G. E. Welch, "Aerodynamic investigation of incidence angle effects in a large scale transonic turbine cascade," *NASA/TM-2013-218070*, 2013.

[6] J. D. Mattingly and foreword by H. von Ohain, *Elements of propulsion: gas turbines and rockets*. AIAA Education Series, 2006.

[7] F. J. G. Heyes and H. P. Hodson, "The measurement and prediction of the tip clearance flow in linear turbine cascades," *Journal of Turbomachinery*, vol. 115(3), p. 376, 1993.

[8] C. Zhou and H. Hodson, "The tip leakage flow of an unshrouded high-pressure turbine blade with tip cooling," *Journal of Turbomachinery*, vol. 133(4), p. 041028, 2011.

[9] P. J. Newton, G. D. Lock, S. K. Krishnababu, H. P. Hodson, W. N.Dawes, J. Hannis, and C. Whitney, "Aero-thermal investigation of tip leakage flow in axial flow turbines - part 3, tip cooling," *Journal of Turbomachinery*, vol. 131(1), p. 011008, 2009.

[10] J. Tallman and B. Lakshminarayana, "Numerical simulation of tip leakage flows in axial flow turbines, with emphasis on flow physics: Part 1—effect of tip clearance height," *Journal of Turbomachinery*, vol. 123(2), p. 314, 2001.

[11] Y. C. Nho, J. S. Park, Y. Lee, and J. S. Kwak, "Effects of turbine blade tip shape on total pressure loss and secondary flow of a linear turbine cascade," *International Journal of Heat and Fluid Flow*, vol. 33(1), pp. 92–100, 2012.

[12] Y. C. Nho, Y. J. Lee, and J. Kwak, "Effects of tip shape on the gas turbine blade tip heat transfer," *Journal of Thermophysics and Heat Transfer*, vol. 26(2), pp. 305–312, 2012.

[13] J. S. Kwak and J. C. Han, "Heat transfer coefficients on the squealer tip and near squealer tip regions of a gas turbine blade," *Journal of Heat Transfer*, vol. 125(4), p. 669, 2003.

[14] N. L. Key and T. Arts, "Comparison of turbine tip leakage flow for flat tip and squealer tip geometries at high-speed conditions," *Journal of Turbomachinery*, vol. 128(2), pp. 213–220, 2006.

[15] S. Naik, C. Georgakis, T. Hofer, and D. Lengani, "Heat transfer and film cooling of blade tips and endwalls," *Journal of Turbomachinery*, vol. 134(4), p. 041004, 2011.

[16] P. J. Newton, G. D. Lock, S. K. Krishnababu, H. P. Hodson, W. N.Dawes, J. Hannis, and C. Whitney, "Heat transfer and aerodynamics of turbine blade tips in a linear cascade," *Journal of Turbomachinery*, vol. 128(2), pp. 300–309, 2006.

[17] J. R. Christophel, K. A. Thole, and F. J. Cunha, "Cooling the tip of a turbine blade using pressure side holes- part 2: Heat transfer measurements," *Journal of Turbomachinery*, vol. 127(2), p. 278, 2005.

[18] G. S. Azad, J. Han, and R. Boyle, "Heat transfer and pressure distribution on a gas turbine blade tip," *Journal of Turbomachinery*, vol. 122(4), p. 717, 2000.

[19] G. S. Azad, J. C. Han, and R. J. Boyle, "Heat transfer and flow on the squealer tip of a gas turbine blade," *Journal of Turbomachinery*, vol. 125(4), p. 669, 2000.

[20] S. K. Krishnababu, P. J. Newton, W. N.Dawes, G. D. Lock, H. P. Hodson, J. Hannis, and C. Whitney, "Aero-thermal investigations of tip leakage flow in axial flow turbines - part 1, effect of tip geometry and tip clearance gap," *Journal of Turbomachinery*, vol. 131(1), p. 011006, 2009.

[21] H. Nasir, S. V. Ekkad, D. M. Kontrovitz, R. Bunker, and C. Prakash, "Effect of tip gap and squealer geometry on detailed heat transfer measurements over a high pressure turbine rotor blade tip," *Journal of Turbomachinery*, vol. 126(2), p. 221, 2004.

[22] J. S. Kwak and J. C. Han, "Heat transfer coefficient on a gas turbine blade tip and near tip regions," *8th AIAA/ASME Joint Thermophysics and Heat Transfer Conference, AIAA 2002-3012*, 2002.

[23] R. Bunker, "A review of turbine blade tip heat transfer," *Annals of the New York Academy of Sciences*, vol. 934(1), pp. 64–79, 2006.

[24] M. Niu and S. Zang, "Numerical investigation of active tip-clearance control through tip cooling injection in an axial turbine cascade," *Journal of Thermal Sciences*, vol. 18(4), pp. 306–312, 2009.

[25] B. Mercan, Y. Ostovan, E. Dogan, and O. Uzol, "Experimental investigation of the effects of waveform tip injection in a low pressure turbine cascade," *ASME Turbo Expo: Power for Land, Sea, and Air*, vol. 8, Parts A, B, and C, GT2012-69316, pp. 1473–1485, 2012.

[26] J. R. Volino, "Control of tip leakage in a high-pressure turbine cascade using tip blowing," *Journal of Turbomachinery*, vol. 139(6), p. 061008, 2017.

[27] S. Mhetras, D. Narzary, Z. Gao, and J. C. Han, "Effect of a cutback squealer and cavity depth on film-cooling effectiveness on a gas turbine blade tip," *Journal of Turbomachinery*, vol. 130(2), p. 021002, 2008.

[28] H. Ma, Q. Zhang, L. He, Z. Wang, and L. Wang, "Cooling injection effect on a transonic squealer tip – part i: experimental heat transfer results and cfd validation," *Journal of Engineering for Gas Turbines and Power*, vol. 139(5), p. 052506, 2017.

[29] F. Cheng, J. Zhang, H. Chang, and J. Y. Zhang, "Investigations of film-cooling effectiveness on the squealer tip with various film-hole configurations in a linear cascade," *International Journal of Heat and Mass Transfer*, vol. 117, pp. 344–357, 2018.

[30] O. Tamunobere and S. Acharya, "Turbine blade tip cooling with blade rotation - part 1: tip and pressure side coolant injection," *Journal of Turbomachinery*, vol. 138(9), p. 091002, 2016.

[31] P. Palafox, M. Oldfield, P. Ireland, T. Jones, and J. LaGraff, "Blade tip heat transfer and aerodynamics in a large scale turbine cascade with moving endwall," *Journal of Turbomachinery*, vol. 134(2), p. 021020, 2012.

[32] J. Tallman and B.Lakshminarayana, "Numerical simulation of tip leakage flows in axial flow turbines, with emphasis on flow physics: Part 2- effect of outer casing relative motion," *Journal of Turbomachinery*, vol. 134(2), p. 324, 2001.

[33] D. Yang, X. Yu, and Z. Feng, "Investigation of leakage flow and heat transfer in a gas turbine blade tip with emphasis on the effect of rotation," *Journal of Turbomachinery*, vol. 132(4), p. 041010, 2010.

[34] S. Acharya and L. Moreaux, "Numerical study of the flow past a turbine blade tip: effect of relative motion between blade and shroud," *Journal of Turbomachinery*, vol. 136(3), p. 031015, 2013.

[35] M. Rezasoltani, K. Lu, M. Schobeiri, and J. C. Han, "A combined experimental and numerical study of the turbine blade tip film cooling effectiveness under rotation condition," *Journal of Turbomachinery*, vol. 137(5), p. 051009, 2014.

[36] R. Mayle and D. Metzger, "Heat transfer at the tip of an unshrouded turbine blade," *Proceedings 7th International Heat Transfer Conference*, vol. 3, pp. 87–92, 1982.

[37] J. D. Coull and N. R. Atkins, "The influence of boundary conditions on tip leakage flow," *Journal of Turbomachinery*, vol. 137(6), p. 061005, 2015.

[38] A. J. Saul, P. T. Ireland, J. D. Coull, T. H. Wong, H. Li, and E. Romero, "An experimental investigation of adiabatic film cooling effectiveness and heat transfer

coefficient on a transonic squealer tip," *Journal of Turbomachinery*, vol. 141(9), p. 091005, 2019.

[39] R. S. Bunker and J. Bailey, "Effect of squealer cavity depth and oxidation on turbine blade tip heat transfer," *ASME Turbo Expo 2001: Power for Land, Sea, and Air, 2001-GT-0155*, p. V003T01A038, 2001.

[40] D. Yang and Z. Feng, "Tip leakage flow and heat transfer predictions for turbine blades," *ASME Turbo Expo: Power for Land, Sea, and Air*, vol. 4, GT2007-27728, pp. 589–596, 2007.

[41] A. Ameri, E. Steinthorsson, and D. Rigby, "Effect of squealer tip on rotor heat transfer and efficiency," *Journal of Turbomachinery*, vol. 120(4), p. 753, 1998.

[42] C. Zhou, "Effects of endwall motion on thermal performance of cavity tips with different squealer width and height," *International Journal of Heat and Mass Transfer*, vol. 91, pp. 1248–1258, 2015.

[43] J. Wang, B. Sunden, M. Zeng, and Q. Wang, "Film cooling effects on the tip flow characteristics of a gas turbine blade," *Propulsion and Power Research*, vol. 4(1), pp. 9–22, 2015.

[44] J. Kwak, J. Ahn, and J. Han, "Effects of rim location, rim height, and tip clearance on the tip and near tip region heat transfer of a gas turbine blade," *Propulsion and Power Research*, vol. 47(26), pp. 5651–5663, 2004.

[45] L. E. Brown, "Axial flow compressor and turbine loss coefficients: A comparison of several parameters," *Journal of Engineering Power*, vol. 94(3), p. 652, 1972.

[46] J. P. Bindon, "The measurement and formation of tip clearance loss," *Journal of Turbomachinery*, vol. 111(3), p. 257, 1989.

[47] S. Pope, *Turbulent Flows*. Cambridge University Press, 2000.

[48] P. Spalart and S. Allmaras, "A one-equation turbulence model for aerodynamic flows," *30th Aerospace Sciences Meeting and Exhibit*, 1992.

[49] B. E. Launder and D. B. Spalding, *Lectures in Mathematical Models of Turbulence*. Academic Press, 1972.

[50] F. Menter, M. Kuntz, and R.Langtry, "Ten years of industrial experience with the sst turbulence model," *Proceedings of the 4th International Symposium on Turbulence, Heat and Mass Transfer*, vol. 32(8), p. 625–632, 2003.

[51] Ansys, "Ansys cfx theory guide, release 18.1, canonsburg, pa," *User Manual*, 2017.

[52] H. Yang, S. Acharya, S. Ekkad, C. Prakash, and R. Bunker, "Flow and heat transfer predictions for a flat-tip turbine blades," *ASME Turbo Expo: Power for Land, Sea, and Air, GT2002-30190*, vol. 3, pp. 271–283, 2002.

[53] R. J. Goldstein, "Film cooling," *Advances in Heat Transfer*, vol. 7, pp. 321–379, 1971.

[54] K. L. Harrison and D. G. Bogard, "Use of the adiabatic wall temperature in film cooling to predict wall heat flux and temperature," *ASME Turbo Expo: Power for Land, Sea, and Air, GT2008-51424*, vol. 4, pp. 1197–1207, 2008.

[55] F. Incropera and D. DeWitt, *Fundamentals of Heat and Mass Transfer*. John Wiley and Sons, 1996.

[56] I. Celik, U. Ghia, P. J. Roache, C. J. Freitas, H. Coleman, and P. E. Raad, "Procedure for estimation and reporting of uncertainty due to discretization in cfd applications," *J. Fluids Eng.*, vol. 130 (7), p. 078001, 2008.

[57] X. Li, J. Zhou, and K. Aung, "On selection of reference temperature of heat transfer coefficient for complicated flows," *Heat Mass Transfer*, vol. 45(5), pp. 633–643, 2008.